

DISSERTATION

zur

Erlangung der Doktorwürde (Dr. rer. nat.)

der

Naturwissenschaftlich-Mathematischen Gesamtfakultät

der

Ruprecht-Karls-Universität

Heidelberg

vorgelegt von

Felix Julian Berger

geboren in Eberbach

Tag der mündlichen Prüfung

7. Mai 2021

Luminescent Defects in Polymer-Wrapped Carbon Nanotubes

Synthesis, Properties and Applications

Gutachter

Prof. Dr. Jana Zaumseil

Prof. Dr. Sebastian Kruss

Abstract

Narrowband photoluminescence (PL) in the near-infrared and electrical exciton generation make semiconducting single-walled carbon nanotubes (SWNTs) promising materials for optoelectronic devices. The functionalization of SWNTs with luminescent sp^3 defects offers synthetically tunable light emission and enhances their potential for applications such as quantum light sources, bioimaging and sensing. However, the synthetic protocols that are currently used to create these defects are limited to aqueous dispersions of SWNTs, which are compromised by short tube lengths, residual metallic SWNTs and poor solution-processability. Here, the combination of highly selective polymer-sorting and shear force mixing as a mild exfoliation method provides electronically-pure (6,5) SWNTs in toluene with average tube lengths $> 1 \mu\text{m}$ and strategies for their sp^3 functionalization are developed based on simple diazonium chemistry.

The complexation by an ether crown allows for the solubilization of commercially available aryldiazonium salts in organic solvents and thus enables their reaction with polymer-wrapped SWNTs. The resulting defect-tailored (6,5) SWNTs show a relatively high photoluminescence quantum yield (PLQY) of up to 4% with 90% of photons emitted from the sp^3 defect. The dependence of the defect-induced PL brightening on the nanotube length indicates that the PLQY of the pristine SWNT may exceed that of the sp^3 defect for a sufficiently high nanotube quality.

By using custom-synthesized diazonium salts in a modified protocol, stable organic radicals are covalently attached to purified semiconducting SWNTs *via* luminescent aryl defects. The proximity between the defect-localized exciton and the unpaired electron promotes spin exchange and electron transfer processes, which are identified through time-resolved PL measurements. The results point toward an increased yield

of triplet excitons due to radical-enhanced intersystem crossing, which could serve as a general concept to probe triplet states in SWNTs.

The dispersion in organic solvents facilitates the integration of defect-tailored, polymer-wrapped SWNTs into optoelectronic devices. A planar dielectric waveguide structure channels the PL emitted from sp^3 defects over distances > 1 mm and thus represents a first step toward their interfacing with photonic circuits and photovoltaic devices. Moreover, the demonstration of electroluminescence from sp^3 defects in light-emitting field-effect transistors underpins their potential for electrically-driven single-photon sources.

Kurzfassung

Ihre schmalbandige Fluoreszenz im Nahinfrarotbereich und die Fähigkeit zur elektrischen Erzeugung von Exzitonen machen halbleitende, einwandige Kohlenstoffnanoröhren (engl. *single-walled carbon nanotubes*, SWNTs) zu vielversprechenden Materialien für die Anwendung in optoelektronischen Bauelementen. Darüber hinaus können ihre Fluoreszenzeigenschaften durch die Funktionalisierung mit lumineszenten sp^3 -Defekten synthetisch kontrolliert und dadurch für die Anwendung in der Quantenoptik, der biologischen Bildgebung und in Sensoren optimiert werden. Die bisher verfügbaren Protokolle zur Einführung von sp^3 -Defekten haben jedoch den entscheidenden Nachteil, dass sie lediglich auf wässrige Dispersionen von SWNTs anwendbar sind, die typischerweise von kurzen Röhrenlängen, Verunreinigungen durch metallische SWNTs und schlechter Lösungsprozessierbarkeit betroffen sind. In dieser Arbeit werden die hochselektive Methode der Polymersortierung und das Scherkraftmischen als sanfte Exfoliierungsmethode kombiniert, um (6,5) SWNTs mit hoher Reinheit in Toluol zu dispergieren. Diese SWNTs werden anschließend durch neu entwickelte Methoden basierend auf Diazoniumchemie mit sp^3 -Defekten funktionalisiert.

Aryldiazoniumsalze werden durch Kronenether-Komplexierung in organischen Medien löslich gemacht und können auf diese Weise mit SWNTs zur Reaktion gebracht werden. Die dadurch erhaltenen sp^3 -funktionalisierten SWNTs zeigen eine vergleichsweise hohe Fluoreszenzquantenausbeute (engl. *photoluminescence quantum yield*, PLQY) von 4 %, wobei 90 % der emittierten Photonen auf sp^3 -Defekte zurückzuführen sind. Die Abhängigkeit der defektinduzierten PLQY-Steigerung von der Länge der Nanoröhren deutet darauf hin, dass die PLQY der unbehandelten Nanoröhre für hinreichend lange Röhren die PLQY des sp^3 -Defekts übersteigen kann.

Durch die Verwendung maßgeschneiderter Diazoniumsalze und eine entsprechende Anpassung der Reaktionsbedingungen wird die kovalente Funktionalisierung auf-

gereinigter, halbleitender SWNTs mit stabilen, organischen Radikalen über lumineszente sp^3 -Defekte erreicht. Die räumliche Nähe des defektgebundenen Exzitons zum ungepaarten Elektron des Radikals erlaubt deren Wechselwirkung über Spin- und Elektronen-Austauschprozesse, welche durch zeitaufgelöste Fluoreszenzmessungen nachgewiesen werden. Die Daten legen eine erhöhte Population an Triplett-Exzitonen durch radikalbeförderte Interkombinationsübergänge (engl. *radical-enhanced intersystem crossing*) nahe, welche in Zukunft zur gezielten Untersuchung von Triplett-Zuständen in SWNTs ausgenutzt werden könnten.

Das Dispergieren der sp^3 -funktionalisierten, polymerumwickelten SWNTs in organischen Lösungsmitteln vereinfacht ihren Einbau in optoelektronische Bauelemente. Eine planare, dielektrische Wellenleiterstruktur transportiert die Fluoreszenz von sp^3 -Defekten über Strecken > 1 mm und legt damit den Grundstein für die Verknüpfung von sp^3 -Defekten mit photonischen Schaltkreisen und photovoltaischen Bauelementen. Abschließend stellt die Demonstration der Elektrolumineszenz von sp^3 -Defekten in lichtemittierenden Feldeffektransistoren das Potenzial dieses Materialsystems für die Anwendung in elektrisch-gepumpten Einzelphotonenquellen unter Beweis.

Acknowledgements

First of all, I am grateful to **Prof. Jana Zaumseil** for giving me the opportunity to work in her group, for her continuous support and everything she has taught me over the past few years. Thank you for trusting in my abilities, for involving me in collaborations and giving me the chance to present at so many conferences. I enjoyed my time in your group very much.

I would also like to thank **Prof. Sebastian Kruss** for kindly agreeing to review this thesis.

In addition, I am thankful to all members of the **NMOE** and **PC2D** groups for creating such a nice atmosphere in the labs and offices, which made me look forward to coming to the institute in the morning. A special thanks goes to my **office mates** for making every day at work highly enjoyable. I am also grateful to **Max Brohmann** for his advice on finishing this thesis and preparing for the exam.

I would like to thank the students I supervised during their research projects, **Simon Settele, Nicolas Zorn, Sebastian Lindenthal, Lukas Bongartz, Toby Kutsch, Lucas Kistner, Tim Nowack, Christine Müller** and **Marco Fischer**, for doing a great job and making work a lot more entertaining!

I am particularly happy to see such a large overlap between my former students and today's **TRIFECTs team**. Working with you was a real pleasure and showed me once more how important it is to share knowledge and ideas within a group. If we had not worked together so well, even in times of Corona, many of our achievements would not have been possible.

Moreover, I would like to thank all of my external **Collaborators**, especially those who allowed me to visit their labs and learn from them: **Prof. Malte Gather** and **Dr. Andreas Mischok** in St. Andrews/Cologne, **Dr. Núria Crivillers** and **J. Alejandro de**

Sousa in Barcelona as well as **Prof. Alexander Högele** and **Dr. Shen Zhao** in Munich. Thanks for making these trips one of the best parts of my PhD.

Darüber hinaus möchte ich mich bei allen **Mitarbeitern der APC** für den freundlichen Umgang und die Bereitschaft, Probleme kurzfristig zu lösen, herzlich bedanken. Mein besonderer Dank gilt den **Mitarbeitern der Feinmechanischen Werkstatt**, die einen großen Teil unserer experimentellen Arbeit erst ermöglichen.

Wenn man auf seine Studienzeit zurückblickt, waren die größten Herausforderungen meist nicht akademischer Natur. Ebenso werden nicht nur die veröffentlichten Paper in Erinnerung bleiben. Aus diesem Grund danke ich insbesondere **Jan, Steffen, Fabian, Philippe** und **Alex** für den großen Spaß, den wir während des Studiums hatten, und hoffe, dass wir uns auch in Zukunft nicht aus den Augen verlieren werden. Ein großes Dankeschön geht an meine **Eltern**, die immer die Ruhe bewahren und ohne deren Unterstützung vieles nicht möglich gewesen wäre. Schließlich möchte ich mich ganz besonders bei meiner Freundin, **Rebekka**, für unsere gemeinsame Zeit und ihre Unterstützung in der Vergangenheit und in der Zukunft bedanken.

Contents

| | |
|---|-----------|
| Abstract | i |
| Kurzfassung | iii |
| Abbreviations | xi |
| 1 Introduction | 1 |
| 2 Background | 5 |
| 2.1 Single-walled carbon nanotubes | 6 |
| 2.1.1 Structure and synthesis | 6 |
| 2.1.2 Chirality sorting | 8 |
| 2.1.3 Electronic structure | 12 |
| 2.1.4 Excitons | 14 |
| 2.2 Luminescent defects | 19 |
| 2.2.1 Exciton diffusion | 20 |
| 2.2.2 Exciton localization | 21 |
| 2.2.3 Optical properties | 21 |
| 2.2.4 Role of defect structure | 25 |
| 2.2.5 Covalent functionalization of SWNTs | 27 |
| 2.3 Waveguides | 30 |
| 2.4 Light-emitting transistors | 32 |
| 3 Experimental Methods | 35 |
| 3.1 (6,5) SWNT dispersion | 36 |
| 3.2 Aryl-functionalization of polymer-wrapped SWNTs | 37 |
| 3.2.1 Reaction with commercial diazonium salts | 37 |

| | | |
|----------|--|-----------|
| 3.2.2 | Reaction with PTM and PTMH diazonium salts | 38 |
| 3.3 | Film deposition and device fabrication | 40 |
| 3.3.1 | Films for single-tube microscopy | 40 |
| 3.3.2 | Aerosol-jet printing | 40 |
| 3.3.3 | Waveguide fabrication | 40 |
| 3.3.4 | LEFET fabrication | 41 |
| 3.4 | Luminescence spectroscopy | 42 |
| 3.4.1 | Luminescence microscopy setup | 42 |
| 3.4.2 | Time-correlated single-photon counting | 44 |
| 3.4.3 | Cryogenic magneto-optical setup | 44 |
| 3.4.4 | PLQY determination | 45 |
| 3.4.5 | Waveguide characterization | 46 |
| 3.5 | Other characterization techniques | 47 |
| 4 | <i>sp</i>³ Functionalization of Polymer-Wrapped SWNTs | 49 |
| 4.1 | Introduction | 50 |
| 4.2 | Functionalization method | 51 |
| 4.3 | Photoluminescence and absorption of <i>sp</i> ³ defects | 54 |
| 4.4 | Optimization of emission efficiency | 57 |
| 4.5 | Role of initial nanotube quality | 62 |
| 4.6 | Defect density metrics | 65 |
| 4.7 | Summary and conclusion | 70 |
| 5 | Interaction of Defect-Localized Excitons with Stable Organic Radicals | 73 |
| 5.1 | Introduction | 74 |
| 5.2 | Functionalization method | 75 |
| 5.3 | Evidence for covalent radical attachment | 76 |
| 5.4 | Impact of the radical on PL | 79 |
| 5.5 | Mechanisms of interaction | 83 |
| 5.6 | Model of exciton dynamics | 87 |
| 5.7 | PL at low temperature and in high magnetic fields | 91 |
| 5.8 | Probing triplet states by EISC | 94 |
| 5.9 | Summary and conclusion | 96 |

| | | |
|----------|---|------------|
| 6 | Luminescent Defects in SWNT Thin Films | 97 |
| 6.1 | Introduction | 98 |
| 6.2 | Emission efficiency in thin films | 100 |
| 6.3 | Waveguide design and characterization | 105 |
| 6.4 | Emission at high excitation densities | 110 |
| 6.5 | Electroluminescence from sp^3 defects | 115 |
| 6.6 | Summary and conclusion | 118 |
| 7 | Conclusion and Outlook | 121 |
| | Bibliography | 127 |

Abbreviations

| | |
|---------------------|---|
| 0D | zero-dimensional |
| 1D | one-dimensional |
| 2D | two-dimensional |
| ATPE | aqueous two-phase extraction |
| BF | brightfield |
| Br-Dz | 4-bromobenzenediazonium tetrafluoroborate |
| Cl ₂ -Dz | 3,5-dichlorophenyldiazonium tetrafluoroborate |
| CPE | conjugated polyelectrolyte |
| CVD | chemical vapor deposition |
| cw | continuous-wave |
| DLCQ | diffusion-limited contact quenching |
| DOS | density of states |
| EEA | exciton-exciton annihilation |
| EISC | radical-enhanced intersystem crossing |
| EL | electroluminescence |
| EPR | electron paramagnetic resonance |
| EVET | electronic-to-vibrational energy transfer |
| FWHM | full width at half maximum |
| GB | Gomberg-Bachmann |
| IPA | isopropyl alcohol |
| IS | integrating sphere |
| LEFET | light-emitting field-effect transistor |
| LSC | luminescent solar concentrator |
| MPD | multi-phonon decay |
| NIR | near-infrared |

| | |
|---------------------|---|
| NO ₂ -Dz | 4-nitrobenzenediazonium tetrafluoroborate |
| OD | optical density |
| OMe-Dz | 4-methoxybenzenediazonium tetrafluoroborate |
| PET | photoinduced electron transfer |
| PFO-BPy | poly[(9,9-dioctylfluorenyl-2,7-diyl)- <i>alt</i> -(6,6')-(2,2')-bipyridine] |
| PL | photoluminescence |
| PLE | photoluminescence excitation-emission |
| PLQY | photoluminescence quantum yield |
| PSB | phonon sideband |
| PTFE | poly(tetrafluoroethylene) |
| PTM | perchlorotriphenylmethyl |
| RISC | thermally activated reverse intersystem crossing |
| r.t. | room temperature |
| SES | shifting excitation spot |
| SOMO | singly-occupied molecular orbital |
| SWNT | single-walled carbon nanotube |
| TCSPC | time-correlated single-photon counting |
| TD | thermal detrapping |
| TE | transverse electric |
| THF | tetrahydrofuran |
| TIR | total internal reflection |
| TM | transverse magnetic |
| UV | ultraviolet |
| vH | van Hove |
| vis | visible |

Chapter 1

Introduction

As the amounts of data generated by electronic devices all over the world increase from day to day, optical communication is more important than ever. In this technology, digital information is transmitted in the form of modulated light pulses propagating through optical fibers.¹ In order to minimize losses due to signal attenuation and dispersion, the wavelength of light should match one of the transmission windows of the fiber material. For standard silica fibers, these telecommunication bands are located in the near-infrared (NIR) spectral range, with the C band (1530-1565 nm) being the one most commonly used. At present, inorganic semiconductor lasers and light-emitting diodes serve as light sources in communication networks,² but emerging fields such as flexible electronics³ and biophotonics⁴ demand for solution-processable and molecularly tunable NIR emitters.

Semiconducting single-walled carbon nanotubes (SWNTs) are promising candidates for such applications based on their mechanical flexibility, liquid-phase processability and diameter-specific narrowband photoluminescence (PL) in the NIR.^{5,6} By choosing SWNT types, commonly termed chiralities, of suitable tube diameter, the emission wavelength may be tuned to the desired telecommunication band. Moreover, SWNTs are ambipolar semiconductors with high electron and hole mobilities and therefore suitable for electroluminescent devices. On the other hand, SWNTs exhibit low photoluminescence quantum yields (PLQYs) of $\sim 1\%$ and none of the chiralities emitting in the C band is currently accessible in large quantities and high purity.

In recent years, the decoration of SWNTs with luminescent sp^3 defects emerged as a powerful route to alleviate these issues and to enable new functionalities.⁷⁻⁹ sp^3 Defects with specific binding patterns on the nanotube carbon lattice create localized and emissive states below the optical band gap of pristine SWNTs. Thus, sp^3 functionalization provides a way to generate longer-wavelength PL with a given chirality and thereby substantially broadens the range of chiralities capable of emitting at telecommunication wavelengths. In addition, synthetic control over the binding configuration and the molecular structure of the attached group allows for further tuning of the defect's PL wavelength. On top of that, as defect-localized excited states are not subject to diffusive quenching, the PL of sp^3 defects is often brighter than the PL of the pristine SWNT. Furthermore, the option to shift both excitation and emission into the NIR is not only beneficial for optical communication, but also enables nanotube-based *in vivo*

PL imaging in the second biological window (1000-1350 nm) with higher contrast and at lower excitation doses.¹⁰⁻¹²

Moreover, sp^3 defects add new functionalities arising from their zero-dimensional structure. While the one-dimensional SWNT can accommodate multiple excitations and may therefore emit more than one photon at the same time, the molecule-like sp^3 defect represents a two-level system that can only emit photons sequentially. The ensuing NIR single-photon emission is retained at room temperature and makes luminescent nanotube defects an interesting material for fiber-based quantum information technologies.¹³⁻¹⁵ In addition to that, the functionalization with molecular groups featuring characteristic binding motifs may be used to bring biological analytes into close contact with SWNTs and thus provide the basis for efficient optical and electronic sensing.¹⁶⁻¹⁸

However, the synthetic protocols for the creation of luminescent defects are currently limited to aqueous dispersions of SWNTs, which are usually prepared by sonication and sorted for the desired chirality *via* gel permeation chromatography or aqueous two-phase extraction.¹⁹ The resulting dispersions typically suffer from short nanotube lengths, the presence of residual metallic SWNTs and poor film formation properties. Hence, they are not suitable for the fabrication of efficient light-emitting devices and electronic sensors based on sp^3 functionalized SWNTs and therefore, new routes allowing for the functionalization of high-quality SWNTs are required to harness the full potential of nanotube defects.

In this thesis, chirality enrichment is achieved through the highly selective dispersion of nanotubes with conjugated polymers in organic solvents. The combination with shear force mixing²⁰ as a mild and scalable exfoliation method provides access to long, nearly monochiral (6,5) SWNTs in toluene and functionalization protocols are developed to enable their decoration with luminescent sp^3 defects directly in the organic solvent. The study of sp^3 defects in these high-quality nanotubes reveals new aspects of their optical properties, which were previously inaccessible due to the shortcomings of aqueous SWNT dispersions. Subsequently, the excellent solution-processability of polymer-wrapped SWNTs is exploited to integrate defect-tailored SWNTs into photonic structures and light-emitting devices. Moreover, the covalent attachment of stable organic radicals is demonstrated as a way to control the nanotube's

photophysics *via* the efficient interaction between the defect-localized excited state and the nearby unpaired spin.

This thesis is organized as follows. Chapter 2 summarizes the current state of research related to this work. Special attention is paid to the models used to describe the optoelectronic properties of carbon nanotubes and luminescent sp^3 defects. In addition, experimentally relevant topics such as chirality sorting and covalent functionalization of SWNTs as well as the working principles of dielectric waveguides and light-emitting field-effect transistors are covered.

Chapter 3 describes the experimental methods for SWNT dispersion, sp^3 functionalization, device integration and characterization employed in this work. The protocols for sp^3 functionalization, which are developed in this thesis, and the setups used for optical characterization are presented in particular detail.

Chapter 4 introduces a method for the creation of luminescent sp^3 defects in polymer-wrapped SWNTs using commercial aryldiazonium salts. The PLQY of the sp^3 functionalized SWNTs is studied as a function of the defect density, the average nanotube length and the molecular structure of the attached aryl group, thus providing guidelines for its optimization. Furthermore, the weak light absorption arising from sp^3 defects is analyzed to obtain an estimate of the oscillator strength of the defect-associated optical transition.

In Chapter 5, the reaction with custom-synthesized diazonium salts is used to covalently attach stable organic radicals to polymer-wrapped SWNTs *via* luminescent aryl defects. The proximity between the sp^3 defect and the unpaired electron of the radical permits spin exchange and electron transfer processes that are revealed through their impact on the PL decay dynamics of the defect-localized excited state.

In Chapter 6, the light emission of sp^3 functionalized SWNTs is studied in thin films and optoelectronic devices. First of all, the PLQY of defect-tailored SWNTs is compared in thin films and liquid dispersions. Subsequently, nanotubes with luminescent defects are embedded into planar dielectric waveguides and their potential for optical gain is evaluated. Finally, networks of functionalized SWNTs are integrated into light-emitting field-effect transistors to generate electroluminescence from sp^3 defects.

Chapter 7 concludes the thesis with a more general interpretation of the main results and provides perspectives for future work.

Chapter 2

Background

This Chapter covers the optoelectronic properties of single-walled carbon nanotubes and luminescent defects as well as the working principles of waveguides and light-emitting field-effect transistors.

2.1 Single-walled carbon nanotubes

Carbon nanotubes are hollow cylindrical structures of sp^2 hybridized carbon atoms with diameters on the order of 1 nm and typical lengths of several μm . Due to their high aspect ratio, they are considered as one-dimensional (1D) materials and thereby bridge the gap between zero-dimensional (0D) fullerenes and two-dimensional (2D) graphene in the family of carbon allotropes. While multi-walled nanotubes can occur by nesting several carbon shells into each other, single-walled carbon nanotubes (SWNTs) are of greater interest for optoelectronic applications thanks to their well-defined electronic and optical features. In the following Sections, the structure of SWNTs will be derived from that of graphene and their intrinsic electronic and optical properties discussed within a single-particle and an excitonic framework. Since the experiments discussed in this work were performed exclusively on (6,5) SWNTs, special emphasis will be placed on their properties, growth and purification. Finally, extrinsic effects in the form of lattice defects will be considered and their impact on the photoluminescence of semiconducting SWNTs reviewed.

2.1.1 Structure and synthesis

Since the properties of carbon nanotubes depend crucially on their precise atomic structure, a unique nomenclature for SWNTs is required. For this purpose, a carbon nanotube may be imagined as a rolled-up sheet of graphene. Figure 2.1a depicts the planar honeycomb lattice of graphene, which is built up of purely sp^2 hybridized carbon atoms. Each nanotube type is now defined by a circumferential roll-up vector \vec{C}_h , which connects pairs of carbon atoms that become coincidental upon rolling-up. The roll-up vector \vec{C}_h is then expressed as a linear combination according to

$$\vec{C}_h = n\vec{a}_1 + m\vec{a}_2 \quad (2.1)$$

where n and m are integers and \vec{a}_1, \vec{a}_2 the primitive lattice vectors of graphene with length $a = \sqrt{3}a_{C-C} = 0.246 \text{ nm}$ related to the carbon-carbon bond length $a_{C-C} = 0.142 \text{ nm}$. The pair of integers (n, m) is usually referred to as the chirality of a SWNT, irrespective of whether or not the nanotube structure is chiral in terms of symmetry.

Alternatively, a SWNT may be specified through combined information on its tube diameter d_t and chiral angle α , related to the chiral indices (n,m) by

$$d_t = \frac{|\vec{C}_h|}{\pi} = \frac{a}{\pi} \sqrt{n^2 + nm + m^2} \quad (2.2)$$

and

$$\cos \alpha = \frac{2n + m}{2\sqrt{n^2 + nm + m^2}} \quad (2.3)$$

The chiral angle α defines the roll-up direction \vec{C}_h with respect to the primitive lattice vector \vec{a}_1 . As a result of the symmetry of the honeycomb lattice, only chiral angles $0^\circ \leq \alpha \leq 30^\circ$ lead to unique nanotube structures. This gives rise to three classes of nanotubes, which are exemplified in Figure 2.1b. Zigzag SWNTs with $(n,0)$ and $\alpha = 0^\circ$ as well as armchair SWNTs with (n,n) and $\alpha = 30^\circ$ are achiral nanotubes. All other sets of (n,m) correspond to chiral SWNTs with their enantiomers given by (m,n) .

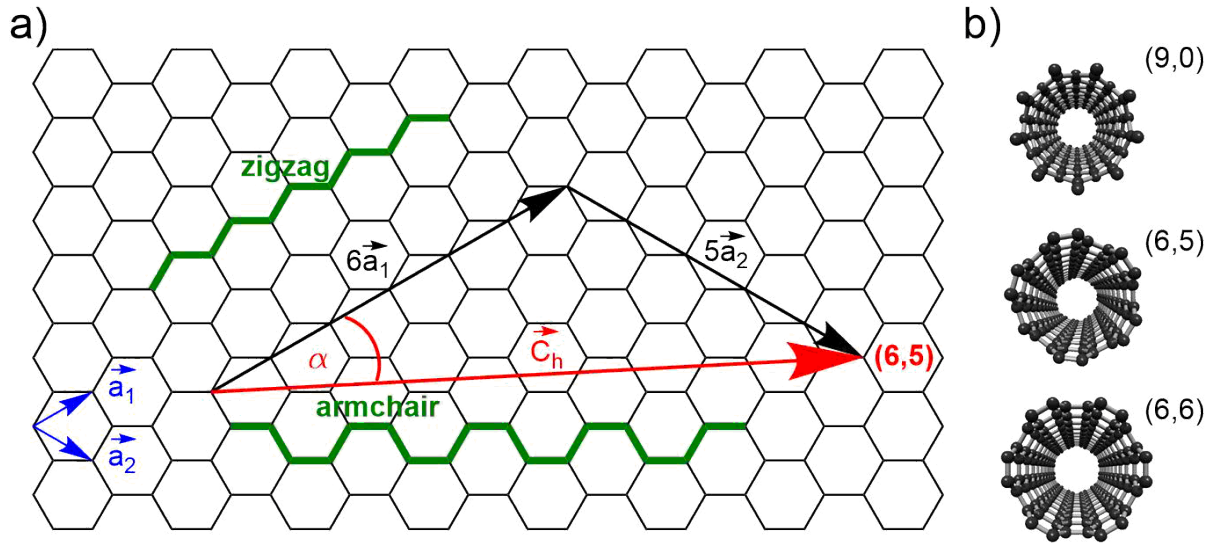


Figure 2.1: a) Definition of the SWNT structure by reference to the graphene sheet. b) Examples of zigzag (9,0), chiral (6,5) and armchair (6,6) SWNTs.

In addition, the translation vector \vec{T} may be introduced as the smallest graphene lattice vector orthogonal to \vec{C}_h . Hence, the length L_t of the nanotube may be expressed as a multiple of $|\vec{T}|$. As $L_t \gg d_t$, nanotubes are frequently modelled as infinitely long by imposing periodic boundary conditions on the lattice and thereby neglecting the tube ends. In reality, as-grown SWNTs are usually terminated by half-sphere-like

end-caps similar to fullerenes.²¹ In fact, tailored end-caps can be used as templates for the bottom-up synthesis of specific chiralities in a surface-catalyzed reaction.²² However, the very low yield and throughput of this method currently prevents its industrial application.

Today, the commercial production of SWNT raw materials is dominated by chemical vapor deposition (CVD) processes using gaseous carbon sources.²³ They are cheaper, more versatile and operate under milder conditions than other established growth methods that rely on the high-temperature conversion ($> 1000\text{ }^{\circ}\text{C}$) of graphite or carbon black by means of arc discharge,²⁴ laser ablation²⁵ or plasma treatment.²⁶ Among CVD approaches, the CoMoCAT process has emerged as the preferred route for growing small-diameter SWNTs ($d_t \sim 0.7 - 1.0\text{ nm}$) with narrow diameter distribution, including mostly (6,5) and (7,5) SWNTs.²⁷ Carbon for SWNT growth is provided by disproportionation of carbon monoxide on a silica- or magnesia-supported cobalt-molybdenum catalyst at typical temperatures of $700 - 950\text{ }^{\circ}\text{C}$ and pressures of $1 - 10\text{ atm}$. Subsequently, an acid treatment (hydrofluoric or sulfuric acid) removes the support material and releases the SWNTs.²⁸⁻³⁰

2.1.2 Chirality sorting

As will be shown in Section 2.1.3, SWNTs are either semiconductors or behave like metals depending on their specific chirality. Despite a certain selectivity in the growth process, all existing methods yield both semiconducting and metallic types of SWNTs.³¹ This issue is further complicated by the fact that all kinds of carbon nanotubes tend to aggregate into bundles as a result of strong van der Waals forces between the π conjugated nanotube sidewalls.³² Due to the fundamentally different electronic and optical properties of the different types of SWNTs, many applications require a post-growth separation of semiconducting and metallic SWNTs or even the isolation of single chiralities. Furthermore, the as-grown SWNTs still contain metallic catalyst particles, amorphous carbon and potentially other carbon allotropes, which must be removed. In the following, strategies for the purification of semiconducting SWNTs will be reviewed with the main focus on the extraction of single chiralities.

The purification is generally performed in the liquid phase and follows this outline: Firstly, the SWNTs must be de-bundled and stabilized against re-aggregation to create a stable colloidal dispersion. Only very few solvents³² (e.g. *N*-cyclohexyl-2-pyrrolidone) are able to disperse significant concentrations of SWNTs, so the addition of stabilizers is usually required. This dispersion step may be chirality-selective or not. Secondly, centrifugation is applied to sediment impurities and bundles of SWNTs, whereas well-individualized SWNTs can be collected from the supernatant. If necessary, this dispersion may be subjected to further sorting steps to narrow down the chirality distribution.

The first dispersions of mostly individualized SWNTs were obtained by vigorous sonication of nanotube raw material in an aqueous surfactant solution (e.g. sodium dodecyl sulfate or sodium cholate)³² followed by centrifugation.³³ However, harsh sonication conditions are known to damage the SWNT structure, shorten the average nanotube length³⁴ and open the tube ends, thus allowing solvent molecules to fill the tube.³⁵ In addition, this dispersion process is not chirality-selective and thus leads to a mixture of various semiconducting and metallic chiralities. Several methods have been employed to subsequently extract the desired nanotube species from these mixed dispersions, such as density gradient ultracentrifugation,³⁶ gel permeation chromatography³⁷ or dielectrophoresis.³⁸ More recently, the aqueous two-phase extraction (ATPE) method attracted considerable attention.³⁹ Here, polyethylene glycol and dextran are dissolved in water at suitable concentrations to create two immiscible phases with different hydrophobicity. The sorting method is based on the observation that SWNTs spontaneously enrich in one of the two phases depending on their tube diameter, electronic type and surfactant coating.⁴⁰⁻⁴² By iterative adjustment of solution parameters, such as the surfactant concentration, single chiralities can be selectively extracted over the course of multiple steps. To reduce the number of processing steps and to simplify the procedure, the dispersion pH can be used as an additional degree of freedom to control the surfactant coating on the SWNT surface without the need of changing the global surfactant concentration.⁴³ The strength of the ATPE approach lies in the preparation of nearly monochiral samples of small-diameter SWNTs, albeit there has been significant progress on the enrichment of large-diameter SWNTs as well.⁴⁴ Even though a purity of 99.5 % semiconducting SWNTs can be achieved after a few cycles

of ATPE, the residual content of metallic SWNTs hampers the performance of these samples in field-effect transistors^{44,45} and thus, ATPE-sorted SWNTs have been mainly used for spectroscopic studies.

However, when samples with exceptionally high purity of semiconducting SWNTs are needed, the polymer-wrapping approach is the method of choice.⁴⁶ First demonstrated by Nish *et al.*,⁴⁷ it relies on the chirality-selective adsorption of conjugated polymers to the nanotube sidewalls leading to colloidal stabilization of individual SWNTs in organic solvents. This sorting process is conceptually different from the previously discussed methods in that the dispersion step is chirality-selective itself. Typically, the SWNT raw material is added to a solution of the conjugated polymer in an organic solvent and subjected to sonication or shear forces to de-bundle the SWNTs. The conjugated polymer subsequently wraps around its preferred chiralities in the mixture and thus stabilizes them against re-aggregation, whereas poorly wrapped nanotubes quickly re-form bundles. Hence, the polymer-wrapped chiralities are easily separated from un-wrapped material by centrifugation. The most important classes of wrapping-polymers are polyfluorenes and their co-polymers,^{20,47-50} but polythiophenes^{51,52} and polycarbazoles⁵³ are frequently used as well. The π conjugated units are usually substituted by long alkyl chains to impart solubility in non-polar organic solvents, such as toluene or *ortho*-xylene. Interestingly, these conjugated polymers display a very high selectivity toward semiconducting chiralities, which makes polymer-sorted nanotubes highly attractive for electronic applications. For example, selective extraction using poly(9,9-di-*n*-dodecylfluorenyl-2,7-diyl)⁵⁰ or poly(2,5-dimethylidynenitrilo-3,4-didodecylthienylene)⁵¹ resulted in purities of semiconducting SWNTs of > 99.7% and > 99.85%, respectively. The structures of some widely used polymers for nanotube sorting are depicted in Figure 2.2.

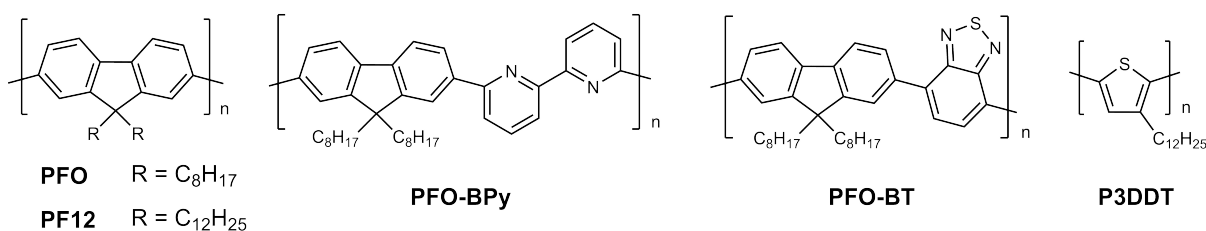


Figure 2.2: Molecular structures of conjugated polymers commonly used for chirality enrichment.

It is worth mentioning that conjugated polymers whose sidechains are terminated by charged functional groups, so-called conjugated polyelectrolytes (CPEs),⁵⁴ can be employed to disperse SWNTs in polar solvents, such as water or methanol.^{55–57} However, due to the enhanced colloidal stability of charged particles, CPEs usually display poor selectivity and cannot be used for chirality enrichment.⁵⁷

The structure of the formed polymer-SWNT hybrids has been investigated mainly by means of transmission electron microscopy^{55,56} and molecular dynamics simulations.^{49,56,58,59} Generally, the polymer chains are either aligned along the nanotube axis or they form helices around it. It was found that the conformation adopted by the wrapping polymer depends on both the polymer structure and the nanotube chirality. While polyfluorenes preferentially wrap near-armchair SWNTs in a helical fashion, their chains may align with the tube axis for SWNTs with smaller chiral angle.⁴⁹ Furthermore, the length of the alkyl side chains influences the yield and selectivity of the process. Longer alkyl chains lead to higher yields and allow for the extraction of SWNTs with larger diameters. Although the distribution of dispersed chiralities becomes broader with increasing side chain length, the selectivity for semiconducting SWNTs is retained.⁴⁹

Despite considerable theoretical efforts and knowledge of a large library of wrapping-polymers, the relationship between polymer structure and preferred chiralities is still not well understood. Furthermore, the polymer molecular weight and process parameters such as solvent viscosity and temperature⁵⁵ affect the selectivity of dispersion.⁶⁰ Beyond that, it has been suggested that the selective extraction of semiconducting SWNTs might be related to ambient p-doping rather than a higher affinity of the polymer to such chiralities.^{61,62}

Nevertheless, certain pairings of nanotube raw materials and conjugated polymers reliably produce dispersions that are highly enriched in only a few or even a single semiconducting SWNT type. One such case is the extraction of nearly monochiral (6,5) SWNTs from CoMoCAT raw material with the aid of PFO-BPy (see Figure 2.2) as reported by Ozawa *et al.* in 2011.⁶³ It is worth noting that PFO-BPy also disperses a broad range of large-diameter SWNTs ($d_t \sim 1.17 - 1.55$ nm) obtained from plasma torch growth,⁶⁴ but exhibits a strong preference for the (6,5) chirality among the small-diameter SWNTs present in the CoMoCAT raw material. In addition, polymer-sorting

can be combined with mild exfoliation methods that do not damage the nanotube structure as much as bath or tip sonication protocols do. Graf *et al.* introduced polymer-wrapping under shear force mixing as a gentle and scalable method to disperse SWNTs.²⁰ This approach made relatively large quantities of electronically-pure (6,5) SWNTs with long average tube lengths (1.8 μm) and low defect concentrations accessible and thereby provided the basis for the work conducted in this thesis.

2.1.3 Electronic structure

The roll-up formalism introduced in the previous Section is also a powerful approach to derive the electronic band structure of SWNTs from that of graphene. Since the graphene lattice is highly symmetrical with only two carbon atoms per primitive unit cell, the nearest-neighbor tight-binding method readily provides analytical approximations to its band structure.⁶⁵ The band structure can be further simplified by invoking electron-hole symmetry, *i.e.*, assuming that valence and conduction bands are mirror images about the intrinsic Fermi level. This is justified in the low-energy window around the Fermi level ($\pm 3\text{ eV}$) that is governed by the π and π^* bands, which dominate the electronic transport and optical excitations in the visible (vis) and near-infrared (NIR) range. Under these conditions, the energy dispersion of graphene reduces to

$$E(\vec{k}) = \pm\gamma\sqrt{1 + 4\cos\frac{\sqrt{3}a}{2}k_x\cos\frac{a}{2}k_y + 4\cos^2\frac{a}{2}k_y} \quad (2.4)$$

where \vec{k} is the wave vector, γ is the nearest-neighbor interaction energy (here, taken to be 3.1 eV⁶⁵) and the Fermi level was set to zero. Closer inspection of the graphene band structure (see Figure 2.3 below) reveals that the bands approach the Fermi level E_F only in the vicinity of the high-symmetry K (and K') points. In fact, the dispersion is linear in this region and the valence and conduction bands touch each other at the K point, which makes graphene a semi-metal or zero-band gap semiconductor.

In order to relate the band structures of SWNTs and graphene, the real space structure of SWNTs defined according to Figure 2.1 must be translated to reciprocal space. The reciprocity condition, $\exp[(\vec{K}_a + \vec{K}_c) \cdot (\vec{C}_h + \vec{T})] = 1$, yields the reciprocal lattice vectors along the tube axis (\vec{K}_a) and along the circumference (\vec{K}_c). The roll-up operation

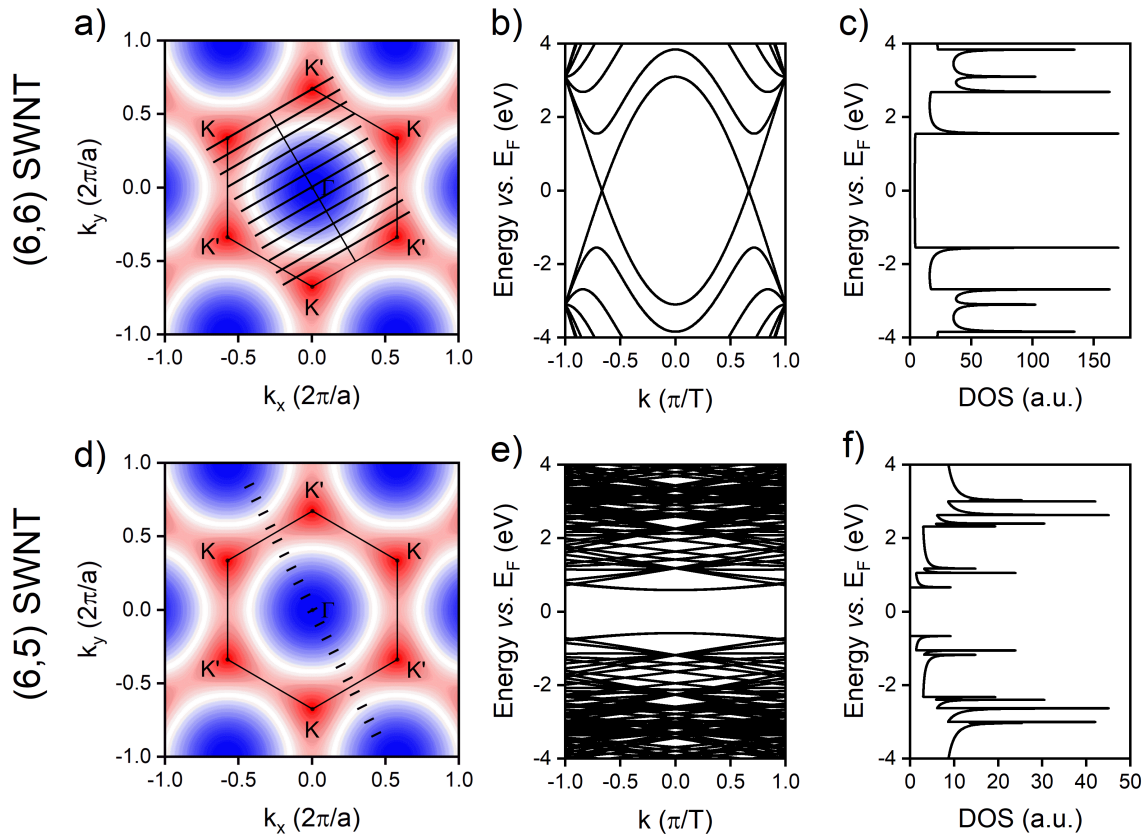


Figure 2.3: Tight-binding electronic structure of (6,6) and (6,5) SWNTs under the assumption of electron-hole symmetry. (a,d) The allowed wave vectors are shown as cutting lines of length $\frac{2\pi}{T}$ superimposed on the graphene band structure. Band dispersion (b,e) and density of states (DOS) distribution (c,f) for both nanotube types. Note that the DOS at the Fermi level is finite for the metallic (6,6) SWNT, but zero for the semiconducting (6,5) SWNT.

imposes a periodic boundary condition on the allowed wave vectors q in circumferential direction, which can only assume discrete values of $q = j|\vec{K}_c| = \frac{2\pi}{|C_h|}j = \frac{2}{d_t}j$, where $j = 0, 1, \dots, j_{max}$. Although periodic boundary conditions are analogously applied along the tube axis, the allowed wave vectors k in axial direction are a nearly continuous variable, because the high aspect ratio of practical SWNTs ($L_t \gg d_t$) leads to closely spaced k values. Consequently, the wave vectors of electrons or holes in SWNTs form a series of lines cutting through the Brillouin zone of graphene. Within this zone-folding approximation, the band structure of a SWNT is then given by the sum of 1D cuts (called sub-bands) through the band structure of graphene.

Figure 2.3 visualizes such cutting lines and compares the ensuing band structure and density of states (DOS) distribution for an armchair (6,6) SWNT and a chiral (6,5)

SWNT. As shown in Figure 2.3a & d, one of the lines for the (6,6) SWNT cuts through the K point, while none of the lines for the (6,5) SWNT intersects this critical point. Therefore, the (6,6) SWNT inherits metallic properties from graphene, whereas the (6,5) SWNT is a semiconductor. As the chiral indices (n,m) fully describe the SWNT structure, they also define its electronic type. In particular, if $(n - m)$ is zero or an integer multiple of 3, the cutting lines include the K point and the SWNT displays metallic behavior (Figure 2.3b). Otherwise, there is a band gap that makes the SWNT semiconducting (Figure 2.3e). A consequence of this simple rule is that armchair (n,n) SWNTs are always metallic. The band gap E_g of semiconducting SWNTs is primarily determined by the tube diameter d_t and less sensitive to the precise (n,m) . Hence, the formula $E_g = 2\gamma \frac{a_{C-C}}{d_t}$ is commonly employed to estimate the band gap.⁶⁵ Another important property of SWNTs is their DOS distribution $g_{tot}(E)$, which is defined according to

$$g_{tot}(E) = \sum_j g(E, j) = \sum_j \frac{1}{\pi} \left| \frac{\partial k}{\partial E} \right| \quad (2.5)$$

where the sum is over the sub-bands with index j . The 1D structure of SWNTs gives rise to a series of sharp features in the DOS distribution, called van Hove singularities, that govern the electronic and optical characteristics of the material. Note that the DOS around the Fermi level is finite for the metallic (6,6) SWNT (Figure 2.3c), whereas it is zero for the (6,5) SWNT (Figure 2.3f).

The semiconducting character of certain SWNT species enables light emission upon optical or electrical excitation, which will be the main focus of this work. Metallic carbon nanotubes, on the other hand, are promising candidates for conductive composites,⁶⁶ transparent, conductive thin films⁶⁷, interconnects for integrated circuits⁶⁸ or spin valves,⁶⁹ but do not show any light emission due to fast non-radiative carrier relaxation.

2.1.4 Excitons

The DOS distribution, introduced in the previous Section, is very useful in describing the electronic and optical properties of SWNTs. For example, it often provides the starting point for the modeling of charge⁷⁰ and thermoelectric transport.⁷¹ Furthermore,

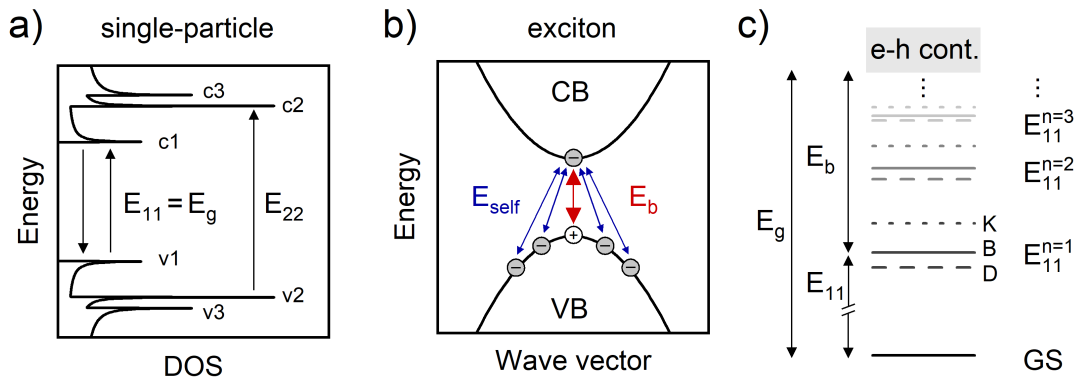


Figure 2.4: Excited states in semiconducting SWNTs within the single-particle and excitonic picture. (a) Optical transitions between van Hove singularities in the density of states (DOS). (b) Illustration of attractive electron-hole and repulsive electron-electron interactions in excitons. The excitonic correction to the band gap energy E_g is defined by the balance of exciton binding energy E_b and self-energy E_{self} . (c) Rydberg series of excitonic energy levels labeled by principal quantum number n on the example of the E_{11} exciton. Of the fine structure states, only the singlets $E_{11}(D)$, $E_{11}(B)$ and the 2-fold degenerate $E_{11}(K)$ are shown.

it can be used to estimate the energy of optical transitions in semiconducting SWNTs. Within the single-particle picture (Figure 2.4a), optical absorption in SWNTs corresponds to the transition of an electron from a van Hove (vH) singularity of the valence band ($v1, v2, \dots$) to a vH singularity of the conduction band ($c1, c2, \dots$). According to Fermi's golden rule,⁷² the transition rate at a given photon energy is proportional to the joint DOS, which is maximized for transitions between vH singularities. More specifically, the strongest transitions are expected between the i th vH singularity of the valence band (v_i) and the i th vH singularity of the conduction band (c_i), which will be labeled E_{ii} from now on. There are two reasons for this: First, the dipole selection rule applied to the symmetry of SWNTs dictates that only E_{ii} transitions are allowed for electric fields parallel to the tube axis, whereas E_{ij} transitions are allowed for electric fields perpendicular to the tube axis.⁷³ Second, due to their 1D structure, SWNTs display a pronounced antenna effect, *i.e.*, their absorption cross-section is much larger for light polarized parallel to the tube axis than for perpendicular polarization.⁷⁴ As a result, the E_{ii} transitions dominate the absorption spectrum and the energy of E_{11} simply corresponds to the band gap energy E_g . Analogously, electronically excited semiconducting SWNTs may relax radiatively and emit band gap photoluminescence (PL) *via* the E_{11} transition.

However, upon closer inspection, the single-particle picture of free photo-excited electrons and holes fails to reproduce the spectral position and shape of absorption bands in SWNTs.⁷⁵⁻⁷⁷ This is not surprising given that the electric field lines defining the attraction between electron and hole largely pass through vacuum owing to the 1D structure of SWNTs.^{78,79} In general, the energy of the excited state is lowered due to the attractive Coulomb interaction between electron and hole. While this interaction amounts to only a few meV in three-dimensional inorganic semiconductors,⁷² the weak dielectric screening in semiconducting SWNTs leads to binding energies E_b on the order of several 100 meV resulting in strongly bound electron-hole pairs called excitons (Figure 2.4b). On the other hand, the repulsive interaction between the excited electron and the electrons in the valence band raises the energy of the excited state by the self-energy term E_{self} . Hence, the E_{11} transition energy in the excitonic picture becomes $E_{11} = E_g + E_{self} - E_b$, where E_g is the single-particle band gap.⁷⁵

By analogy to the s, p, d, f, \dots states in a hydrogen atom, excitons feature a series of higher excited states E_{ij}^n denoted by the principal quantum number $n = 1, 2, 3, \dots$ that ultimately approach the unbound electron-hole continuum,⁸⁰ as shown for the E_{11} exciton in Figure 2.4c. In fact, two-photon excitation experiments accessing these higher-energy states experimentally verified the excitonic nature of the optical resonances in semiconducting SWNTs.^{81,82}

In carbon nanotubes, each excitonic level E_{ii}^n exhibits additional fine structure as indicated in Figure 2.4c. The degeneracy of the K and K' valleys of the underlying graphene lattice allows four distinct singly-excited configurations KK, K'K', KK' or K'K with the electron (hole) residing in the K(K) valley. In addition, the spins of the involved charge carriers produce 1 singlet and 3 triplet states for each of the valley configurations resulting in a total of 16 excitons for each E_{ii}^n series. However, as will be rationalized in the following, of all these excitons only a single state is optically bright, *i.e.*, accessible through a one-photon process from/to the ground state.

As the exciton wave vector is the vector sum of the electron and hole wave vectors ($\vec{K} = \vec{k}_e + \vec{k}_h$), it follows that the KK' and K'K intervalley excitons have a finite center-of-mass momentum of magnitude $|\vec{K}| = K$, whereas the intravalley excitons have $|\vec{K}| = 0$. Consequently, only intravalley excitations correspond to a direct (momentum-conserving) transition across the band gap of a SWNT (compare Figure 2.3e) and

thus, the intervalley (or K -momentum) excitons are optically dark. Furthermore, the zero-momentum excitons split into a bonding and an antibonding linear combination with odd and even parity, respectively.⁸³ Since the selection rules for a one-photon absorption/emission process require the initial and final states to have opposite parity, the even-parity zero-momentum exciton is dark as well. Finally, as the carbon atoms building up the SWNT display weak spin-orbit coupling, all triplet excitons are dark due to the requirement of spin conservation. Thus, only the zero-momentum, odd-parity singlet exciton is bright.

Despite being not directly observable by standard absorption or PL spectroscopy, dark excitons can become detectable in such experiments by coupling to phonons or under the influence of applied magnetic fields. Beyond that, their presence affects the dynamics and temperature-dependence of the PL from the bright state. Overall, these experiments provide an insight into the dark exciton manifold as discussed in the following.

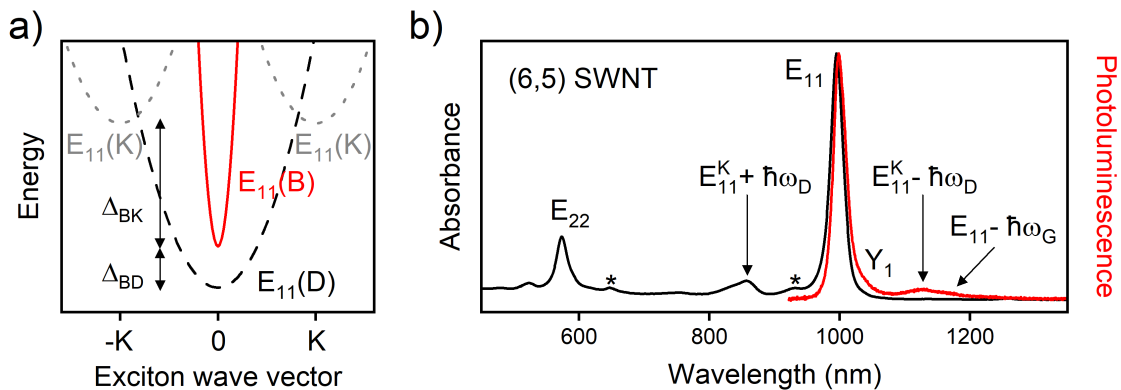


Figure 2.5: (a) Energy dispersion of singlet E_{11} states. (b) Absorption (black) and photoluminescence (red) spectra of (6,5) SWNTs with peak assignments. The asterisk (*) indicates impurity signals.

Figure 2.5a depicts the currently used model of the E_{11} singlet excitons. The parity-forbidden dark state ($E_{11}(D)$) is below the bright ($E_{11}(B)$) state, which leads to a decrease of E_{11} PL intensity at low temperatures ($< 50 - 100$ K depending on tube diameter).⁸⁴ The energy gap Δ_{BD} between them is only a few meV and was found to decrease with increasing tube diameter⁸⁵ in agreement with the theoretically expected relationship $\Delta_{BD} \propto 1/d^2$.⁸⁶ When a strong magnetic field is applied along the axis of the nanotube, the Aharonov-Bohm effect lifts the degeneracy of the K and K' valleys and brightens

the $E_{11}(\text{D})$ state.⁸⁵ Further, the splitting between the $E_{11}(\text{B})$ and $E_{11}(\text{D})$ state becomes field-dependent as $\Delta_{BD}(\vec{B}) = \sqrt{\Delta_{BD}^2 + \Delta_{AB}^2(\vec{B})}$, where Δ_{BD} and Δ_{AB} are the zero-field and the Aharonov-Bohm splitting, respectively. Δ_{AB} is linearly proportional to the magnetic flux $\Phi = (\pi d_t^2/4)|\vec{B}|\cos(\phi)$ threading the tube with diameter d_t which makes an angle ϕ with the magnetic field \vec{B} . The zero-field splitting Δ_{BD} can thus be obtained from extrapolation to $|\vec{B}| = 0$.

The K -momentum excitons ($E_{11}(\text{K})$ in Figure 2.5a) are degenerate and located above the bright state with a larger energy gap Δ_{BK} of about 25 meV.^{87,88} These excitons play an important role even under ambient conditions, as radiative transitions from (to) the ground state are allowed under absorption (emission) of a D phonon with a momentum of K . The energetic position of the K -momentum excitons is then identified as the center between the absorptive and the emissive sideband (compare Figure 2.5b). While substantial information is available on dark singlet excitons, triplet excitons are still poorly understood. The energies of E_{11} triplets extracted from calculations or experiments vary strongly between studies.^{89–92} Recently, the detection of phosphorescence from several SWNT chiralities by means of optically-detected magnetic resonance (ODMR) spectroscopy⁹³ showed reasonable agreement with calculations by Capaz *et al.*⁸⁹ and the diameter-dependence of the singlet-triplet splitting Δ_{BT} was confirmed to be $\propto 1/d^2$. Apart from that, the triplet exciton population can be monitored through transitions into higher excited triplets ($T_1 \rightarrow T_n$) as observed in transient absorption measurements.⁹⁴ Finally, it was reported that triplet excitons can become optically active at cryogenic temperature upon deposition of the ferromagnetic semiconductor europium sulfide onto the SWNT.⁹⁵

The spectral features arising from the allowed optical transitions are discussed in the following, using absorption and PL spectra of (6,5) SWNTs (Figure 2.5b). The absorption spectrum shows the E_{11} transition in the near-infrared (~ 1000 nm) with narrow line width (~ 25 meV) and the E_{22} transition in the visible range (~ 575 nm). Upon absorption into a higher excited state, such as the E_{22} exciton, fast internal conversion (~ 100 fs⁹⁶) leads to population of the E_{11} band-edge exciton manifold. The radiative decay of the bright $E_{11}(\text{B})$ exciton then gives rise to E_{11} PL with an extremely small Stokes shift (~ 6 meV) that is associated with the rigid SWNT structure and thus, small reorganization energy.⁹⁷ Furthermore, there is a pronounced sideband in

absorption (PL) arising from the excitation (decay) of the K -momentum dark exciton under absorption (emission) of a D phonon.^{87,88} The weaker PL sideband is interpreted as a vibronic transition of the bright E_{11} (B) exciton coupled to the G phonon.⁸⁸ In addition, the E_{11} signal displays a low-energy shoulder (Y_1) that is suspected to be of extrinsic origin and might be related to excitons interacting with lattice defects.⁸⁸

In general, carbon nanotubes can host a broad range of unintentional lattice defects created during growth or subsequent processing.⁹⁸ The vast majority of these defects leads to exciton quenching upon diffusive encounter and is therefore optically dark. A few particular arrangements of sp^3 defects in the SWNT sidewall, however, are known to introduce new optically-active states that exhibit bright PL. Over the past years, synthetic methods were developed which selectively target such luminescent defect configurations. The next Section covers in detail their synthesis, the interaction of excitons with them as well as the ensuing optical properties.

2.2 Luminescent defects

Soon after the first dispersions of individualized, and thus luminescent, semiconducting SWNTs had become available,³³ lattice defects were identified as a source of non-radiative exciton quenching limiting the photoluminescence quantum yield (PLQY) in SWNTs.^{99–101} In stark contrast to that, Piao *et al.* reported the striking observation of a new luminescence feature with substantially higher PLQY than the E_{11} transition upon introduction of synthetic sp^3 defects.¹⁰² The origin of this brightening effect lies in the localization of otherwise highly mobile excitons at defect sites followed by efficient radiative relaxation.^{103–105} Theoretical studies suggest that the precise binding pattern of molecular groups on the nanotube lattice is crucial for the luminescence properties of such defects.^{106–108} Recently, luminescent defects (sometimes also referred to as quantum defects or organic color centers) were extensively reviewed^{7–9} because of their highly attractive optical properties including enhanced PLQYs¹⁰² and room-temperature single-photon emission in the NIR.¹⁴ The following discussion of sp^3 defects begins with exciton diffusion as the population mechanism of defect states before addressing their structure-dependent optical properties and synthetic approaches to create them.

2.2.1 Exciton diffusion

Before excitons can interact with lattice defects, they must diffuse to the defect site. It is worth noting that diffusion is only considered on the level of the band-edge E_{11} excitons as internal relaxation from higher-energy excitons is much faster than diffusion.⁹⁶ The mechanism of exciton diffusion in SWNTs depends on their environment. In air-suspended SWNTs, which can be considered as near-ideal pristine nanotubes, the exciton transport is mediated by scattering with acoustic phonons.¹⁰⁹ In that case, the exciton diffusion constant is given by $D = \langle v^2 \tau_{dp} \rangle$, where $v(K) = \hbar^{-1} \frac{\partial E}{\partial K}$ is the exciton group velocity and τ_{dp} is the pure dephasing time determined by the frequency of scattering events.¹¹⁰ From the dependence of D on the exciton dispersion $E(K)$, it becomes clear that bright excitons diffuse faster than dark excitons by virtue of their smaller effective mass (compare Figure 2.5a). Under such intrinsic conditions, the diffusion constant was also found to scale with the tube diameter according to $D \propto d_t^{2.5}$ matching theoretical predictions.^{109,111}

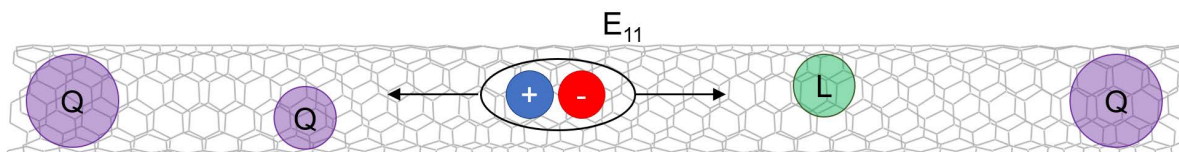


Figure 2.6: Diffusion of the band-edge E_{11} exciton along the nanotube axis. Non-radiative quenching sites and luminescent defects are labeled by Q (purple) and L (green), respectively.

In contrast to that, exciton transport in colloiddally dispersed SWNTs is limited by scattering with the disordered surface potential defined by the surfactant and solvent shell. Here, the relation $D = v\Lambda$ can be used to deduce the mean free path Λ from a known diffusion constant. A mean free path of $\Lambda \sim 1.5$ nm was obtained for a surfactant-stabilized aqueous dispersion of (6,5) SWNTs.¹¹⁰ The extracted diffusion constants are generally on the order of $1\text{-}10 \text{ cm}^2 \text{ s}^{-1}$,^{101,110,112} which allow the exciton to explore a tube segment of ~ 100 nm within only ~ 10 ps. Hence, for tube lengths of around $1 \mu\text{m}$ just a few defects already result in a large probability of interaction with the exciton. On top of that, the sonication treatment used to de-bundle the SWNTs is known to damage the end-caps of as-grown SWNTs and to lead to open and disordered tube ends.³⁵ Unfortunately, most types of lattice defects, including the tube ends, lead

to exciton quenching and thus, limit the photoluminescence quantum yield (PLQY) of solution-processed SWNTs to about $\sim 1\%$.¹⁰¹

On the other hand, fast diffusion can also funnel excitons to luminescent defects,¹⁰³ if any are present. As illustrated in Figure 2.6, the competition between diffusion to non-radiative (Q) and radiative (L) recombination sites is one of the key aspects defining the PLQY in SWNTs with emissive defects.

2.2.2 Exciton localization

The common feature of all luminescent defects is that they introduce a significant sp^3 character (larger than that due to nanotube curvature) to the carbon atoms binding the attached molecular groups in an otherwise nearly sp^2 hybridized lattice. This local symmetry-breaking creates new optically-active excitonic states below the E_{11} exciton.¹⁰⁶ More specifically, the degeneracy of the K and K' valleys is lifted, resulting in a large energy splitting between the $E_{11}(B)$ and the $E_{11}(D)$ excitons that correspond to the odd- and even-parity linear combinations of KK and K'K' excitons and are nearly degenerate in pristine SWNTs ($\Delta_{BD} \sim 5$ meV). In addition, the former dark state gains substantial oscillator strength as it is no longer parity-forbidden. Figure 2.7 illustrates the splitting into a stabilized E_{11}^* and a destabilized E_{11}^{up} state.¹⁰ Since the new E_{11}^* state lies energetically well below the bright $E_{11}(B)$ exciton, the excitation is trapped, *i.e.* localized, in the low-energy E_{11}^* state upon diffusive encounter with the defect. This leads to emergence of E_{11}^* emission at the expense of intrinsic E_{11} PL.

Due to the depth of the trapping potential (~ 100 meV¹¹³), the excitons remain localized at the sp^3 defect even at room temperature and thus, diffusion to non-radiative quenching sites is ruled out for them. Without the limitation of diffusive quenching, the PLQY of the defect-associated E_{11}^* transition is determined by the radiative and non-radiative decay rates of the localized exciton, which can enable substantially brighter emission compared to the intrinsic E_{11} transition.^{102,104}

2.2.3 Optical properties

Upon optical excitation at the E_{11} transition or above, the high oscillator strength of the nanotube host¹¹⁴ leads to efficient light absorption and creation of E_{11} excitons that are

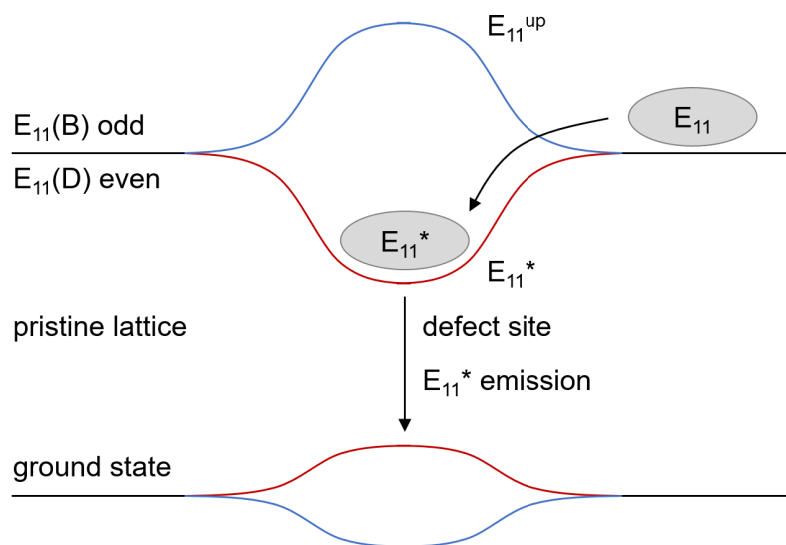


Figure 2.7: Local symmetry-breaking leads to energetically low-lying bright states that can trap the E_{11} exciton. Radiative relaxation from this state gives rise to E_{11}^* emission. The color code connects states of opposite symmetry, between which parity-allowed optical transitions exist.

diffusively transported to sp^3 defects.¹⁰³ Since the defect state is energetically below the band-edge exciton, the E_{11}^* PL transition is red-shifted from the E_{11} transition, as shown in Figure 2.8a. Furthermore, the photoluminescence excitation (PLE) spectrum¹¹⁵ of the sp^3 functionalized SWNTs is nearly identical to that of pristine SWNTs owing to the low density of defect sites and population of defect states through diffusion of E_{11} excitons.

In order to understand the origin of efficient E_{11}^* emission, the radiative and non-radiative relaxation pathways¹⁰⁵ must be considered (Figure 2.8b). For both pristine SWNTs^{86,116} and sp^3 defects,^{105,117} theory predicts radiative lifetimes on the order of 1-10 ns. However, the observed room-temperature PL lifetime in solution-processed SWNTs is usually on the order of 10 ps and thus limited by non-radiative quenching resulting in a PLQY of only $\sim 1\%$.^{101,104} Due to the absence of diffusive quenching for defect-localized excitons, their lifetime is substantially longer and commonly in the range of a few 100 ps,^{104,105} which reflects the higher emission efficiency of sp^3 defects. Systematic variation of nanotube chirality,^{102,104} exciton trapping potential,¹⁰⁴ solvent environment¹⁰⁵ and temperature¹¹³ was used to identify the main relaxation pathways of excitons trapped at sp^3 defects.

Since exciton localization at sp^3 defects leads to enhanced exciton-phonon coupling,¹¹⁸ multi-phonon decay (MPD) is the main non-radiative relaxation pathway for trapped

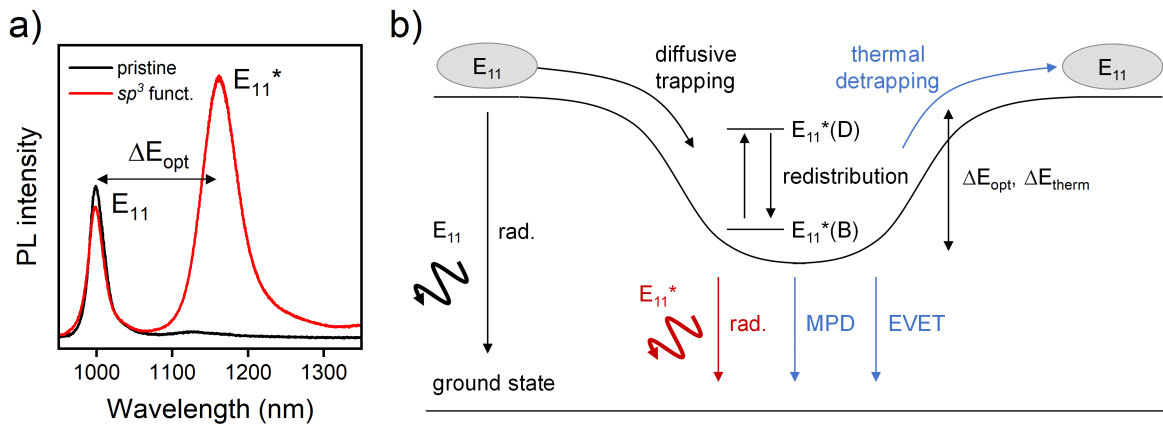


Figure 2.8: (a) PL spectra of pristine and sp^3 functionalized (6,5) SWNTs. (b) Schematic of exciton dynamics at sp^3 defects following the model by He *et al.*¹⁰⁵ Non-radiative loss channels and E_{11}^* emission are indicated by blue and red color, respectively.

excitons.¹⁰⁴ As the number of phonons needed to bridge the optical gap (here, E_{11}^*) drops, the MPD rate increases and leads to a shorter E_{11}^* PL lifetime. This trend is most prominent when different nanotube chiralities functionalized with the same defect type are compared.¹⁰⁴ If the radiative relaxation rate is assumed to be chirality-independent, defects in larger-diameter SWNTs with lower E_{11}^* energy should be less efficient emitters. The limited PLQY data available in the literature indeed matches this expectation.¹⁰²

If the sp^3 functionalized SWNTs are dispersed in a solvent (or embedded in a matrix) with high absorption cross-section over the spectral range of defect emission, Förster-type resonant energy-transfer from the defect to the surrounding molecules can occur.¹⁰⁵ Because of the low energy of E_{11}^* emission (~ 1 eV), the acceptor state is usually associated with an infrared-active combination vibration and hence, the process is referred to as electronic-to-vibrational energy transfer (EVET).^{119,120} Such molecular vibrations are often present in polar solvents like water or methanol and explain the shorter E_{11}^* PL lifetime and lower emission efficiency in these media.¹⁰⁵

To a first approximation, the depth of the exciton trapping potential may be assumed to be the energy difference between the E_{11} and E_{11}^* PL transitions (Figure 2.8a), which is called the optical trap depth (ΔE_{opt}). However, temperature-dependent PL measurements have shown that the thermal detrapping energy (ΔE_{therm}) is generally smaller than the optical trap depth.¹¹³ While ΔE_{therm} is still around 100 meV for (6,5) SWNTs, it is substantially smaller than the corresponding ΔE_{opt} of about 170 meV. It

has been suggested that the energy difference $\Delta E_{opt} - \Delta E_{therm}$ should be interpreted as a reorganization energy (ΔE_{reorg}) that reflects the deformation of the local SWNT structure upon exciton trapping at an sp^3 defect.¹¹³ Despite the large ΔE_{therm} , thermal detrapping (TD) is not negligible at room temperature and manifests itself through an increase of PL lifetime for longer-wavelength defect emission associated with deeper exciton traps.¹⁰⁵

Similar to the intrinsic E_{11} emission, the defect luminescence arises from a single bright state (for each binding configuration, as described in Section 2.2.4). Nevertheless, several dark states exist at energies close to that of the bright state. As a result, these states can drain exciton population from the bright defect state and thus weaken the E_{11}^* emission.¹⁰⁵ Theoretical and experimental studies suggest that the energetic ordering of bright and dark states depends on the type of defect.^{107,113,121,122} While the lowest-energy singlet in aryl- or alkyl-substituted sp^3 defects is bright, it is likely dark in oxygen defects.

The non-radiative loss channels discussed above combine to a cumulative decay rate

$$\tau_l^{-1} = \tau_{MPD}^{-1} + \tau_{EVEET}^{-1} + \tau_{TD}^{-1} + k_{other} \quad (2.6)$$

where k_{other} denotes all remaining irreversible decay pathways including radiative recombination.¹⁰⁵ At cryogenic temperature, the temporal decay of E_{11}^* PL is typically mono-exponential with rate τ_l^{-1} .^{123,124} At room temperature, on the other hand, the available thermal energy is sufficient to enable a fast and reversible exchange of exciton population among bright and dark defect states. The populations of the involved states then relax toward their equilibrium values with rate k_{BD} . As recombination can occur simultaneously at any time, the fast decay component due to population redistribution is given by¹⁰⁵

$$\tau_s^{-1} = k_{BD} + \tau_l^{-1} \quad (2.7)$$

Hence, the E_{11}^* PL decay becomes bi-exponential once the thermal energy is comparable to the energy gap between bright and dark excitons.

One of the most important implications of the deep exciton traps created by sp^3 defects is the ensuing single-photon emission behavior at room temperature and in the near-

infrared.^{14,125} The zero-dimensional defect acts as a two-level system that can only switch between a singly occupied and an unoccupied state and therefore results in high single-photon purity. Even though the intrinsic dephasing time of the localized exciton is two orders of magnitude shorter than its radiative lifetime,¹¹⁷ Purcell enhancement *via* coupling to plasmonic nanocavities can speed up the radiative decay such that indistinguishability of the emitted photons is achieved.¹⁵

Another aspect of the two-level character of luminescent defects is their low-threshold emission saturation due to state-filling.¹²⁶ As exciton diffusion populates defect states within ~ 10 ps, but the lifetime of the trapped exciton is ~ 100 ps, only moderate exciton densities, and thus pump powers, are needed to occupy a significant number of defects on a SWNT with one exciton. Consequently, the probability of exciton trapping followed by radiative relaxation decreases with increasing exciton density and the E_{11}^* -to- E_{11} intensity ratio becomes highly pump power-dependent.

2.2.4 Role of defect structure

So far, the arrangement of sp^3 defects on the nanotube lattice and the nature of the functional groups was largely neglected. In general, it is assumed that two molecular groups are added to the conjugated π system to produce a charge-neutral and closed-shell structure. Theoretical and experimental studies have shown that the relative position of the two created sp^3 carbon atoms are crucial for the electronic and thus also optical properties of the defect state.^{107,127} In the following, functionalization will be assumed to proceed *via* a radical addition mechanism, but the same rationale applies to an ionic mechanism. Upon addition of the first radical fragment to a carbon-carbon π bond, electron pair resonance delocalizes an unpaired electron over the *ortho* and *para* positions as illustrated in Figure 2.9a. Subsequently, one of these reactive sites binds a second radical fragment to yield a stable closed-shell structure with fixed configuration.

Each of these structures is associated with an optically-active defect state at a distinct energy.¹⁰⁷ The presence of multiple defect species in an ensemble of sp^3 functionalized SWNTs is a major source of spectral diversity that can be observed in single nanotube experiments at low temperature.¹²⁸ According to the currently accepted picture,¹²⁷

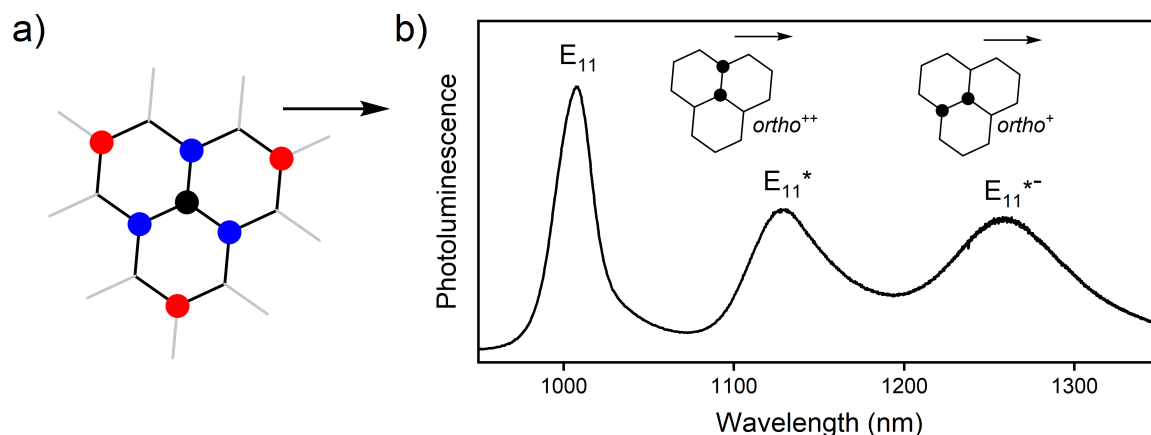


Figure 2.9: (a) Binding configurations for the addition of molecular fragments to the (6,5) nanotube lattice. Once the first fragment (black) is added to the lattice, the second fragment may bind to one of the corresponding *ortho* (blue) or *para* (red) positions. The orientation of the nanotube axis is indicated by the arrow. (b) PL spectrum of a (6,5) SWNT functionalized with two types of sp^3 defects that are arranged in the $ortho^{++}$ and $ortho^+$ configurations responsible for the distinct E_{11}^* and E_{11}^{*-} emission signals.

ortho arrangements are preferred and the two prevalent configurations in chiral SWNTs are the $ortho^{++}$ and $ortho^+$, which give rise to the E_{11}^* and E_{11}^{*-} emission features, as shown in Figure 2.9b. While it is conceivable that electron pair resonance places the sp^3 carbon atoms farther apart, these structures are predicted not to be luminescent.¹⁰⁶ To date, it is not known whether the second functional group is commonly derived from the employed reagent or the solvent. Calculations compared two cases: Either the second group is identical to the first, *e.g.*, an aryl radical, or it is a hydrogen atom abstracted from the solvent. Since it was found that both structures yield very similar defect state energies, this aspect is expected to play only a minor role.¹⁰⁷

Moreover, it was found that for a given binding configuration, more electron-withdrawing functional groups lead to farther red-shifted emission due to enhanced electrostatically induced exciton localization (Figure 2.10).^{102,108,129} Beyond that, the hybridization of the (aryl or alkyl) carbon atom on the attached moiety affects the defect state energy and a lower *s* character shifts the emission to longer wavelengths as observed for divalent functional groups.¹⁰⁸ As the difference in optical transition energies between the $ortho^{++}$ and $ortho^+$ configurations is > 50 meV, whereas substituent-related shifts are typically < 25 meV, it may be concluded that the binding configuration dominates the defect state properties.

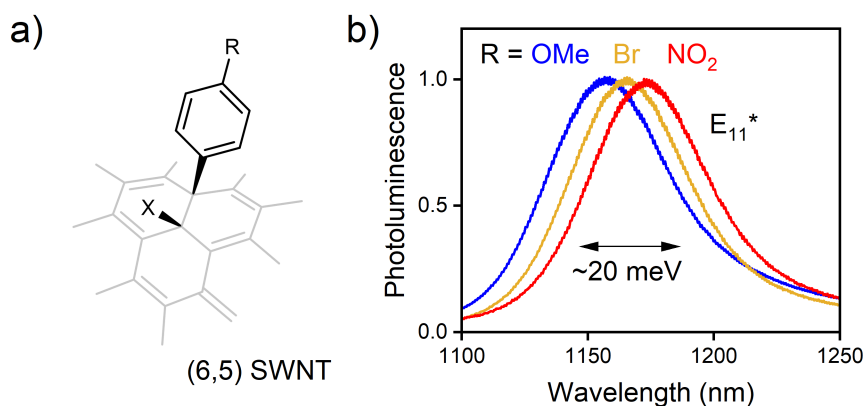


Figure 2.10: (a) sp^3 Defects created by attachment of an arene with *para* substituent R and a second group X of unknown chemical structure. (b) As the electron-withdrawing character of the substituent R increases along the series OMe < Br < NO₂, the E_{11}^* is progressively more red-shifted.

2.2.5 Covalent functionalization of SWNTs

As described above, covalent functionalization creates low-energy emissive states owing to perturbation of the SWNT's electronic structure. An important requirement for efficient defect luminescence is that the sp^3 functionalized sites must be spatially well-separated. In this low-density regime, the defect-associated E_{11}^* PL increases with defect density.¹⁰² However, once the nanotube lattice becomes too disordered due to disruption of the conjugated π system, the E_{11}^* PL drops sharply and ultimately vanishes.¹⁰⁰ Hence, defect emission is only observed within a narrow defect density window, which is the reason why it was overlooked for a long time and defects were believed to universally quench the PL of SWNTs.

It follows that the creation of emissive defects requires synthetic methods that enable precise control of the defect density. Figure 2.11 provides an overview of commonly employed synthetic routes to luminescent defects. Note that this list is by no means exhaustive and new methods keep being added.^{130,131}

The vast majority of functionalization reactions that are known to produce emissive defects proceed in aqueous dispersion and are therefore limited to surfactant-stabilized nanotubes sorted by gel permeation chromatography or aqueous two-phase extraction (see Section 2.1.2). The first unambiguous observation of luminescent defects was made on ozone-treated SWNTs (Figure 2.11a).¹⁰ It is assumed that ozonation produces

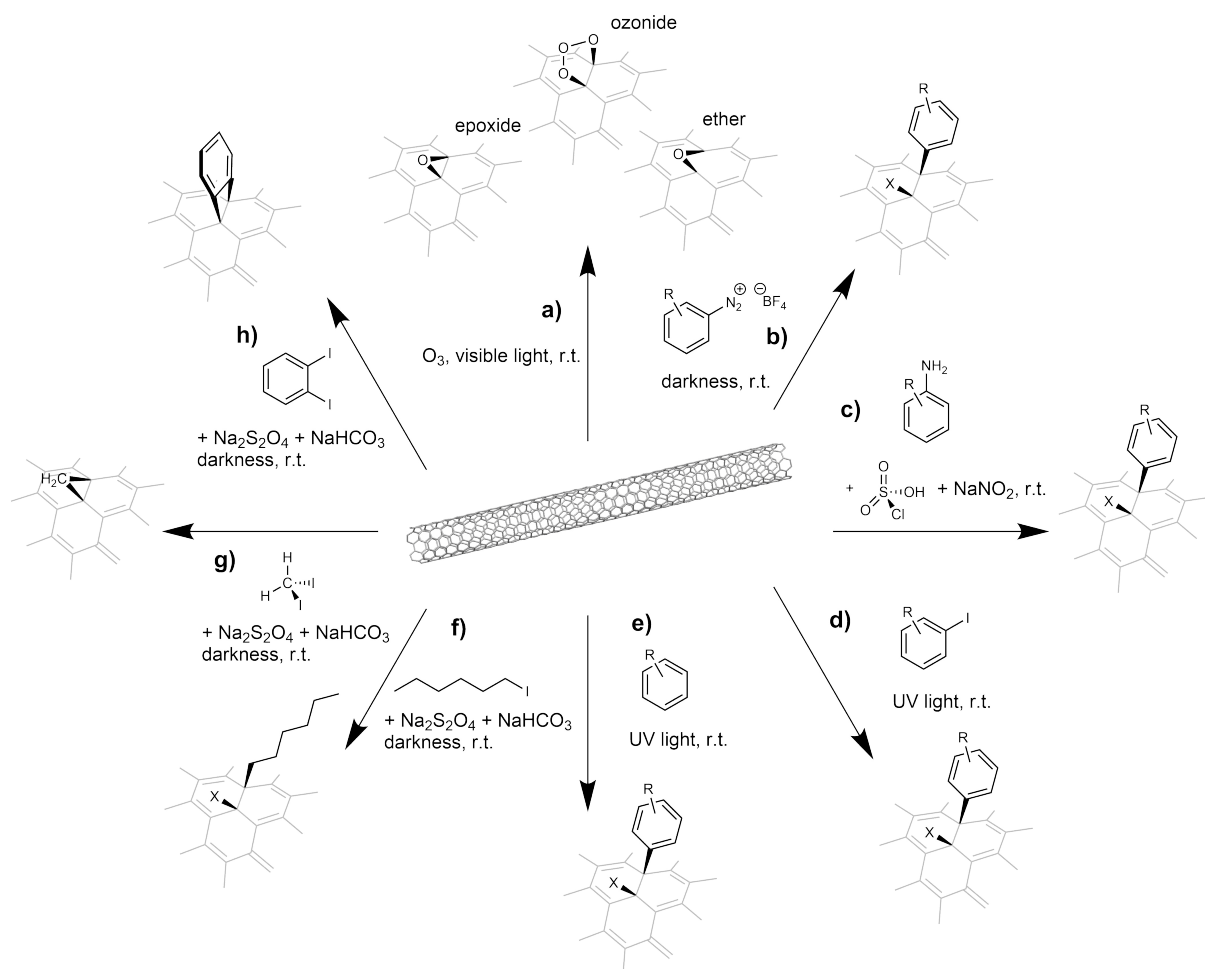


Figure 2.11: Selected synthetic routes to luminescent defects in SWNTs. (a) Ozonation;^{10,115} (b) reaction with pre-formed aryldiazonium salts;¹⁰² (c) superacid-promoted dispersion and *in situ* generation of diazonium salts; UV light-induced activation of (d) aryl halides¹³² or (e) nitroarenes and aminoarenes;¹³³ Coupling with (f) alkyl iodides, (g) alkylene diiodides or (h) arylene diiodides under reducing conditions.¹²⁹

oxygen defects *via* ozonide intermediates, which subsequently decompose to epoxides or ethers.^{10,121} To scale up the process and avoid the use of ozone, a modern approach utilizes sodium hypochlorite as the oxidizing agent in a flow cell under ultraviolet (UV) irradiation.¹³⁴

Due to the synthetic tunability and the often brighter defect emission, the covalent attachment of aryl or alkyl groups to SWNTs has received more attention than the oxygen functionalization.^{7,9,135} The classical route to sp^3 functionalization of nanotubes with aryl groups makes use of diazonium chemistry (Figure 2.11b) and was investigated in some detail.^{136,137} It is likely that the conjugated system is attacked by an aryl radical, which is formed either in a Gomberg-Bachmann reaction¹³⁸ or through a single-electron

transfer from the nanotube to the diazonium salt followed by release of N_2 . A drawback of the diazonium route is the relatively slow reaction that often takes several hours or even days at room temperature,¹⁰² although there are reports of enhanced reaction rates upon irradiation with visible light.^{139,140} It was also shown that nanotube dispersion and sp^3 defect creation can be combined in a one-pot process (Figure 2.11c), in which a diazonium compound is generated *in situ* from an aromatic amine.¹⁴¹

Since diazotation is not always compatible with sensitive functional groups and the resulting compounds have limited shelf life, photo-activation by UV light has been explored as a way to enable the reaction with otherwise inert aryl compounds. For example, aryl iodides readily react with SWNTs under UV illumination (Figure 2.11d).¹³² Interestingly, amino- and nitroarenes also introduce sp^3 defects under such conditions (Figure 2.11e), but the molecular structure of these defects as well as the mechanistic pathway are not completely clear.¹³³

In order to attach alkyl groups to SWNTs, alkyl iodides can be activated by the reducing agent sodium dithionite (Figure 2.11f).¹²⁹ This route is very versatile as it permits the use of aryl iodides and diiodides as well. In case of alkyl diiodides (Figure 2.11g), so-called divalent defects are accessible,¹²⁹ in which the attached group binds to two neighboring carbon atoms of the SWNT lattice, thereby removing the need for an auxiliary group X. Due to constraints on the bond angles, the *ortho*⁺⁺ binding configuration is strongly favored in such defects, thus leading to reduced spectral diversity.¹⁰⁸ Analogously, aryl diiodides may be employed to create divalent aryl defects (Figure 2.11h).¹²⁹ Because of the different bond character, most notably hybridization, the spectra of divalent defects are distinctly shifted from their monovalent analogs.^{108,129}

It is worth mentioning that in some cases the sp^2 character of the pristine nanotube lattice is retained after covalent functionalization and thus, the optical properties of the SWNT are not modified, *i.e.*, the intrinsic E_{11} emission is not quenched. Such a scenario was observed for the [2+1] cycloaddition of nitrenes to SWNTs followed by rearrangement to an open, ether-like configuration with sp^2 hybridized binding sites.¹⁴² In this way, the interaction of quasi-pristine SWNTs with a broad variety of covalently bound molecules may be studied without the anchor point affecting the electronic structure of the nanotube.¹⁴³

2.3 Waveguides

In order to harness the luminescence of a material for technological applications, the emitted light must be efficiently collected and channeled in the desired propagation direction. Structures that serve this purpose are generally termed optical waveguides^{144,145} as they guide the light waves in a specific direction. One of the most common structures for transmission in the UV-vis-NIR range is the planar dielectric waveguide (Figure 2.12), in which a dielectric layer with high refractive index n_f (the core) is sandwiched between two layers of low refractive indices $n_s, n_c < n_f$ (the cladding). Within this structure, light is confined to the high-index core where it propagates *via* total internal reflection (TIR) from the interfaces between core and cladding.

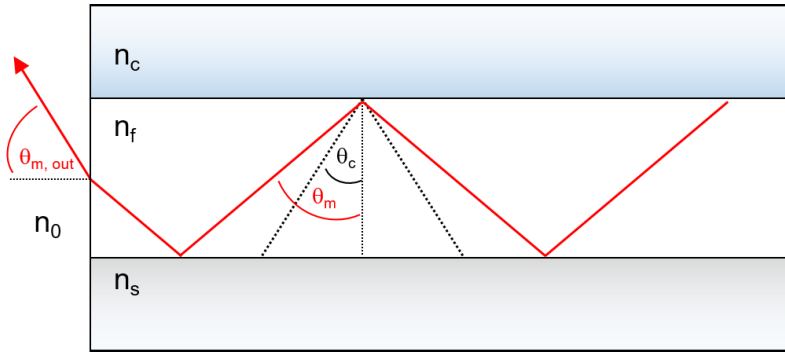


Figure 2.12: General layout of a planar dielectric waveguide. The refractive index of the core must be larger than that of the substrate and the cover, *i.e.*, $n_f > n_s, n_c$, and $\theta_m > \theta_c$. Note the refraction of the light ray upon out-coupling to the surrounding medium of low refractive index n_0 .

TIR requires that the bounce angle of a light ray is larger than a critical angle $\theta_c = \arcsin \frac{n_s/c}{n_f}$, where n_s and n_c apply to the respective interface. Since the wave is reflected repeatedly between the two interfaces, a guided mode can only be sustained if it interferes constructively with itself. In other words, such modes must satisfy the transverse resonance condition¹⁴⁵

$$\frac{2\pi}{\lambda} n_f d \cos \theta_m - \phi_s - \phi_c = m\pi \quad (2.8)$$

where λ is the wavelength of light, d the core thickness, θ_m the bounce angle of mode $m = 0, 1, 2, \dots, M$ and ϕ_s/c are the phase shifts associated with TIR at the core/substrate and core/cover interface, respectively. As the phase shift for modes with transverse electric polarization is given by¹⁴⁵

$$\tan \phi_{s/c} = \frac{\sqrt{n_f^2 \sin^2 \theta_m - n_{s/c}^2}}{n_f \cos \theta_m} \quad (2.9)$$

Equation 2.8 is transcendental and must be solved numerically or graphically to obtain the set of allowed modes and their corresponding bounce angles θ_m .

Depending on whether the waveguide structure is symmetric, *i.e.* $n_s = n_c$, or asymmetric with $n_s \neq n_c$, the characteristics of guided modes are markedly different. For instance, in symmetric planar waveguides, modes with transverse electric (TE) and transverse magnetic (TM) polarization are degenerate, whereas they feature distinct propagation constants in the asymmetric case. Furthermore, symmetric waveguides always support a fundamental guided mode ($m = 0$) irrespective of d and λ and only higher order modes ($m > 0$) are subject to a wavelength cut-off condition. In asymmetric waveguides, on the other hand, even the fundamental mode may be cut off unless the ratio d/λ is sufficiently large. More precisely, the core thickness d must fulfill¹⁴⁶

$$d > \frac{\lambda}{2\pi \sqrt{n_f^2 - n_s^2}} \arctan \sqrt{\frac{n_s^2 - n_c^2}{n_f^2 - n_s^2}} \quad (2.10)$$

for the $m = 0$ TE mode to propagate at wavelength λ . Hence, the core thickness must be carefully controlled and smooth interfaces with the substrate and cover are required to achieve low-loss light transmission.

Asymmetric planar dielectric waveguides are of great practical relevance as they are encountered in many applications including optical amplifiers and lasers,¹⁴⁷ photonic circuits¹⁴⁸ and luminescent solar concentrators.^{149–151} The coupling of luminescence from single-walled carbon nanotubes into waveguides was demonstrated in various architectures under optical^{152–154} or electrical^{148,155} excitation. Given the recent emergence of high-purity single-photon emission from sp^3 functionalized SWNTs at telecommunication wavelengths,¹⁴ waveguide-integration represents the next step toward their application in fiber-based optical communication.¹⁵⁶ Moreover, due to the long distances traveled by the guided light waves, optical gain and loss processes in materials are often investigated in waveguide structures.¹⁵⁷

2.4 Light-emitting transistors

The key advantages of semiconducting SWNTs over other, perhaps more efficient, organic emitter materials are their NIR light emission close to the telecommunication wavelengths¹⁴ paired with high charge carrier mobilities for both electrons and holes.⁵ Being ambipolar semiconductors, SWNTs are perfectly suited for electrically-driven exciton generation and thus electroluminescence (EL) as realized in light-emitting field-effect transistors (LEFETs).^{158,159}

Figure 2.13a outlines the structure of a bottom-contact/top-gate LEFET, in which the semiconductor is contacted by two electrodes (serving as source and drain) and separated from the gate electrode by a thin dielectric layer. Upon application of a gate voltage V_G with respect to the grounded source electrode, charges are accumulated at the semiconductor-dielectric interface. Once a lateral electric field is provided by means of a source-drain bias V_D , charge carriers can flow through the created channel. As the accumulated charge density and hence conductivity depend on the gate voltage, the gate electrode controls the source-drain current I_D through the device.¹⁵⁸ An important parameter for semiconductor devices is the linear charge carrier mobility μ_{lin} , which can be extracted from the linear regime of a transfer curve (*i.e.*, at low V_D) according to¹⁶⁰

$$\mu_{lin} = \frac{L}{WCV_D} \frac{\partial I_D}{\partial V_G} \quad (2.11)$$

where L and W are the channel length and width, respectively, and C denotes the areal dielectric capacitance.

In order to generate EL, injected electrons and holes must recombine in the semiconductor. This requires precise tuning of the charge density profile along the channel by choice of suitable V_G and V_D . As illustrated in Figure 2.13b, if the applied gate voltage V_G is positive but smaller than the drain voltage V_D , the effective gate voltage relative to the drain ($V_G - V_D$) becomes negative. Under these conditions, electrons are injected from the source, whereas holes are injected from the drain electrode. Likewise, negative V_G and V_D give rise to hole injection from the source and electron injection from the drain. Consequently, the locally induced charge density must change sign at a certain position along the channel.¹⁶² This narrow region (typically 1 μm width¹⁶³) where the

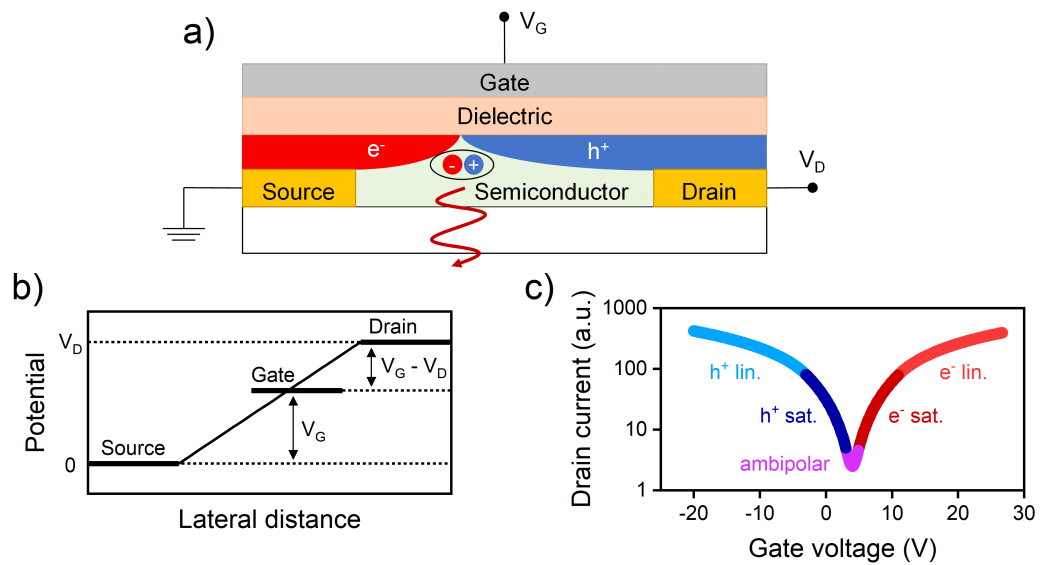


Figure 2.13: (a) Schematic of a light-emitting field-effect transistor, electrical exciton generation and light out-coupling through a transparent substrate. (b) Illustration of source, drain and gate electrode potentials and definition of effective bias between drain and gate. (c) Transfer characteristic calculated within a simplified model¹⁶¹ under the assumption of $V_D = 8$ V and equal mobilities ($\mu_h = \mu_e$) and threshold voltages ($V_{th}^e = -V_{th}^h = 3$ V) for electrons and holes. The linear (lin.), saturation (sat.) and ambipolar regime of electron and hole transport are color coded.

charge density is formally zero defines the recombination zone from which EL may be emitted. Since the width of the recombination zone is substantially smaller than typical channel lengths of an LEFET (several μm), it can be assumed that all injected electrons and holes recombine and thus their numbers are balanced and represented by the drain current.¹⁵⁹ In other words, both the hole and the electron channel are in the saturation regime with their pinch-off point located in the recombination zone. This ambipolar regime of transistor operation is characterized by a V-shaped transfer characteristic (*i.e.*, dependence of I_D on V_G at constant V_D) as depicted in Figure 2.13c. LEFETs were demonstrated for a broad range of luminescent semiconductors¹⁵⁹ from conjugated polymers¹⁶⁴ to transition metal dichalcogenides,¹⁶⁵ colloidal quantum dots¹⁶⁶ and carbon nanotubes.¹⁶⁷ Although LEFETs cannot compete with state-of-the-art light-emitting diodes (LEDs) when it comes to pure lighting applications, they offer various unique functionalities.¹⁵⁹ For instance, the combination of current switching and light emission in a single device or the ability to incorporate plasmonic nanostructures¹⁶⁸ thanks to the lateral design. Finally, LEFETs are a useful tool to

investigate charge transport in operating devices as they provide both electrical and optical information on the state of the semiconductor.¹⁵⁹

Chapter 3

Experimental Methods

This Chapter details the materials, the experimental methods and the characterization techniques used in this thesis.

3.1 (6,5) SWNT dispersion

Selective (6,5) SWNT dispersion. Nearly monochiral dispersions of (6,5) SWNTs were produced by shear force mixing in combination with selective polymer-wrapping.²⁰ CoMoCAT raw material (Chasm Advanced Materials, Batches SG65i-L58 or SG65i-L63, 0.38 g L⁻¹) was added to a solution of poly[(9,9-dioctylfluorenyl-2,7-diyl)-*alt*-(6,6')-(2,2')-bipyridine)] (PFO-BPy, American Dye Source, $M_w = 40 \text{ kg mol}^{-1}$, 0.5 g L⁻¹) in toluene and subjected to shear force mixing (Silversion L2/Air, 10 230 rpm) for typically 72-96 h. Aggregates and impurities were removed by two consecutive centrifugation steps (Beckman Coulter Avanti J26XP centrifuge) at 60 000 rpm for 45 min. The supernatant was extracted and passed through a poly(tetrafluoroethylene) (PTFE) syringe filter with 5 μm pore size to obtain individualized, PFO-BPy-wrapped (6,5) SWNTs.

Sonication-induced tube shortening. To investigate tube length-dependent effects, dispersions prepared according to the above protocol were subsequently tip-sonicated (Sonics Vibracell VXC-500) using a tapered microtip at 35 % amplitude with 8 s *on* and 2 s *off* pulses. The sample was immersed in a 5 °C cooling bath and the sonication time was varied between 4.5-23 h to control the degree of tube shortening. After sonication, the dispersion was centrifuged at 60 000 rpm for 45 min and the supernatant collected.

Removal of excess polymer by filtration. Depending on the experiment or subsequent processing it was sometimes necessary to reduce the concentration of unbound polymer in the dispersion. To this end, the as-prepared dispersion was passed through a PTFE membrane filter (Merck Millipore, JVWP, 25 mm diameter, 0.1 μm pore size) on a vacuum filtration setup. The filter pore size was chosen so as to collect the PFO-BPy-wrapped (6,5) SWNTs in high yield, but to allow passage of most of the unbound polymer chains in the sample. Relatively large quantities of (6,5) SWNTs ($\sim 100 \mu\text{g}$) can be collected on a single membrane and stored in air for several days without noticeable changes in material properties. For further processing and analysis, the SWNTs were re-dispersed by immersing the SWNT-coated membrane in a small volume of the desired pure solvent (usually toluene) or dilute polymer solution and applying bath sonication for typically 30 min.

3.2 Aryl-functionalization of polymer-wrapped SWNTs

Luminescent aryl sp^3 defects were introduced to PFO-BPy-wrapped (6,5) SWNTs through diazonium chemistry in organic media. As discussed in Section 4.2, it is crucial to match the reaction conditions to the solubility characteristics of the diazonium salt and the colloidal stability of the polymer-wrapped SWNTs. To account for the vastly different solubilities of the commercial diazonium salts (OMe-Dz, Cl₂-Dz, Br-Dz, NO₂-Dz) compared to the PTM-Dz and PTMH-Dz (see below for the structures), two different protocols were developed.

3.2.1 Reaction with commercial diazonium salts

Reagents. The following chemicals were purchased from Sigma Aldrich and used without further purification: 4-methoxybenzenediazonium tetrafluoroborate (OMe-Dz, 98%), 3,5-dichlorophenyldiazonium tetrafluoroborate (Cl₂-Dz), 4-bromobenzenediazonium tetrafluoroborate (Br-Dz, 96%) and 4-nitrobenzenediazonium tetrafluoroborate (NO₂-Dz, 97%), potassium acetate (KOAc, 98%) and 18-crown-6 (18C6, 99%). The molecular structures of these compounds are displayed in Figure 3.1. OMe-Dz and Cl₂-Dz were stored under N₂ atmosphere at -20 °C. Br-Dz and NO₂-Dz were stored in air at 5 °C. All diazonium salts were stored in darkness. KOAc and 18C6 were stored in air at room temperature.



Figure 3.1: Molecular structures of commercial diazonium salts and additives.

Remarks on starting dispersion. The starting material for this functionalization protocol¹⁶⁹ are as-prepared (6,5) SWNT dispersions without prior removal of excess polymer (Section 3.1). The concentration of (6,5) SWNTs in the reaction mixture was 0.36 mg L⁻¹ (corresponding to an optical density (OD) of 0.2 cm⁻¹ at the E_{11} transition) unless stated otherwise.

Reaction protocol. First, a solution of 18C6 in toluene was added to the (6,5) SWNT dispersion such that the final 18C6 concentration becomes 7.6 mmol L^{-1} after addition of the remaining components. Second, a solution of the aryldiazonium salt in acetonitrile (MeCN) was added in order to produce an 80:20 vol-% toluene/acetonitrile mixture with the desired diazonium concentration, which was typically in the range of $\mu\text{mol L}^{-1}$ to mmol L^{-1} . At this stage two different routes were explored.

Either a low concentration of KOAc was introduced (**Route I**) or not (**Route II**). For **Route I**, a stock solution of KOAc ($10^{-4} \text{ mol L}^{-1}$) in 80:20 vol-% toluene/MeCN including 7.6 mmol L^{-1} 18C6 was prepared. 5 min after addition of the diazonium salt, an appropriate volume of this solution was added to the reaction mixture to produce a low KOAc concentration of typically $10^{-9} \text{ mol L}^{-1}$. For **Route II**, this step was simply omitted.

After addition of all reagents, the mixture was protected from light and stored at room temperature without stirring. Reactions were terminated after 16 h by vacuum filtration of the mixture through a PTFE membrane filter (Merck Millipore, JVWP, 25 mm diameter, $0.1 \mu\text{m}$ pore size) to collect the functionalized SWNTs. While still on the filtration setup, the filter cake of SWNTs was washed with MeCN (10 mL) and toluene (5 mL) to remove unreacted diazonium salt and by-products. Finally, the functionalized (6,5) SWNTs were re-dispersed in toluene by bath sonication for 30 min.

3.2.2 Reaction with PTM and PTMH diazonium salts

Reagents and solvents. PTM-Dz and PTMH-Dz (for structures see Figure 3.2) were synthesized by J. Alejandro de Sousa and Aleix Quintana García under the supervision of Núria Crivillers at the Institut de Ciència de Materials de Barcelona following the synthetic route reported by Seber *et al.*¹⁷⁰ Both diazonium salts were stored in the dark in air at $5 \text{ }^\circ\text{C}$. Tetrahydrofuran (THF), which was used in the functionalization reaction, was freshly distilled over sodium to remove water and peroxide contaminations.

Light sensitivity. Since the PTM radical is sensitive to UV and blue light, all steps involving PTM-Dz were performed in a laboratory equipped with red lights. When using PTMH-Dz, work was carried out under white light, but care was taken to limit light exposure to 1-2 min due to the general light sensitivity of diazonium compounds.

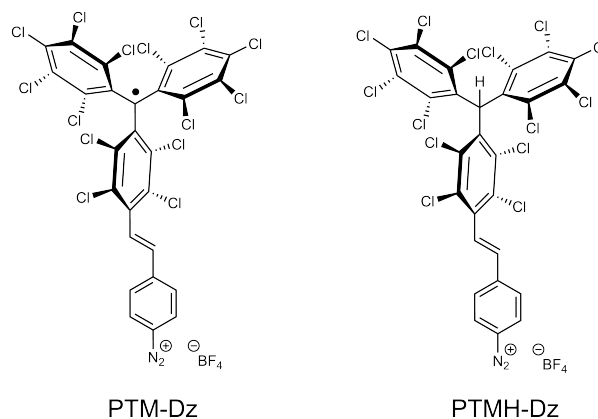


Figure 3.2: Molecular structures of PTM-Dz and PTMH-Dz.

With the exception of short-term (1-2 min) transfer of samples under white light, PTM-functionalized SWNTs were always protected from UV and blue light.

Remarks on solubility. Due to the good solubility of PTM-Dz and PTMH-Dz in THF and colloidal stability of PFO-BPy-wrapped (6,5) SWNTs in this solvent, the reaction was performed in THF without addition of other solubilizing agents.

Transfer of (6,5) SWNTs to THF. The as-prepared (6,5) SWNT dispersion in toluene was filtered through a PTFE membrane (Merck Millipore, JVWP, 25 mm diameter, 0.1 μm pore size) to collect the SWNTs. Then, the SWNTs were re-dispersed in a small volume of THF by bath sonication for 30 min.

Reaction protocol. The (6,5) SWNT dispersion in THF was combined with a solution of either PTM-Dz or PTMH-Dz in THF to reach a (6,5) SWNT concentration of 0.72 mg L^{-1} (corresponding to an OD of 0.4 cm^{-1} at the E_{11} transition) and a diazonium salt concentration of either 7 $\mu\text{mol L}^{-1}$ or 0.15 mmol L^{-1} for low and high levels of functionalization, respectively. The reaction mixture was protected from light and stored at room temperature without stirring. Reactions were terminated after 16 h by vacuum filtration of the mixture through a PTFE membrane (Merck Millipore, JVWP, 25 mm diameter, 0.1 μm pore size) to collect the functionalized SWNTs. While still on the filtration setup, the filter cake of SWNTs was washed with THF ($3 \times 7 \text{ mL}$) to remove unreacted diazonium salt and by-products. Finally, the functionalized (6,5) SWNTs were re-dispersed in toluene by bath sonication for 30 min.

3.3 Film deposition and device fabrication

Prior to the first layer deposition, all substrates were cleaned by two bath sonication steps in acetone and isopropyl alcohol (IPA) for 10 min each.

3.3.1 Films for single-tube microscopy

Glass slides (Schott AF32eco) were coated with 150 nm of gold (thermal evaporation) to suppress photoluminescence from the glass. A small volume of a dispersion of PFO-BPy-wrapped (6,5) SWNTs was added to a concentrated solution of polystyrene (PS, $M_w = 182 \text{ kg mol}^{-1}$, Polymer Source, Inc.) in toluene to adjust the (6,5) SWNT concentration to an OD of 0.005 cm^{-1} at the E_{11} transition and the PS concentration to 20 g L^{-1} . This dispersion was spin-coated at 2000 rpm onto the prepared substrates to create a low density of SWNTs embedded in a PS matrix.

3.3.2 Aerosol-jet printing

An Aerosol Jet 200 printer (Optomec, Inc.) equipped with an ultrasonic atomizer and a $200 \mu\text{m}$ inner diameter nozzle was used for aerosol-jet printing¹⁷¹ of pristine and functionalized (6,5) SWNTs onto glass substrates. The ink consisted of a dispersion of PFO-BPy-wrapped (6,5) SWNTs at a concentration of 5.4 mg L^{-1} (equivalent to an OD of 3 cm^{-1} at the E_{11} transition) and 2 vol-% of terpineol (mixture of isomers, Sigma Aldrich). The flow of sheath and carrier gas was 30 sccm and 25 sccm, respectively, and the sample stage was heated to $100 \text{ }^\circ\text{C}$ to enable fast evaporation of toluene. The SWNT layer thickness was tuned by the process speed and number of printing cycles. Residual terpineol was rinsed off with THF and IPA and the sample was blow-dried.

3.3.3 Waveguide fabrication

Single-side polished, circular magnesium fluoride (MgF_2) substrates with 25 mm diameter and 1 mm thickness were purchased from VM-TIM (Jena, Germany). The optical axis was orthogonal to the polished surface. Filter cakes of sp^3 functionalized (6,5) SWNTs were re-dispersed in a small volume of toluene by bath sonication for a few hours to produce a highly concentrated SWNT stock dispersion, which was

subsequently combined with a solution of PS (35 g L^{-1} , $M_w = 182 \text{ kg mol}^{-1}$, Polymer Source, Inc.) in toluene in a volume ratio of 1:5 (SWNT dispersion/PS solution). The viscous dispersion was spin-coated onto MgF_2 substrates at 800 rpm for 2 min. The substrates were scratched on the opposite side with a diamond scribe to facilitate breaking. The coated substrates were immersed in liquid nitrogen for several seconds to freeze the polymer matrix before cleaving the substrate to produce a clean edge for characterization.

3.3.4 LEFET fabrication

Interdigitated bottom-contacts ($20 \mu\text{m}$ channel length, 10 mm channel width) were patterned onto glass substrates (Schott AF32eco) by standard photolithography and electron-beam evaporation of 2 nm of chromium and 30 nm of gold, followed by lift-off in *N*-methyl-2-pyrrolidone. Random networks of pristine or functionalized (6,5) SWNTs were created by spin-coating a concentrated dispersion (18 mg L^{-1} corresponding to an E_{11} OD of 10 cm^{-1}) at 2000 rpm. Each substrate was coated three times with a 2 min annealing step between depositions. After the third deposition, the substrates were thoroughly rinsed with THF and IPA and blow-dried. Subsequently, the nanotube films were patterned by standard photolithography combined with oxygen plasma etching. The samples were then transferred to a nitrogen-filled glovebox and annealed at $150 \text{ }^\circ\text{C}$ for 30 min. A hybrid dielectric of 11 nm syndiotactic poly(methyl methacrylate) (PMMA, $M_w = 350 \text{ kg mol}^{-1}$, Polymer Source, Inc.) and 61 nm hafnium oxide (HfO_x) was used in all transistors. First, a solution of PMMA (6 g L^{-1}) in *n*-butyl acetate was spin-coated at 4000 rpm. Second, atomic layer deposition (Ultratech Savannah S100) using a tetrakis(dimethylamino) hafnium precursor produced a HfO_x layer that also served as a natural encapsulation of the device. The devices were completed by thermal evaporation of silver top-gate electrodes of 30 nm thickness through a shadow mask.

filter settings for PLE mapping. Scattered laser light and luminescence from the sample were separated by a dichroic long-pass filter (**DMLP**).

The sample could be either a solid thin film or a liquid dispersion. In case of thin films, focusing was performed by imaging the residual laser back-reflection that was not suppressed by the **DMLP** onto an alignment camera (**Si cam**, Pixelink) *via* a flip-mirror (**FM**) and a tube lens (**TL1**). The objective was moved along the optical axis until a sharp focus point was obtained. In case of liquid samples, a small volume of dispersion was filled into a quartz cuvette (Hellma Analytics, QX material) that was sealed with a PTFE stopper. One of the clear faces of the cuvette was approached with the objective until the PL signal intensity reached its maximum value.

For acquisition of PL spectra, residual laser light was blocked by a long-pass filter (**LP**, 830 nm cut-on, unless noted otherwise) and focused onto the entrance slit (300 μm width) of a grating spectrograph (**GSG**, Acton SpectraPro SP2358) by a tube lens (**TL2**). The turret in the spectrograph was equipped with a mirror (**MG**) and two different gratings (**G1** and **G2**). The luminescence from the sample was dispersed by a grating with 150 grooves mm^{-1} and 1200 nm blaze and detected by a liquid nitrogen-cooled InGaAs line camera (**NIR LC**, Princeton Instruments OMA V:1024-1.7 LN). For TCSPC, the output of the spectrograph was guided to a gated InGaAs/InP avalanche photodiode (**NIR APD**, Micro Photon Devices) *via* a collimation lens (**CL**) and an NIR-optimized 20 \times objective (**OBJ2**, Mitutoyo). The spectrometer was controlled either by the commercial WinSpec 32 software or a customized LabVIEW script.

Spectral correction. All spectra were corrected for thermal noise of the detector by subtracting a background spectrum acquired under dark conditions. Further, the influence of the wavelength-dependent photon detection efficiency of the InGaAs detector and light absorption due to optical components was determined by transmitting a broadband light source (Thorlabs SLS201/M, 300-2600 nm) of known spectral power distribution ($I_{theo,lamp}(\lambda)$) through the detection path and collecting a spectrum ($I_{exp,lamp}(\lambda)$). A transfer function $f(\lambda) = I_{exp,lamp}(\lambda) / I_{theo,lamp}(\lambda)$ was computed and the sample spectra corrected according to $I_{corr}(\lambda) = I_{raw}(\lambda) / f(\lambda)$.

EL spectroscopy. EL was generated by applying suitable constant voltages to the drain (V_D) and gate (V_G) terminals of an LEFET with respect to the grounded source terminal using a Keithley 2612A source meter. The transistor was mounted on the optical setup

with the direction of current flow orthogonal to the optical axis of the detection path. To ensure that the emission zone was located in the center of the channel, the transistor structure was illuminated from the top by the collimated beam of a lamp to image regions of high (channel) and near-zero (electrodes) transmission onto the InGaAs line camera *via* the spectrograph mirror. In this mode, the center of the channel was shifted to the center of the detector array and aligned with the input slit of the spectrometer. After switching off the lamp, V_D and V_G were adjusted such that the EL signal was positioned in the center of the detector array before exchanging the mirror for the grating to record a spectrum.

3.4.2 Time-correlated single-photon counting

The time-resolved PL decay was monitored in the configuration described under Section 3.4.1 using the pulsed output of a supercontinuum laser as the excitation source. The laser further provided electrical trigger signals to a gated InGaAs/InP avalanche photodiode (APD) and a counting module (PicoQuant PicoHarp 300). Histograms of photon arrival times were produced using the counting module and reconvolution-fitted with the aid of SymphoTime64 software. The fast, instrument-limited decay of the E_{11} PL signal served as the instrument response function (IRF), which had a full width at half maximum (FWHM) of 84 ps. Care was taken to record the IRF with the same laser wavelength setting as employed in the experiment to account for the wavelength-dependent pulse width of the supercontinuum laser.

3.4.3 Cryogenic magneto-optical setup

Low-temperature PL spectroscopy under high magnetic fields was performed by Shen Zhao under the supervision of Alexander Högele at the Faculty of Physics of the Ludwig-Maximilians-Universität München. A closed-cycle magneto-optical cryostat (attoDRY1000, attocube systems) was employed to maintain a temperature of 4 K during the experiment. The sample was mounted on a custom-built holder such that the magnetic field was parallel and light propagation orthogonal to the sample surface, *i.e.* Voigt geometry. The cw output of a Ti:sapphire laser was tuned to 995 nm to be in resonance with the E_{11} transition of (6,5) SWNTs. The cw laser power was kept at 6 μ W

to avoid multi-exciton effects and improve emission stability. PL from single nanotubes was collected by an aspheric lens (Thorlabs 354330-B, N.A. 0.68), dispersed by a spectrograph (Acton SpectraPro SP2500 equipped with a 300 grooves mm^{-1} grating) and detected by a liquid nitrogen-cooled InGaAs line camera (Princeton Instruments OMA V:1024-1.7 LN). For low-temperature TCSPC measurements, the sample was excited in pulsed mode (2×10^{14} photons cm^{-2} pulse $^{-1}$) and the PL directed toward a superconducting single-photon detector (Scontel TCOPRS-CCR-SW-85). The IRF was recorded on the attenuated laser signal.

3.4.4 PLQY determination

The PL quantum yield (PLQY) of pristine and functionalized SWNTs in liquid dispersions or thin films was determined from integrating sphere (IS) measurements giving direct access to the number ratio of emitted (N_{PL}) to absorbed (N_{abs}) photons:^{20,172}

$$\text{PLQY} = \frac{N_{PL}}{N_{abs}} \quad (3.1)$$

For this purpose, a set of measurements was performed on the sample and a reference. In case of film samples, the empty sphere served as the reference, whereas a quartz cuvette (Hellma Analytics, QX material) filled with the respective solvent was used as the reference for dispersions.

The spectrally-filtered output of a supercontinuum laser (~ 10 ps pulse width, 20 MHz repetition rate, ~ 300 μW average output power) was tuned to the E_{22} transition of (6,5) SWNTs at 575 nm and the collimated beam directed into the IS. Both film and dispersion samples were directly illuminated by the laser. The OD at the E_{11} transition was adjusted to 0.2 cm^{-1} or less such that re-absorption was negligible.¹⁷³ Light was out-coupled from the IS through an optical fiber and guided to an InGaAs line camera detector (Section 3.4.1). Spectra were recorded either in the NIR (900-1600 nm) to detect the PL or around the laser wavelength (575 nm) to determine the sample absorption from the difference between the sample and the reference spectrum.

N_{PL} is determined by integration of the sample emission spectrum, while N_{abs} is obtained as the difference of the integrated laser signals of the reference and sample spectra. Note that if spectra are integrated on a wavelength scale, the recorded intensity

must be transformed to $I(\lambda) \times \lambda$ for the integral to be proportional to the number of photons.

It is crucial to account for the wavelength-dependent detection efficiency and absorption due to optical components in the visible and NIR range as described in Section 3.4.1. Moreover, the absorption of the commonly employed solvent toluene strongly overlaps with the E_{11}^* emission of sp^3 defects. Therefore, the emission spectra of toluene dispersions were corrected by placing a toluene-filled cuvette inside the IS while collecting the calibration lamp spectrum (Thorlabs SLS201/M) in the NIR range.¹⁶⁹

3.4.5 Waveguide characterization

Waveguides prepared according to Section 3.3.3 were characterized in a home-built setup designed to enable optical gain measurements employing the variable stripe length method.^{157,174} For this purpose, a laser line (of variable length) was projected onto the sample and the waveguided emission was collected under a right angle from the edge of the substrate as shown in Figure 3.4.

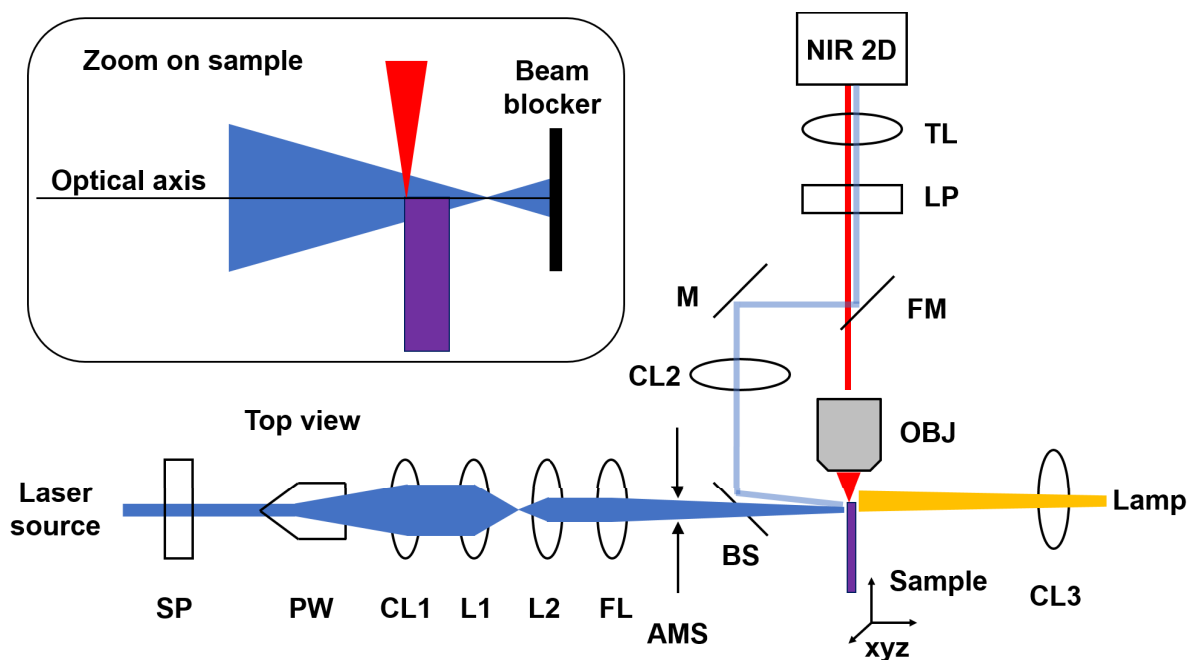


Figure 3.4: Setup for variable stripe length waveguide characterization. Blue color indicates excitation laser light, red color emitted PL and yellow color lamp radiation used for alignment purposes. The laser beam shaping is shown schematically in top view.

Samples were excited by the femtosecond-pulsed output of a Ti:sapphire **laser** (Coherent Astrella, 4 kHz repetition rate, 78 fs pulse duration, centered at 800 nm) that was tuned to the desired pump wavelength using an optical parametric amplifier (Light Conversion TOPAS-Prime). After rejecting unwanted NIR laser light with a short-pass filter (**SP**), the laser beam entered a Powell lens (**PW**, Edmund Optics, N-BK7, 30° fan angle) that generated a narrow laser line, which was collimated by another lens (**CL1**). A telescope (composed of lenses **L1** and **L2**) was used to demagnify the stripe and another lens (**FL**) focused the laser line onto the **sample**, which was mounted on **xyz** micropositioners. The length of the excited stripe was adjusted by restricting the beam with a mechanical slit (**AMS**).

Prior to measurement, the position of the substrate edge was determined by imaging the sample under back-illumination with the collimated (**CL3**) output of a lamp. Furthermore, upon inserting a flip-mirror (**FM**), the stripe length on the sample surface could be measured by imaging the laser back-reflection onto the detector with an NIR beamsplitter (**BS**) and two lenses (**CL2** and **TL**).

After the described alignment and beam shaping, the waveguided emission was collected from the substrate edge through an NIR-optimized objective (**OBJ**, 20×, N.A. 0.45, Olympus). Appropriate long-pass filters were included to block scattered laser light and the PL was dispersed in an imaging spectrograph (Princeton Instruments IsoPlane SCT 320) and detected by a thermoelectrically-cooled 2D InGaAs array (**NIR 2D**, Princeton Instruments NIRvana:640ST). Note that this detector was used for both spectral acquisition and imaging.

3.5 Other characterization techniques

Electron paramagnetic resonance spectroscopy. Electron paramagnetic resonance (EPR) measurements were performed by Vega Lloveras at the Institut de Ciència de Materials de Barcelona. EPR spectra in the X band (9.5 GHz) were acquired on a Bruker ESP 300 E spectrometer equipped with a T102 rectangular cavity. Unless stated otherwise, measurements were performed at room temperature.

Absorption spectroscopy. Absorption spectra were acquired with a Varian Cary 6000i UV-vis-NIR spectrophotometer. Liquid samples were filled into a quartz cuvette

(Hellma Analytics, QX or QS material) with 1 cm path length. A baseline correction was applied by measuring a spectrum of the cuvette filled with the respective solvent.

Raman spectroscopy. Raman spectra were recorded with a Renishaw inVia Reflex confocal Raman microscope equipped with a 50 \times long-working distance objective (Olympus, N.A. 0.5). The wavelength of the incident laser was 532 nm. Samples were prepared by drop-casting a small volume of SWNT dispersion onto glass slides (Schott AF32eco) and rinsing off excess polymer with THF and IPA. The resulting films were scanned with a line laser and the average of > 1000 spectra collected from different positions was computed.

Atomic force microscopy. Atomic force micrographs were recorded with a Bruker Dimension Icon atomic force microscope in tapping mode under ambient conditions. For nanotube length measurements, SWNT dispersions with an E_{11} OD of ~ 0.2 cm were spin-coated at 2000 rpm onto native silicon wafers and excess polymer was rinsed off with THF and IPA. Data was visualized and analyzed using the Gwyddion software.

Electrical characterization. Current-voltage characteristics of field-effect transistors were measured with an Agilent 4156C Semiconductor Parameter Analyzer under dry nitrogen atmosphere. Capacitance measurements were performed with a Solartron Analytical ModuLab XM MTS impedance analyzer. The device capacitance was estimated as the maximum on-state capacitance in a quasi-static measurement at 100 Hz.

Chapter 4

sp^3 Functionalization of Polymer-Wrapped SWNTs

This Chapter describes a method to create luminescent defects in polymer-wrapped SWNTs and discusses the ensuing optical properties.

The results of this Chapter were published* in part in Berger *et al.*, *ACS Nano* **2019**, *13*, 9259-9269.¹⁶⁹ Modified reprints of previously published Figures are presented with permission of the American Chemical Society. Parts of the data shown in Section 4.3 and 4.4 were collected by Tim Nowack and Christine Müller under my supervision.

4.1 Introduction

As described in Section 2.2, luminescent sp^3 defects in semiconducting SWNTs offer a range of attractive optical properties, including enhanced PLQY¹⁰² and photon-antibunching at room temperature.¹⁴ For several years, however, emissive defects were only accessible through ozonation,^{10,115,121,125} diazonium chemistry^{102,127,139,175} or Billups-Birch reduction.^{176,177} While the latter method involves extremely harsh reaction conditions, thus precluding sensitive functional groups, the other routes were restricted to aqueous dispersions of SWNTs, which come with several drawbacks.

Firstly, the vast majority of dispersion protocols utilizing aqueous surfactant solutions make use of high-power sonication that damages the nanotube structure and leads to short tube length with high exciton quenching site densities.^{20,34,101} Secondly, the high concentrations of surfactant^{37,178} or other additives³⁹ employed in the process impair film formation and limit the processability of such nanotube inks. Finally, residual metallic SWNTs hinder the fabrication of optoelectronic devices due to short-circuiting at short channel lengths.^{45,50}

Polymer-sorted SWNTs, on the other hand, feature excellent semiconducting purity^{45,50} (see Section 2.1.2) and are easily processed into high-quality thin films^{171,179} (compare Chapter 6). Furthermore, mild exfoliation methods, such as shear force mixing, may be used to disperse long nanotubes ($> 1 \mu\text{m}$) with comparatively high PLQY ($\sim 2.5\%$) thanks to the low quenching site density and the nonpolar environment provided by the organic solvent (*e.g.* toluene).²⁰

The sp^3 functionalization of polymer-wrapped nanotubes with pre-formed diazonium salts is challenging though, because the polymer coating imparts colloidal stability only in low-polarity solvents, which do not solubilize polar reagents like diazonium salts. To

*URL: <https://pubs.acs.org/doi/10.1021/acsnano.9b03792>. Requests related to the reuse of this material should be directed to the American Chemical Society.

overcome this conflict, diazonium salts may be generated *in situ* from aromatic amines, but high temperature and inert conditions hamper the scalability of this approach.¹⁸⁰ Dip-doping of pre-deposited polymer-wrapped SWNTs in aqueous reagent solutions was demonstrated as well, but only successful with sparsely distributed nanotubes and highly reactive diazonium salts.¹²⁸ Hence, none of these protocols is well suited for the scalable manufacture of optoelectronic devices harnessing the optical properties of sp^3 defects.

In this Chapter, a method is described that fills this gap and enables the simple and scalable functionalization of polymer-wrapped SWNTs with commercial diazonium salts at room temperature.

4.2 Functionalization method

The starting material for functionalization were PFO-BPy-wrapped (6,5) SWNTs dispersed by shear force mixing in toluene (Section 3.1).²⁰ To enable the reaction between these nanotubes and pre-formed, commercially available aryldiazonium salts, the reaction medium must solubilize the diazonium salt without destabilizing the colloidal dispersion too strongly. In the method described here, such a compromise is achieved by adding the ether crown 18-crown-6 (18C6, see Figure 4.1 for molecular structure) to enhance the solubility of the diazonium salt in organic solvents. 18C6 was chosen as the solubilizing agent, because Beadle *et al.* had previously identified 18C6 as a suitable phase-transfer catalyst for reactions with aryldiazonium salts in aromatic solvents.¹⁸¹ Since the presence of 18C6 in toluene alone did not enable sufficiently high diazonium concentrations, acetonitrile (MeCN) was added as a polar co-solvent. A 80:20 vol-% toluene/acetonitrile mixture with 7.6 mmol L^{-1} 18C6 increased the solubility of aryldiazonium salts to the level of a few mmol L^{-1} . In this medium, PFO-BPy-wrapped SWNTs showed only minor and reversible flocculation over the course of hours that did not inhibit the formation of sp^3 defects (Figure 4.1).

As functionalization is thought to proceed *via* aryl radical addition to the conjugated SWNT lattice,¹³⁷ the question arises how aryl radicals may be generated from diazonium salts in organic media. It is worth noting that diazonium functionalization is generally a complex process that starts by adsorption of the diazonium salt to the

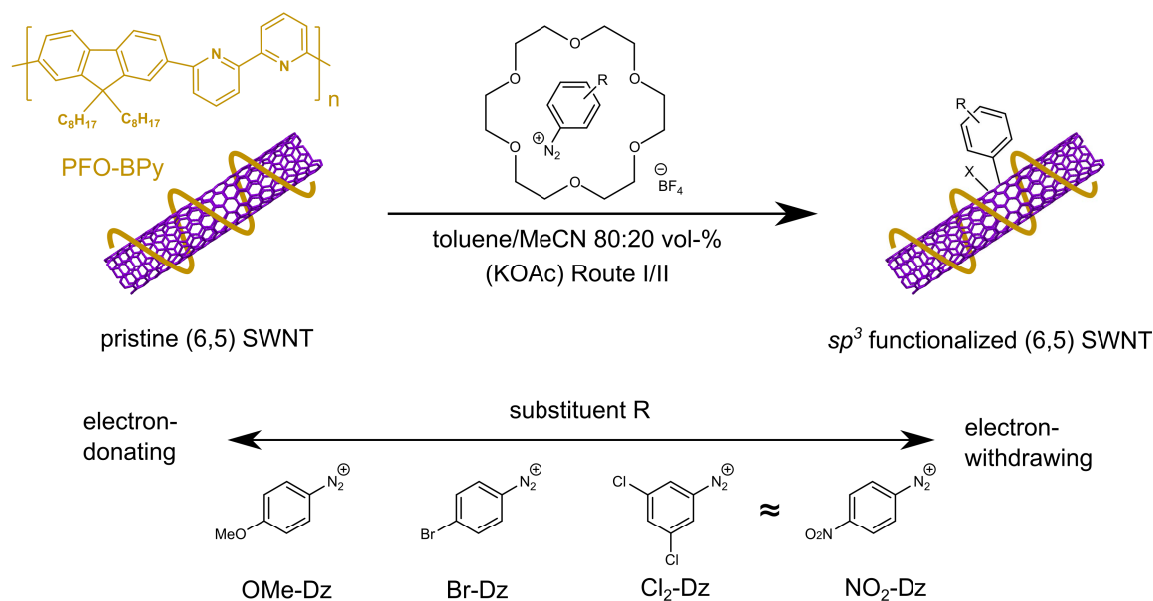


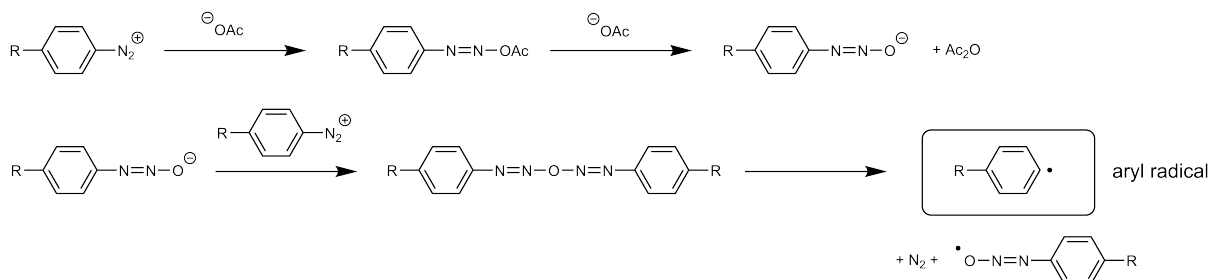
Figure 4.1: Aryl sp^3 defect creation in PFO-BPy-wrapped (6,5) SWNTs through reaction with diazonium salts. X denotes an auxiliary fragment of unknown molecular structure. The method is applicable to aryl diazonium salts with substituents R ranging from electron-withdrawing to electron-donating character.

nanotube sidewall (on the timescale of a few minutes in water) and may involve various charged and radical intermediates depending on the reaction conditions.^{136,137,182} In water, radical initiation is known to occur through a Gomberg-Bachmann (GB) reaction mediated by hydroxide ions.¹³⁸ For the reaction with nanotubes in aqueous dispersion, two initiation pathways have been proposed:^{137,182} Either GB reaction or a single-electron transfer from the SWNT to the diazonium salt followed by release of N_2 . Hence, two reaction conditions were tested in this work. In Route I (see Section 3.2.1), potassium acetate (KOAc) was added, following a report that carboxylate salts can mimic the role of hydroxide as a GB initiator in organic solvents when solubilized by 18C6.¹⁸¹ For Route II, KOAc was omitted, which left a single-electron transfer from the nanotube to the diazonium compound as a likely activation pathway. Possible radical initiation mechanisms relevant to Route I and Route II protocols are depicted in Figure 4.2a with reaction schemes (i) and (ii), as proposed by Beadle *et al.*¹⁸¹ and Dyke *et al.*¹⁸² The follow-up step of aryl radical addition to the nanotube lattice is illustrated in Figure 4.2b. As will be discussed in relation to Figure 4.4 below, the defect densities obtained from both routes are similar (for a given diazonium concentration). Hence,

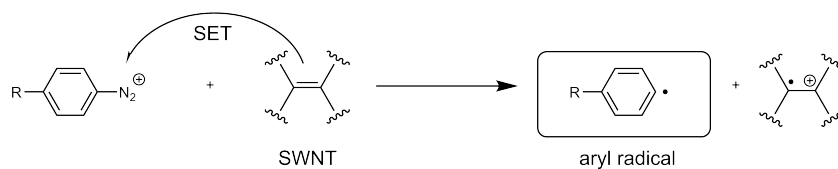
the single-electron transfer mechanism appears to be the main initiation pathway in organic solvents as it can occur under both Route I and Route II conditions.

a) Radical initiation

i) Gomberg-Bachmann mechanism with KOAc (Beadle *et al.*)



ii) Single-electron transfer from nanotube to diazonium salt (Dyke *et al.*)



b) Radical addition

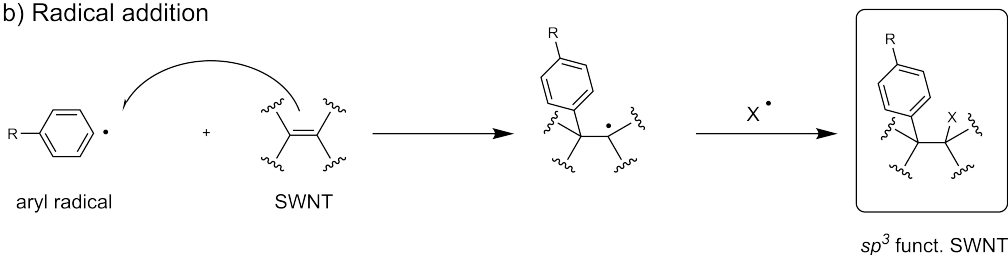


Figure 4.2: Proposed mechanisms for (a) aryl radical generation from diazonium salts and (b) sp^3 defect formation by radical addition to the nanotube lattice. Radical initiation may be promoted by (i) potassium acetate in a Gomberg-Bachmann reaction or (ii) a single-electron transfer from the nanotube to the diazonium compound, as proposed by Beadle *et al.*¹⁸¹ and Dyke *et al.*¹⁸²

A detailed functionalization protocol using commercial diazonium salts with and without KOAc can be found in Section 3.2.1 of the Experimental methods. After a typical reaction time of 16 h at room temperature, the sp^3 functionalized nanotubes were collected by vacuum filtration and thoroughly washed with acetonitrile and toluene to remove unreacted diazonium salt and by-products. During the reaction, the mixture showed only weak PL, but after the washing step the PL intensity increased dramatically. As the reaction between nanotubes and diazonium salts is rather inefficient,¹³⁶ a high concentration of diazonium cations must be adsorbed on the nanotube surface to drive the reaction at a reasonable rate. Presumably, the high concentra-

tion of charged adsorbates is responsible for PL quenching during the reaction, thus preventing the *in situ* monitoring of the reaction progress by PL spectroscopy. Once the functionalized SWNTs are washed, however, they are easily re-dispersed in pure solvents (here, toluene) or dilute polymer solutions to obtain samples with stable and bright PL, which will be analyzed in detail in the next Section.

4.3 Photoluminescence and absorption of sp^3 defects

Absorption and photoluminescence spectra (Figure 4.3a,b) recorded for dispersions of (6,5) SWNTs after functionalization with 4-bromobenzenediazonium tetrafluoroborate (Br-Dz) clearly indicate the formation of luminescent defects. In addition to intense E_{11} absorption at 994 nm from the intrinsic band-edge exciton, an absorption band at 1142 nm emerges for functionalized SWNTs (Figure 4.3a). Since the band is absent in the untreated reference sample and increases monotonically with diazonium concentration C_{Dz} , it is assigned to E_{11}^* absorption of the defect state. The identification of this band with sp^3 defects in previous reports was compromised by dilute dispersions and the presence of minority chiralities.¹⁰² Because of the high quality of the polymer-sorted SWNT dispersions and the concomitant low scattering background, the E_{11}^* band could be clearly resolved despite its low optical density of only a few percent relative to the E_{11} transition. As the density of sp^3 defects in the lattice is very low, their absorption is weak, but they nonetheless strongly modify the PL properties of the SWNT by virtue of efficient exciton trapping.¹⁰³

As evident from Figure 4.3b, sp^3 functionalized (6,5) SWNTs display two emission signals at 999 nm and 1161 nm originating from mobile (E_{11}) and defect-localized excitons (E_{11}^*), respectively. With increasing diazonium concentration and thus, defect density, the E_{11} PL intensity drops (not apparent in the normalized spectra) and the E_{11}^* emission becomes more and more dominant as diffusing E_{11} excitons are funneled into sp^3 defects. The evolution of PL intensity as a function of defect density will be discussed in detail within the framework of PLQY measurements (Section 4.4). Since the reaction cannot be monitored *in situ* and the work-up procedure changes the SWNT concentration, the recorded PL intensities cannot be compared directly among different

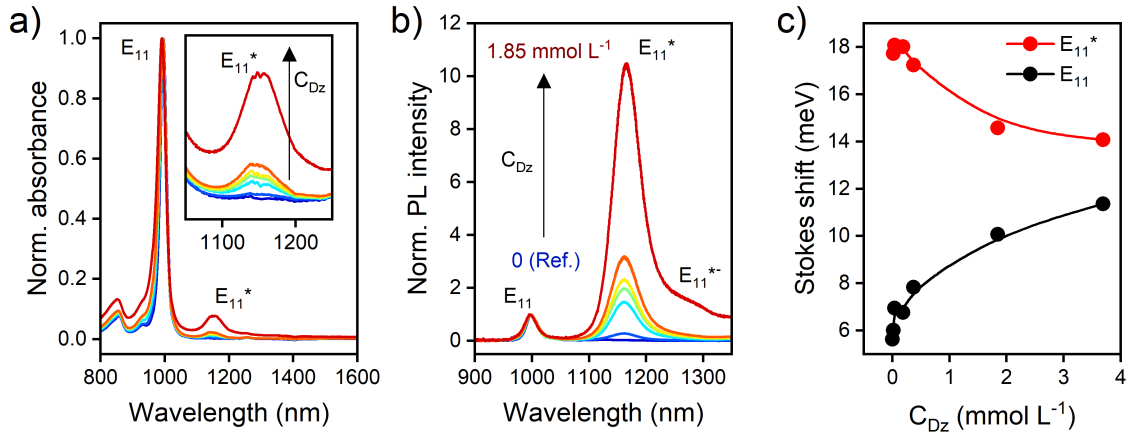


Figure 4.3: Normalized (a) absorption and (b) photoluminescence (PL) spectra of (6,5) SWNT dispersions after functionalization with different concentrations (C_{Dz}) of 4-bromobenzenediazonium tetrafluoroborate (Br-Dz). PL was excited at 575 nm (pulsed, 0.5 mJ cm^{-2}). (c) Extracted Stokes shifts of the E_{11} and E_{11}^* transition as a function of diazonium concentration and thus, defect density.

batches and thus, absolute PL quantum yields are required for a full interpretation of the PL data.

From the absorption and PL spectra, the Stokes shifts (Figure 4.3c) of the E_{11} and E_{11}^* transition are obtained. Interestingly, the Stokes shift of the E_{11}^* transition amounts to 18 meV in the low defect density limit, which is merely a factor of ~ 3 larger than that of the E_{11} transition. The small E_{11} Stokes shift is a result of the rigid SWNT structure and the delocalized character of the intrinsic E_{11} exciton.⁹⁷ For defect-localized excitons, on the other hand, substantial vibrational reorganization energies and hence, Stokes shifts, were predicted by theory.^{107,113} Specifically, an E_{11}^* Stokes shift of ~ 140 meV was computed for the *ortho*⁺⁺ binding configuration of 4-bromophenyl defects,¹⁰⁷ which is in stark contrast to the experimentally determined value of 18 meV. Moreover, the other aryl substituents studied in this work also led to E_{11}^* Stokes shifts of around 20 meV.

The Stokes shift and the degree of reorganization are intimately connected with the mismatch between the optical trap depth (defined as the PL energy difference $\Delta E_{opt} = E_{11} - E_{11}^*$) and the thermal energy required for exciton detrapping (ΔE_{therm}). Kim *et al.* attributed the difference between both quantities to a vibrational reorganization energy $\Delta E_{reorg} = \Delta E_{opt} - \Delta E_{therm}$ and extracted values in the range of 20-120 meV for ΔE_{reorg} depending on the defect density and the aryl substituent.¹¹³ However, within

the model employed by Kim *et al.*,¹¹³ the E_{11}^* Stokes shifts measured in this work should represent an upper limit to the magnitude of ΔE_{reorg} and thus call such large reorganization energies into question. Thus, it appears more likely that a significant deformation of the SWNT ground state structure at the defect site, as described in other reports^{10,102} and sketched in Figure 2.7, is responsible for the discrepancy between optical and thermal trap depth. In that case, the term $\Delta E_{opt} - \Delta E_{therm}$ and the E_{11}^* Stokes shift are decoupled and both experimental observations can be reconciled.

Upon closer inspection, the absorption and emission features (Figure 4.3a,b) of the E_{11} blue-shift, whereas the E_{11}^* signals red-shift with increasing defect density. As the shifts are stronger in absorption than in emission, the Stokes shifts become defect density-dependent. While the E_{11}^* Stokes shift is roughly constant below a diazonium concentration of $0.185 \text{ mmol L}^{-1}$, it drops at higher defect densities, potentially due to defect clustering accompanied by excitonic state delocalization.¹¹³ In contrast to that, the E_{11} Stokes shift is sensitive even to very low defect concentrations and approaches the E_{11}^* Stokes shift for highly defective SWNTs. This finding underscores the role of the E_{11} Stokes shift as a useful probe of low defect densities in SWNTs.²⁰

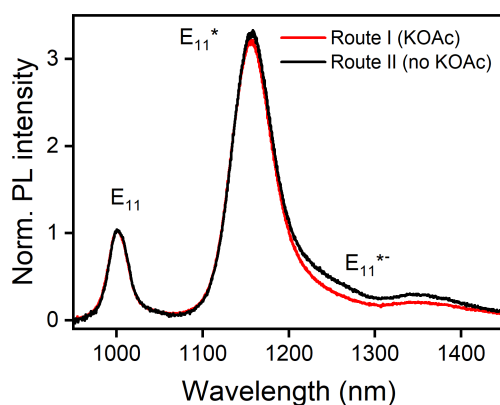


Figure 4.4: Normalized PL spectra of (6,5) SWNTs functionalized with 4-methoxybenzenediazonium tetrafluoroborate (OME-Dz) in the presence of $10^{-9} \text{ mol L}^{-1}$ KOAc (Route I) and in the absence of KOAc (Route II). Excitation conditions: 575 nm, pulsed, 0.5 mJ cm^{-2} .

PL spectra at the highest defect densities (Figure 4.3b) further show a red emission tail that has been attributed to defects with $ortho^+$ binding configuration and is commonly labelled E_{11}^{*-} .^{127,183} When exploring the effect of KOAc on sp^3 functionalization, slight differences in E_{11}^{*-} intensity were observed depending on KOAc concentration

(Figure 4.4). Surprisingly, the presence of KOAc did not result in higher defect densities (for a given diazonium concentration), even though the addition of KOAc to the reaction mixture was followed by an immediate yellow coloration of the solution, presumably indicating the formation of radicals^{181,182} and their coupling to longer conjugated chromophores. However, it was observed that a low KOAc concentration (on the order of the concentration of hydroxide ions in aqueous diazonium reactions¹⁰²) led to weaker E_{11}^{*-} emission and thus indicated an improved selectivity for defects with *ortho*⁺⁺ binding configuration. As quantum chemical calculations suggest a directing effect of *ortho*⁺⁺ defects that promotes the formation of *ortho*⁺ defects in their vicinity,¹⁰⁸ the latter species might be created later in the reaction. Bearing in mind that the defect density is nearly independent of KOAc concentration, the reduced E_{11}^{*-} intensity might be due to decomposition of non-adsorbed diazonium salt in the solution thus preventing its delayed reaction with the nanotube and preferential *ortho*⁺ formation. Because of the slightly higher selectivity, all reactions in this Chapter were conducted in the presence of KOAc (according to Route I, Section 3.2.1), but since the difference is rather small, KOAc was later omitted (Route II) in the preparation of samples for Chapter 6 to simplify the procedure.

4.4 Optimization of emission efficiency

Since diazonium chemistry selectively produces the E_{11}^{*-} -emitting binding configuration in (6,5) SWNTs,¹²⁷ the remaining parameters that can be tuned synthetically are the defect density and the electron-withdrawing character of the attached functional group. In particular, the defect density of the functionalized SWNTs must be matched to the targeted application. For example, if defects are to be employed as single-photon sources,¹⁵⁶ each nanotube should ideally carry only a single defect. Due to the statistical defect density distribution in ensemble-functionalized SWNTs, this scenario has not been realized yet. On the other hand, when defects are introduced to raise the PLQY or shift the emission wavelength of SWNTs, the ideal defect density is the one that maximizes the PLQY of the ensemble of SWNTs. As the latter case is of special interest for the use of functionalized SWNTs in light-emitting devices, this Section focuses on optimizing the ensemble PLQY.

To accurately evaluate the PLQY of the defect-associated E_{11}^* transition and the potential overall brightening of SWNT photoluminescence, the PLQY was determined by an absolute method utilizing an integrating sphere (Section 3.4.4).^{20,172} The total PLQY of a sample is related to the integral of its emission spectrum over the full spectral range of emission (generally within the InGaAs detection window of 900-1600 nm). However, the emission intensity may be distributed over several PL signals, such as the E_{11} and E_{11}^* in the case of sp^3 functionalized (6,5) SWNTs. If so, it is useful to restrict the integration to the spectral range of each transition and thereby to assign a PLQY to a particular transition. Of course, these individual PLQYs sum up to the total PLQY as described above. Such a definition is valuable in practice, because any application will require the emitted light to fall within a certain wavelength range.

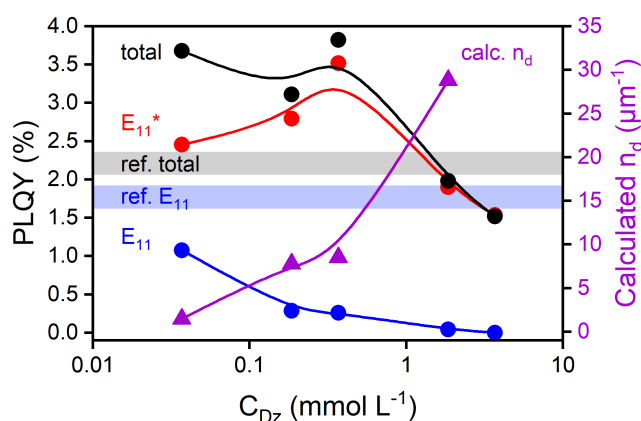


Figure 4.5: Total PLQY and spectrally-resolved contributions from E_{11} (900-1080 nm) and E_{11}^* (1080-1320 nm, including a small contribution from the E_{11}^{*-} band) measured on dispersions of (6,5) SWNTs treated with different concentrations of NO_2 -Dz. The E_{11} and total PLQYs of a reference sample of pristine (6,5) SWNTs are indicated by blue and gray shading, respectively. The corresponding densities of luminescent defects n_d calculated from a diffusion-limited contact quenching model are displayed in purple.

Figure 4.5 shows the total PLQY and the spectral contributions from E_{11} and E_{11}^* for dispersions of (6,5) SWNTs with different densities of 4-nitrophenyl defects. Shaded areas further indicate the E_{11} and total PLQY of a pristine (6,5) SWNT reference. Note that the discrepancy between the two values arises from a significant photoluminescence sideband contribution at wavelengths > 1080 nm (compare Section 2.1.4).

As expected, the E_{11} PLQY drops monotonically as a function of diazonium concentration and ultimately vanishes owing to trapping of E_{11} excitons at an increasing

density of luminescent sp^3 defects. In turn, even low diazonium concentrations result in strong E_{11}^* emission. With increasing C_{Dz} , the E_{11}^* PLQY passes through a maximum at 0.37 mmol L^{-1} and then falls off once the lattice becomes too disordered for radiative relaxation of excitons. Under optimal functionalization conditions, the E_{11}^* and total PLQY amount to 3.5% and 3.8%, respectively. Thus, more than 90% of photons are emitted in the E_{11}^* band centered around 1170 nm. Interestingly, a high total PLQY (3.7%) is also obtained at a very low defect density ($\sim 0.037 \text{ mmol L}^{-1}$) thanks to combination of efficient E_{11} and E_{11}^* emission, which has not been observed for functionalization in aqueous dispersions.¹⁰² It appears that this PLQY maximum is only accessible when the initial E_{11} PLQY is sufficiently high, as is the case for long, polymer-wrapped (6,5) SWNTs.²⁰

Until now, the defect density was measured by the concentration of employed diazonium salt, but of course it would be highly desirable to know the actual number density of defects per micrometer tube length. Unfortunately, this quantity is hard to determine due to the small footprint of a single defect site ($\sim 1 \text{ nm}^2$) and limitations in spatial resolution.^{184,185} To at least estimate the defect density, a model based on diffusion-limited contact quenching (DLCQ) of excitons will be used, which was introduced for pristine SWNTs by Hertel *et al.*¹⁰¹ and extended to functionalized SWNTs by Miyauchi *et al.*¹¹⁵

Since diffusion to exciton quenching sites and luminescent defects are the dominating decay pathways for E_{11} excitons,¹¹⁵ the drop of E_{11} PLQY in a functionalized tube with respect to the pristine tube can be used to estimate the density of defects. Within this framework, the E_{11} PLQY of the pristine SWNT is controlled by the density of (unintentional) quenching sites n_q . In addition, sp^3 functionalization introduces luminescent defects at a density n_d , which also quench E_{11} excitons by transferring them to the defect state (E_{11}^*). Making use of the absolute PLQYs measured for pristine and functionalized (6,5) SWNTs, the assumption of diffusion-limited contact quenching yields a simple expression for the density of luminescent defects

$$n_d = n_q \left(\sqrt{\frac{\eta}{\eta^*}} - 1 \right) = \sqrt{\frac{\pi}{2\eta D \tau_{rad}}} \left(\sqrt{\frac{\eta}{\eta^*}} - 1 \right) \quad (4.1)$$

where η and η^* are the E_{11} PLQY in pristine and functionalized SWNTs, respectively, D is the exciton diffusion constant and τ_{rad} is the radiative lifetime of the E_{11} exciton.^{101,115} The calculated density of luminescent defects using $D = 10.7 \text{ cm}^2 \text{ s}^{-1}$ and $\tau_{rad} = 3 \text{ ns}$, as reported by Hertel *et al.*¹⁰¹ and Hofmann *et al.*,¹⁸⁶ is plotted along with the PLQY data in Figure 4.5. For the maximum E_{11}^* and total PLQY, a density of about 9 sp^3 defects per μm is found. Given that unintentional quenching sites (of density n_q) effectively cut the nanotube into segments with a typical length of $\sim 100 \text{ nm}$ ¹⁰¹ that are explored by mobile E_{11} excitons, $n_d = 9 \mu\text{m}^{-1}$ corresponds to roughly one luminescent defect per nanotube segment. As long as the excitation density is low and state-filling may be neglected,¹²⁶ as was the case in the PLQY measurement, it is intuitive to expect that the maximum E_{11}^* emission efficiency is reached once each tube segment in an ensemble of SWNTs is occupied by one luminescent defect; in accordance with the maximum E_{11}^* PLQY for $n_d \sim 9 \mu\text{m}^{-1}$ in Figure 4.5. A confirmation of this microscopic picture, however, would require super-resolved information on the relative positions of quenching sites and luminescent defects and is thus challenging. In Section 4.6 below, the defect density estimated within the DLCQ model will be correlated with other spectroscopic metrics which are more easily accessible than the PLQY and therefore of high practical relevance.

In order to further optimize the E_{11}^* PLQY, the influence of the substituents on the aryl defects was explored. The main effect of the substituent is to slightly modify the depth of the exciton trapping potential and thus the emission wavelength^{102,129} as demonstrated in Figure 2.10. But since the reactivity of diazonium salts generally increases with the electron-withdrawing nature of the functional group,¹⁰² changing the substituent also results in a different defect density for the same diazonium salt concentration. To decouple these aspects, the PLQY was measured as a function of diazonium salt concentration (compare Figure 4.5) for aryl defects with substituents ranging from electron-donating to electron-withdrawing character and the C_{Dz} yielding the maximum E_{11}^* PLQY was identified in each case. For Br-Dz and NO_2 -Dz the optimum C_{Dz} was found to be 0.37 mmol L^{-1} , whereas the electron-rich OMe-Dz required 3.7 mmol L^{-1} and the electron-poor Cl_2 -Dz only $0.037 \text{ mmol L}^{-1}$. The E_{11}^* and total PLQYs extracted under these optimal conditions are shown in Figure 4.6a as a function of the optical trap depth ΔE_{opt} associated with each defect type. Additionally,

typical ranges of the E_{11} and total PLQY of pristine, shear-mixed (6,5) SWNTs are marked by gray shading.

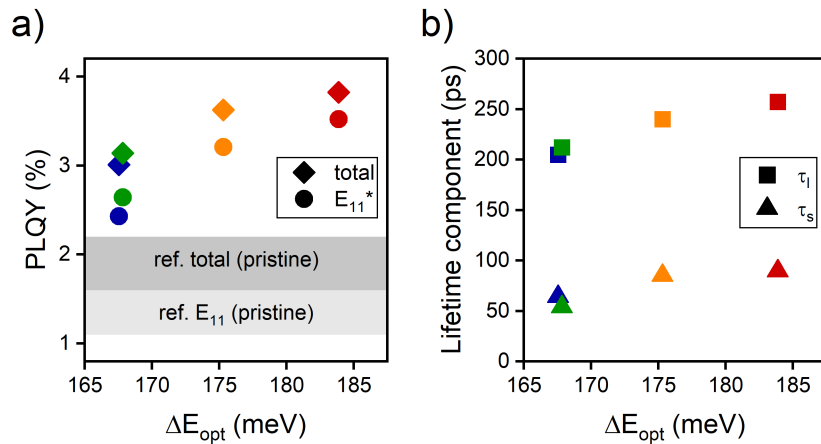


Figure 4.6: (a) Total and E_{11}^* PLQY as a function of the optical trap depth $\Delta E_{opt} = E_{11} - E_{11}^*$. (b) Long and short lifetime components (τ_l , τ_s) as a function of ΔE_{opt} . The optical trap depth is tuned by the substituent on the aryl group and increases along the series: 4-methoxy (blue); 3,5-dichloro (green); 4-bromo (orange); 4-nitro (red).

The E_{11}^* PLQY clearly increases with ΔE_{opt} and accounts for an increasing share of the total PLQY. More precisely, the E_{11}^* PLQY rises from 2.4% for 4-methoxyphenyl to 3.5% for 4-nitrophenyl, while the total PLQY increases from 3.0% to 3.8%. Hence, the total PLQY is enhanced to a degree that depends on the type of aryl defect and may vary from a factor of 1.4 to 1.7 across the investigated series. On the other hand, the PLQY appears to saturate for deep optical traps and thus, it is unlikely that PLQYs substantially greater than 4% are achievable by synthetic tuning of ΔE_{opt} alone.

To better understand the dependence of PLQY on ΔE_{opt} , the PL decay at the E_{11}^* peak emission wavelength of each defect type was recorded using time-correlated single-photon counting (TCSPC). Subsequently, a bi-exponential model was reconvolution-fitted to the data to extract the decay times (τ_s , τ_l). As summarized in Section 2.2.3, the bi-exponential decay is commonly interpreted as a fast redistribution of trapped exciton population among bright and dark states, which is followed by slow exciton recombination through radiative and non-radiative channels.^{104,105} The fits reveal a long decay component τ_l on the order of a few 100 ps and a short component τ_s of a few 10 ps in good agreement with previously reported data for sp^3 functionalized (6,5) SWNTs.^{104,105} Furthermore, the evolution of PL lifetime parallels that of the PLQY showing an increase as a function of ΔE_{opt} (Figure 4.6b).

Since the radiative E_{11}^* lifetime is usually assumed to be on the order of 1 ns for all defect types,¹⁰⁵ the correlation of the E_{11}^* PL lifetime with ΔE_{opt} indicates the slowing-down of non-radiative decay mechanisms for deeper exciton traps. This behavior matches the observation by He *et al.* that for a given nanotube host the E_{11}^* PL lifetime increases for longer emission wavelengths.¹⁰⁵ Surprisingly, when the same defect type is compared on different nanotube hosts, the opposite trend is observed and the E_{11}^* PL lifetime drops for longer wavelengths.¹⁰⁴ In concise terms, an increase of PL lifetime for longer wavelengths points toward thermal detrapping of excitons as the main non-radiative relaxation mechanism, whereas a decrease of PL lifetime for longer wavelengths supports multi-phonon decay as the main loss channel. Consequently, the data in Figure 4.6b is in agreement with thermal detrapping being the dominating non-radiative pathway in sp^3 functionalized (6,5) SWNTs at room temperature. Despite the large optical red-shift ($\Delta E_{opt} \sim 170$ meV), the rate of thermal detrapping was estimated to be on the order of a few 100 ps,¹⁰⁵ thus similar to the observed values of τ_l . Additional ground state^{10,102} as well as excited state structural deformations at the defect site¹¹³ could further facilitate thermal detrapping and rationalize its prominent role in the room-temperature dynamics of defect-localized excitons.

4.5 Role of initial nanotube quality

While the dependence of PLQY and lifetime on defect density and optical trap depth are similar to previous findings,^{102,105} the overall PLQY enhancement of a factor of ~ 1.7 is in stark contrast to the reported 5- to 10-fold brightening (depending on aryl substituent) reported for sp^3 defect creation in aqueous (6,5) SWNT dispersions.¹⁰² Moreover, the recently reported sp^3 functionalization of ultrashort (~ 40 nm) SWNTs gave rise to an extraordinarily strong PL enhancement.¹⁸⁴ In view of these observations, the initial quality of the to-be-functionalized SWNTs could be responsible for variations in the PL brightening upon sp^3 functionalization. In particular, the shear mixed SWNTs studied in this work feature long average tube lengths ($> 1 \mu\text{m}$ as shown below) and high PLQY ($\sim 2\%$), thus indicating a comparatively low density of processing-induced exciton quenching sites in the nanotube lattice. In contrast to that, surfactant-encapsulated SWNTs in water are often obtained from harsh tip sonication

damaging the SWNT structure. On top of that, subsequent chirality sorting by gel chromatography may further remove long nanotubes from the ensemble. As a result, the average tube lengths in such dispersions are frequently in the range of only 350-700 nm.^{105,175}

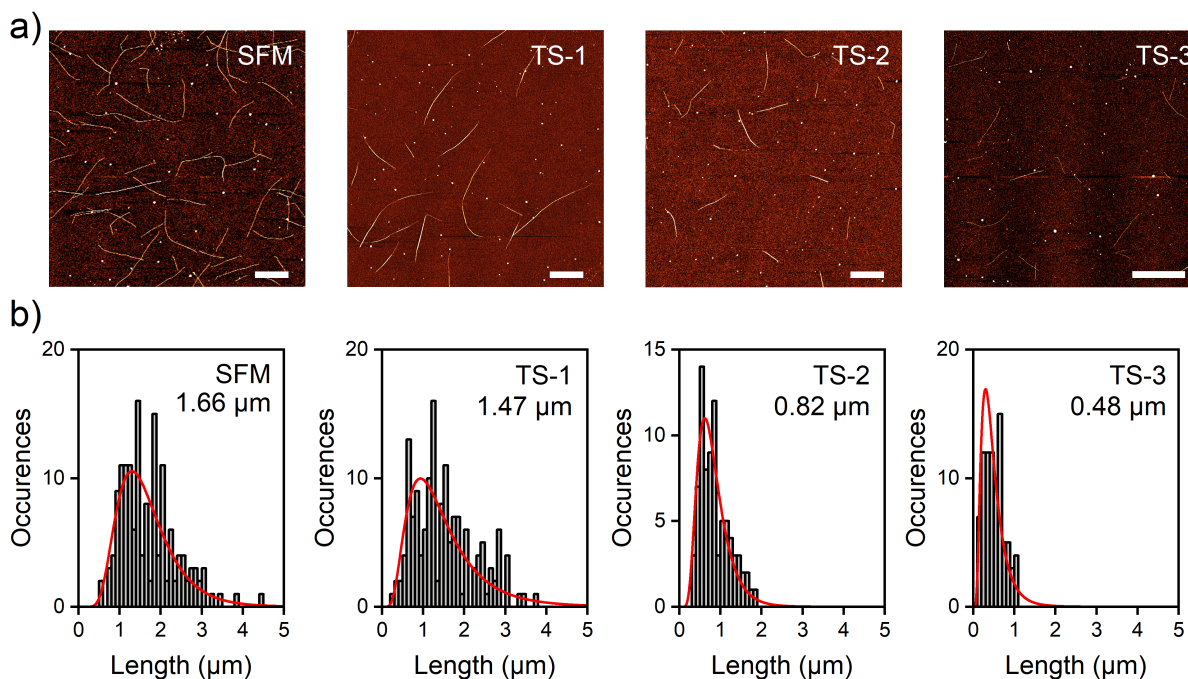


Figure 4.7: (a) Atomic force micrographs of shear force mixed and intentionally shortened (6,5) SWNTs deposited on native silicon wafers. As-mixed SWNTs (SFM) are compared with batches subjected to additional 4.5 h (TS-1), 12 h (TS-2) or 23 h (TS-3) of tip sonication. All scale bars are 1 μm . (b) Histograms of tube lengths and log-normal distribution fits (red lines) to the data. The average tube length is noted in each panel.

To test the hypothesis that the defectiveness of the SWNT starting material affects the functionalization-induced PL enhancement, shear-mixed, polymer-wrapped (6,5) SWNTs were intentionally shortened³⁴ by tip sonicating the dispersions after the usual sorting procedure. The degree of tube shortening was controlled by the duration of tip sonication as described in Section 3.1. In this way, the case of defective SWNT starting material is mimicked without compromising the chiral purity of the sample or the need to change the dispersion medium.

Since the nanotube length is the best indicator of SWNT quality, atomic force micrographs (Figure 4.7) were acquired to determine the tube length distribution of the as-mixed SWNTs and the tip-sonicated batches. As expected, the tubes are shortened from an average length of 1.7 μm for the shear force mixed stock to 0.5 μm for the

longest sonication time. As shown in Figure 4.8, this tube shortening is accompanied by a drop in PLQY from 1.6 % to 0.7 %. Interestingly, the PLQY decreases sharply even for a minor reduction of average tube length. This behavior is likely due to creation of sidewall defects, which do not cut the nanotube, but still quench E_{11} excitons.¹⁰¹

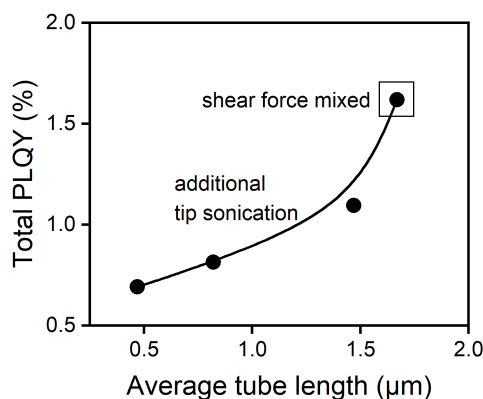


Figure 4.8: Total PLQY of PFO-BPy-wrapped (6,5) SWNTs in toluene as a function of the average tube length in the sample.

After characterizing the pristine and length-tailored SWNT batches, each sample was treated with Br-Dz at a concentration of 0.37 mmol L^{-1} , which yielded the highest PLQY in the screening experiment described in Section 4.4. Based on other studies,^{176,184} it might be expected that more defective SWNTs were also more susceptible to chemical attack and thus, a higher density of luminescent defects would be generated for a given concentration of diazonium reagent. However, the PL spectra recorded after functionalization (Figure 4.9a) did not support this picture, as the E_{11}^*/E_{11} PL intensity ratio was nearly independent of the dispersion history of the sample. In contrast to that, the spectrally-integrated PLQYs before and after functionalization were clearly affected by the dispersion scheme.

While sp^3 functionalization increases the PLQY of all SWNT batches, the absolute value of the final PLQY after functionalization decreases for longer tip sonication times or equivalently, lower initial PLQY. However, the brightening factor, which is defined here as the ratio of final PLQY/initial PLQY, reveals that more damaged SWNTs experience a greater relative enhancement of PLQY (Figure 4.9b). This inverse relationship between the quality of the nanotube starting material and the sp^3 defect-induced relative brightening suggests that the long tubes and low quenching site densities

of shear-mixed (6,5) SWNTs are at least partially responsible for the comparatively low brightening factor observed in this work (~ 1.7 -fold). Despite the small relative brightening of high-quality SWNTs, they still display the highest absolute PLQY among the functionalized SWNT batches, which is an intuitive result given that quenching sites in low-quality SWNTs interfere with E_{11} exciton diffusion and thereby reduce the efficiency of exciton capture by luminescent defects.

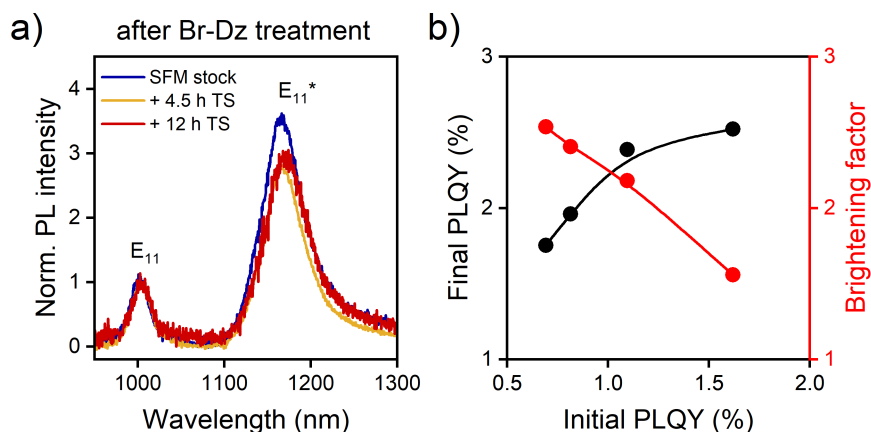


Figure 4.9: (a) Normalized PL spectra of different batches of (6,5) SWNTs after functionalization with Br-Dz measured inside an integrating sphere. (b) Final PLQY (after functionalization) *versus* initial PLQY (before functionalization) and calculated brightening factor, which is defined as the ratio of final PLQY / initial PLQY. Note that the total PLQYs, *i.e.*, integrated over both the E_{11} and the E_{11}^* transition, are compared.

The remaining difference between the 2.5-fold brightening for the shortest nanotubes in this study and the 7-fold enhancement reported for aqueous dispersions of (6,5) SWNTs with the same defect type (4-bromophenyl)¹⁰² is likely due to the fact that the SWNTs dispersed in water were even shorter on average¹⁷⁵ than the shortest tubes characterized here. In addition, Figure 4.9b points toward a PLQY saturation for long nanotubes in a low-polarity environment (PFO-BPy-wrapped in toluene). Conversely, due to the lower initial PLQY of the SWNTs dispersed in water, such nanotubes may have a wider scope of PLQY enhancement.

4.6 Defect density metrics

As described in Section 4.4 above, the functionalization-induced drop of E_{11} PLQY can be used to estimate the defect density per unit tube length (Equation 4.1). But because

absolute PLQY measurements are laborious and require special instrumentation, empirical spectroscopic metrics for the defect density are of great practical relevance. Therefore, this Section compares the density of luminescent defects n_d calculated from PLQY measurements with several metrics that are easily extracted from standard characterization including Raman, absorption and photoluminescence spectra. Beyond that, the calculated defect density will be used to obtain an order-of-magnitude estimate of the oscillator strength of the E_{11}^* transition. Note that all the data shown in this Section were measured on (6,5) SWNTs functionalized with Br-Dz. The PLQY data used to compute n_d are not shown explicitly, but follow the usual trend as exemplified in Figure 4.5.

The most commonly employed defect density metric is the ratio of D to G^+ mode intensities in the Raman spectrum of SWNTs.^{187,188} As the G^+ mode corresponds to a longitudinal-optical phonon of the pristine lattice of semiconducting SWNTs,¹⁸⁹ its intensity is proportional to the number of sp^2 hybridized carbon atoms. By contrast, the D mode is Raman-inactive in ideal nanotubes, but gains intensity from symmetry-breaking sp^3 defects.¹⁸⁸ Hence, the D/ G^+ intensity ratio may serve as a measure of sp^3 defect density. Unlike for graphite,^{190,191} however, a precise relation to the defect density (that holds over a wide range of defect concentrations¹⁹²) is not established for SWNTs. Therefore, only relative comparisons can be made between samples.

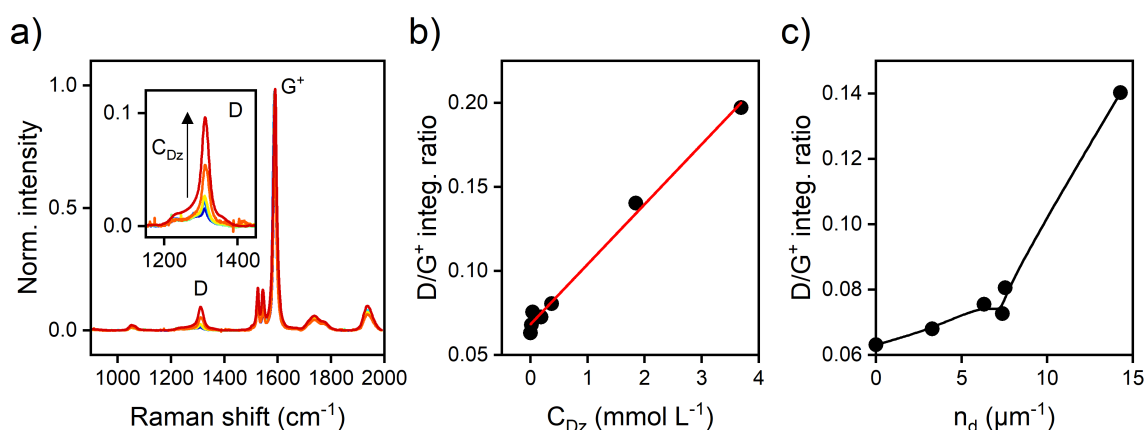


Figure 4.10: (a) Raman spectra of (6,5) SWNTs functionalized with different concentrations (C_{Dz}) of Br-Dz. The inset shows the D mode region. Incident laser wavelength: 532 nm. (b) Spectrally-integrated D/ G^+ mode intensity ratio as a function of diazonium concentration. The red line is a linear fit to the data. (c) D/ G^+ mode intensity ratio plotted *versus* the density of luminescent defects calculated from PLQY data. The line is a guide to the eye.

Figure 4.10a shows Raman spectra of (6,5) SWNTs that were reacted with different concentrations of Br-Dz. The increasing degree of functionalization is clearly reflected in a rising D mode intensity in the G^+ -normalized spectra. Since the D/G^+ intensity ratio is assumed to be proportional to the sp^3 defect concentration, its linear scaling with diazonium concentration (Figure 4.10b) suggests that the conversion efficiency of diazonium molecules to sp^3 carbon atoms is roughly constant across the investigated concentration window ($\mu\text{mol L}^{-1}$ – mmol L^{-1}). On the other hand, plotting the D/G^+ intensity ratio *versus* the density of luminescent defects calculated from PLQY data (Figure 4.10c) reveals deviations at high defect densities. In the low-density regime, the D/G^+ intensity ratio is approximately proportional to the calculated defect concentration, but at high densities, it is substantially larger than expected from the PLQY measurement. Such a deviation could potentially arise from clustering of defects.^{176,184} In this picture, the D/G^+ intensity ratio measures the real density of sp^3 carbon atoms in the lattice, whereas diffusive exciton quenching (which defines the PLQY and hence, n_d) does not distinguish between an individual defect and a small cluster of closely spaced (~ 1 nm) or directly neighboring defects owing to the large exciton diffusion lengths (~ 100 nm).¹⁰¹ As a result, the n_d calculated from the E_{11} PLQY underestimates the density of sp^3 carbon atoms and thus leads to the observed deviation at high defect levels. The hypothesis of defect clustering is further supported by the nearly constant E_{11}^* Stokes shift at low C_{Dz} (compare Figure 4.3c), which starts to decrease only above a certain C_{Dz} . This trend could be explained by excitonic state delocalization over multiple defect centers and corresponding reduction of reorganization energy.

It is worth noting that a general drawback of the D/G^+ metric is the relatively large uncertainty at low defect densities, which is the primary range of interest for luminescent defects. This data scattering, as evident from (Figure 4.10b), is presumably related to batch-to-batch variations in the density of unintentional defects, *i.e.*, tube ends and other quenching sites.¹⁹³

Other easily accessible defect density metrics are the E_{11}^* to E_{11} signal ratios in absorption and emission. However, their precise dependence on the density of defects is not obvious, especially with respect to effects like absorption bleaching and PL quenching at the highest defect densities.^{102,136} Figure 4.11 shows the calculated n_d alongside both metrics as a function of the diazonium concentration employed in the reaction.

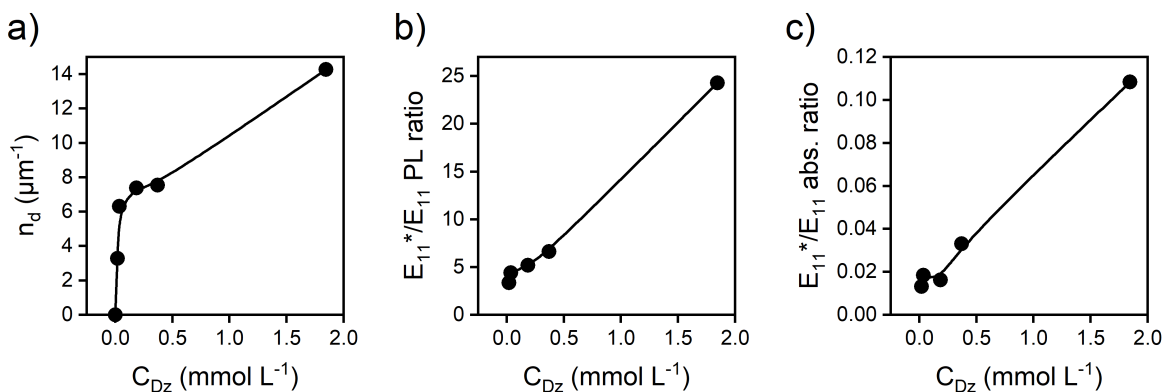


Figure 4.11: (a) Density of luminescent defects calculated from PLQY data plotted *versus* the diazonium concentration employed in the reaction. Spectrally-integrated E_{11}^*/E_{11} (b) absorbance and (c) photoluminescence ratio plotted *versus* the diazonium concentration. Lines are guides to the eye.

As hypothesized above, the slower increase of n_d at high defect levels (Figure 4.11a) might be due to clustering. Nevertheless, both the E_{11}^*/E_{11} photoluminescence and the absorbance ratio scale roughly linearly with diazonium concentration (Figure 4.11b,c) even in the range of suspected clustering. Since C_{Dz} was concluded to be proportional to the sp^3 carbon concentration, both E_{11}^*/E_{11} signal ratios may be used as empirical metrics of sp^3 defect density, although a deeper understanding of their relation is still lacking.

Finally, combined information on the density of luminescent defects (estimated by n_d) and the E_{11}^* absorbance gives access to the oscillator strength of defect-localized excitons. In turn, this enables the determination of the average defect concentration in an ensemble of sp^3 functionalized SWNTs. The main limitations of this approach are that the E_{11}^* absorbance must be above the detection limit, but at the same time the bleaching of E_{11} absorbance must remain small, because otherwise the concentration of nanotube carbon atoms cannot be determined. Therefore, this method works best for moderate defect densities, which are of great importance, since they often yield the highest PLQYs.

The intensity of an optical transition can be characterized by various quantities that may be used interchangeably. Here, spectrally-integrated metrics (from 1096-1221 nm for the E_{11}^* band) are preferred over peak metrics, because they are insensitive to variations in signal width and hence more robust.¹¹⁴ Firstly, the integrated molar

absorptivity of the E_{11}^* transition was obtained as the slope of a linear fit (Figure 4.12) according to¹¹⁴

$$\int \frac{A}{l} d\lambda = c_d \int \epsilon_{11}^* d\lambda \quad (4.2)$$

where A is the decadic absorbance, l the path length, c_d the molar defect concentration and the integration is performed on wavelength scale. The total concentration of carbon atoms in the sample was calculated from the E_{11} molar absorptivity reported by Streit *et al.* and c_d was derived from this value using n_d from PLQY data and the geometrical factor¹⁹⁴ of 88 carbon atoms per nanometer tube length in (6,5) SWNTs.

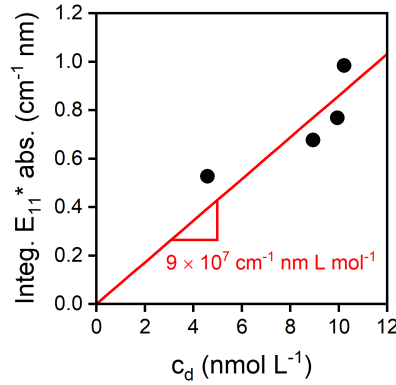


Figure 4.12: Spectrally-integrated, absolute E_{11}^* absorbance of 4-bromophenyl-functionalized (6,5) SWNTs plotted *versus* the concentration of luminescent defects calculated from PLQY data.

Secondly, the integrated absorption cross-section was determined along similar lines employing¹¹⁴

$$\int \frac{A}{l} dv = \rho_d \int \sigma_{11}^* dv \quad (4.3)$$

where ρ_d denotes the defect density per unit volume and the integration is carried out on wavenumber scale. Finally, the oscillator strength f was found from¹⁹⁴

$$f = \frac{4\epsilon_0 c^2 m_e \ln(10)}{N_A e^2} \int \epsilon_{11}^* dv \quad (4.4)$$

with ϵ_0 being the permittivity of vacuum, c the speed of light, m_e the electron mass, N_A Avogadro's number and e the elementary charge. Table 4.1 summarizes the extracted

quantities and compares them with literature values¹¹⁴ for the E_{11} transition of (6,5) SWNTs.

Table 4.1: Spectrally-integrated molar absorptivity, absorption cross-section and oscillator strength for the E_{11} (from Streit *et al.*¹¹⁴) and E_{11}^* transition of (6,5) SWNTs, respectively. Note that E_{11} metrics are per carbon atom, whereas E_{11}^* metrics are per defect site.

| Optical transition | $\int \epsilon d\lambda$ ($\text{cm}^{-1} \text{ nm L mol}^{-1}$) | $\int \sigma d\nu$ (cm) | f |
|--|---|-------------------------|------|
| E_{11} (per carbon atom ¹¹⁴) | 2.34×10^5 | 9.24×10^{-15} | 0.01 |
| E_{11}^* (per defect site) | 9×10^7 | 3×10^{-12} | 3 |

Apparently, the oscillator strength of a single defect site is a factor of ~ 300 larger than that of an individual carbon atom contributing to an E_{11} exciton. However, this seemingly large discrepancy is primarily caused by the different choice of units (per carbon atom *versus* per defect site). When an exciton becomes localized around an individual sp^3 carbon center, its size (or electron-hole correlation length) is still in the range of 1 to a few nm^{8,128} thus covering a few hundred carbon atoms that contribute to its oscillator strength. After dividing by this conversion factor of ~ 100 , the oscillator strengths of the E_{11} and E_{11}^* transitions should be quite similar and both on the order of 0.01 per carbon atom. Previously, a localization-induced enhancement of oscillator strength by a factor of 2 was proposed by Miyauchi *et al.*¹¹⁵ The results presented here support that the oscillator strength of the E_{11}^* is on the same order of magnitude as that of the E_{11} transition, but the available data is not sufficiently accurate to resolve changes as small as a factor of 2.

4.7 Summary and conclusion

In summary, this Chapter described the first liquid-phase functionalization protocol for polymer-wrapped SWNTs that generates luminescent defects. Ether crown complexation was used to solubilize pre-formed aryldiazonium salts in organic solvents and thereby facilitated their reaction with polymer-sorted SWNTs at room temperature. During the reaction, the PL from the nanotubes was strongly quenched, presumably due to adsorbed diazonium cations, but bright PL was recovered after washing the SWNTs and re-dispersing them in fresh solvent. This simple and scalable approach enables the decoration of long, electronically-pure semiconducting SWNTs with

emissive defects and thus dramatically expands their application potential. As will be demonstrated in Chapter 6, such nanotubes can be deposited as high-quality thin films and are readily integrated into light-emitting devices, thus paving the way for electrically-pumped emission from sp^3 defects.

The introduction of aryl defects with electron-withdrawing substituents and careful tuning of the defect density resulted in PLQYs of up to $\sim 4\%$ with about 90% of photons emitted in the E_{11}^* band. Such comparatively high PLQYs are possible thanks to the large tube lengths and low quenching site densities of shear-mixed, PFO-BPy-wrapped (6,5) SWNTs. While longer nanotubes display higher absolute PLQYs before and after functionalization, the relative brightening shows an inverse trend with the greatest PL enhancement experienced by the most defective starting material.

In addition, the dispersions of polymer-wrapped and sp^3 functionalized (6,5) SWNTs featured well-resolved absorption spectra with low scattering background and negligible contribution from minority chiralities. Under these conditions, the E_{11}^* absorption band arising from sp^3 defects could be unambiguously detected. The Stokes shift of the E_{11}^* transition amounts to only 20 meV in the low defect density limit and decreases further as the level of functionalization increases, thus pointing toward clustering of defects at high densities. Upon estimating the defect concentration from the reduction of E_{11} PLQY within a diffusion-limited contact quenching model, an oscillator strength of about 3 is obtained for the defect-localized exciton. After accounting for the exciton size of a few nanometers, the oscillator strength of the trapped E_{11}^* exciton is estimated to be around 0.01 per carbon atom and is thus very similar to that of the mobile E_{11} exciton.

Chapter 5

Interaction of Defect-Localized Excitons with Stable Organic Radicals

This Chapter explores how the dynamics of defect-localized excitons are modified under the influence of functional groups carrying a net spin.

The results of this Chapter were published* in Berger *et al.*, *ACS Nano* **2021**, *15*, 5147-5157.¹⁹⁵ Modified reprints of previously published Figures are presented with permission of the American Chemical Society. The PTM- and PTMH-substituted diazonium salts were synthesized by J. Alejandro de Sousa and Aleix Quintana García under the supervision of Núria Crivillers at the Institut de Ciència de Materials de Barcelona. The EPR data presented in Sections 5.2 and 5.4 were collected by Vega Lloveras at the Institut de Ciència de Materials de Barcelona. The low-temperature PL and magneto-PL data discussed in Section 5.7 were acquired by Shen Zhao under the supervision of Alexander Högele at the Faculty of Physics of the Ludwig-Maximilians-Universität München.

5.1 Introduction

The previous Chapter dealt with the optical properties of (6,5) SWNTs functionalized with aryl groups bearing structurally simple substituents that did not perform any function other than to slightly modify the exciton trapping potential. There were several reasons for this approach: First of all, as discussed in Section 2.2.4, theoretical^{8,107} and experimental studies¹⁰² showed that the substituent on the aryl group has only a minor influence on the optical trap depth. Although shifts up to 25 meV are feasible with strongly electron-withdrawing groups, they are still small compared to shifts (> 50 meV) between the *ortho*⁺ and *ortho*⁺⁺ defect binding configurations, which are controlled by the functionalization chemistry rather than the substituents on the attached moiety.¹²⁷ Moreover, diazonium salts with substituents such as nitro (-NO₂) groups are commercially available and are already sufficiently electron-withdrawing to create deep exciton traps.¹⁰²

On the other hand, the ability to pin excitons to the point of *sp*³ functionalization unlocks a wide range of options to tune the excitons' properties through their interaction with covalently attached groups. For example, the changes in defect state energy, and hence E_{11}^* PL wavelength, induced by the binding of analytes to functional groups on

*URL: <https://pubs.acs.org/doi/10.1021/acsnano.0c10341>. Requests related to the reuse of this material should be directed to the American Chemical Society.

sp^3 defects can be used for optical sensing of pH¹⁹⁶ or biologically relevant compounds such as sugars¹⁹⁷ or metal salts.¹⁹⁸

More profound changes in the properties of defect-localized excitons might arise from their interaction with substituents carrying a net spin. In the past, metallic single-walled or multi-walled carbon nanotubes, which do not exhibit any photoluminescence (PL), were decorated with open-shell transition metal¹⁹⁹ or lanthanide complexes^{200,201} and used to fabricate devices with magnetic field-switchable electrical resistance, commonly referred to as spin valves.^{69,202,203}

In contrast to that, this Chapter describes the first covalent functionalization of purified semiconducting SWNTs with stable organic radicals anchored to the nanotube *via* luminescent sp^3 defects. The attached perchlorotriphenylmethyl (PTM) group exhibits a long half-life of around 100 years by virtue of a propeller-shaped arrangement of aryl groups shielding the carbon-centered radical.²⁰⁴ Consequently, such spin-labeled SWNTs are long-term stable and may find application in magnetic resonance imaging^{200,205} or spintronic devices,²⁰⁶ which could benefit from long spin-coherence times in the all-organic material.

The work presented in this Chapter focuses on using the PL of the defect-localized exciton as a probe for the interaction between the nanotube and the PTM radical which is governed by short-ranged processes such as spin exchange and electron transfer. These findings demonstrate how the interaction with nearby spins may be used to control nanotube photophysics and, in particular, the yield of triplet excitons.

5.2 Functionalization method

As in Chapter 4, shear-mixed (6,5) SWNTs wrapped with the copolymer PFO-BPy (see Figure 2.2 for molecular structure) served as the starting material for sp^3 functionalization.²⁰ Reacting these nanotubes with the custom-synthesized aryldiazonium salt PTM-Dz^{170,207} led to the formation of sp^3 defects covalently linked to perchlorotriphenylmethyl (PTM) radicals as depicted in Figure 5.1. Thanks to its non-polar PTM group, the PTM-Dz reagent was well-soluble in tetrahydrofuran (THF), which also dispersed PFO-BPy-wrapped SWNTs, thus removing any conflicts between nanotube dispersion stability and reagent solubility that had to be overcome for functionalization with

commercial diazonium salts (see Section 4.2). Hence, the reaction could be carried out in pure THF without the need for any additives as described in detail in Section 3.2.2. After 16 hours in the dark at room temperature, the sp^3 functionalized SWNTs were collected by vacuum filtration and unreacted diazonium salt and by-products were removed by rinsing with THF. Subsequently, bath sonication was applied to re-disperse the PTM-functionalized SWNTs in toluene for spectroscopic analysis.

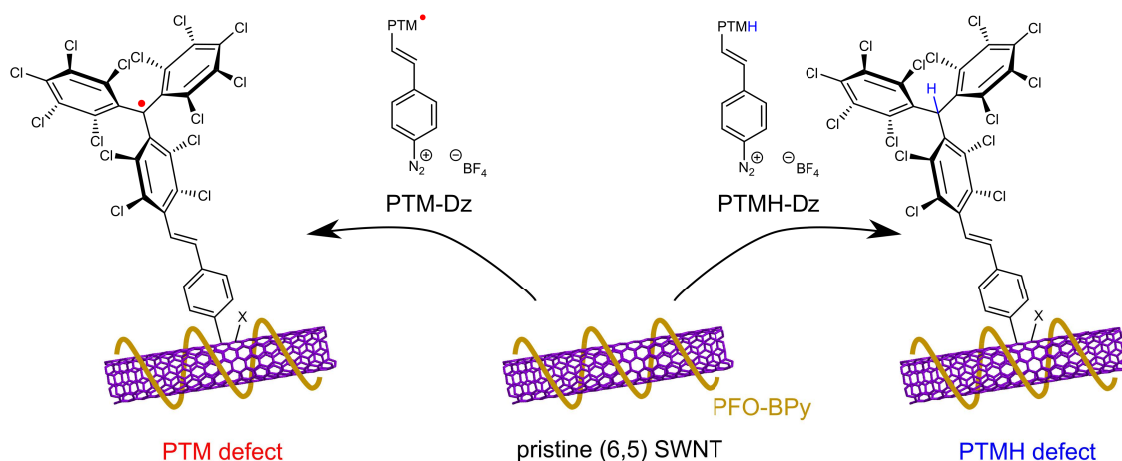


Figure 5.1: Reaction of PFO-BPy-wrapped (6,5) SWNTs with the diazonium salts PTM-Dz and PTMH-Dz creates sp^3 defects with open-shell (PTM) and closed-shell (PTMH) substituents, respectively. X denotes an auxiliary fragment of unknown molecular structure.

Since the main focus of this study was to identify the impact of the radical (open-shell) substituent on the PL of the defect-localized exciton, sp^3 defects with closed-shell substituents were required as references. For this purpose, (6,5) SWNTs were treated with the tailored diazonium salt PTMH-Dz, in which the PTM moiety was hydrogen-substituted to form a closed-shell structure (compare Figure 5.1). In addition, the method established in Section 4.2 was employed to create simple 4-bromophenyl (ArBr) defects *via* reaction with the commercial diazonium salt Br-Dz that showed a higher reactivity than PTMH-Dz and was therefore used to prepare closed-shell reference samples with larger defect densities.

5.3 Evidence for covalent radical attachment

In order to confirm the attachment of stable organic radicals to (6,5) SWNTs, the obtained nanotube dispersions were characterized by PL and electron paramagnetic

resonance (EPR) spectroscopy. The PL spectra (Figure 5.2a) of (6,5) SWNTs that were treated with PTM-Dz or PTMH-Dz both display a signal at around 1165 nm assignable to defect-localized (E_{11}^*) excitons and thus represent strong evidence for the covalent binding of molecular groups to the nanotube surface.

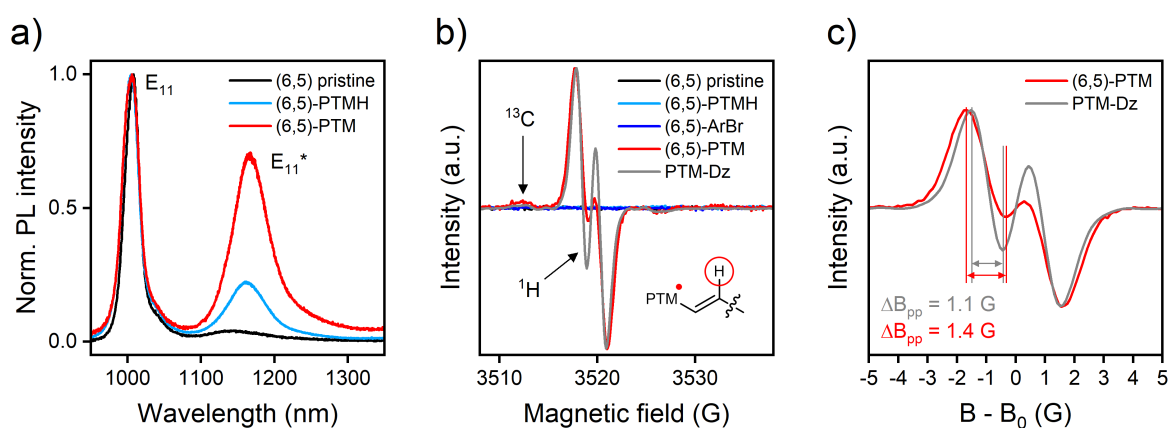


Figure 5.2: (a) PL spectra of the pristine and sp^3 functionalized (6,5) SWNT dispersions in toluene under pulsed excitation at 700 nm. (b) Room-temperature EPR spectra of these dispersions in addition to a dispersion of (6,5) SWNTs functionalized with a high density of 4-bromophenyl (ArBr) defects in toluene and a solution of PTM-Dz in tetrahydrofuran. (c) Zoom on the EPR signals of PTM-functionalized (6,5) SWNTs and the PTM-Dz reagent. Note that the magnetic field (B) is displayed as $B - B_0$ where B_0 denotes the field at the center of the signal. The extracted linewidths (ΔB_{pp}) are given in the graph.

To ascertain that the attached functional group was indeed the desired PTM-styryl unit and the radical center remained intact during the reaction, EPR spectra of the dispersions were recorded at room temperature (Figure 5.2b). As expected for purified semiconducting SWNTs with negligible concentrations of metallic catalyst particles,²⁰⁸ the dispersion of pristine (6,5) SWNTs did not show any EPR signal. Likewise, nanotubes functionalized with closed-shell PTMH defects did not give rise to any EPR response. However, as the weak E_{11}^* PL signal (Figure 5.2a) indicated only a low density of PTMH defects, an additional control experiment was performed using (6,5) SWNTs with a high density of closed-shell ArBr defects, which did not show an EPR signal either and thus confirmed the result obtained for PTMH defects. In contrast to that, the PTM-functionalized (6,5) SWNTs clearly showed the EPR signature of the PTM-styryl moiety with a g factor of 2.0024 characteristic of PTM radicals²⁰⁹ and a signal shape that closely matched the spectrum of the PTM-Dz precursor. Note that extensive washing of the nanotubes after the reaction ensured that the concentration of

unbound PTM radicals (*e.g.*, in the form of residual PTM-Dz) was negligible and thus, the observed EPR signal could be assigned to covalently attached PTM radicals.

The successful decoration of (6,5) SWNTs with stable organic radicals was further corroborated by the slight broadening of the EPR signal in PTM-functionalized SWNTs with respect to the PTM-Dz reference (see Figure 5.2c). Such a broadening is indeed expected as a consequence of the slower tumbling²¹⁰ of the PTM radical when attached to the μm -long nanotube with rotational correlation times of $\sim 10\text{ms}$ ²¹¹ which are much longer than those of the small PTM-Dz molecule.

Furthermore, the observation of identical EPR fine structure for PTM-functionalized (6,5) SWNTs and the PTM-Dz reference not only supports the covalent attachment of PTM radicals but also provides insights into the distribution of spin density at the created PTM-substituted sp^3 defects. As this fine structure results from the hyperfine coupling between the unpaired electron spin and the nuclear spins of ^{13}C carbon atoms in the PTM unit as well as the nuclear spin of the vinylic ^1H atom highlighted in Figure 5.2b, the correspondence in fine structure indicates that the spin density in PTM defects remains localized on the PTM-styryl moiety. Hence, the interaction between the radical spin and the SWNT is expected to be through-space.

In summary, the EPR signal of PTM-functionalized (6,5) SWNTs arises from an unpaired electron localized on the PTM moiety and not on the nanotube itself. In contrast to that, Lohmann *et al.*²¹² recently reported the emergence of an EPR signal at low temperatures for (6,5) SWNTs that were functionalized with sp^3 defects bearing closed-shell substituents in aqueous dispersion. In fact, similar observations were made in earlier studies on the sp^3 functionalization of SWNTs dispersed in water.^{137,213} In all cases, the authors attributed this signal to a radical localized on the nanotube that may be formed upon binding of an odd number (1, 3, ...) of aryl groups to the SWNT lattice. Since the intensity of this EPR signal dropped strongly with increasing temperature and became undetectable above 200 K,²¹² it is not expected to contribute to the room-temperature spectra discussed above (Figure 5.2b). Therefore, to search for any indications of nanotube-centered radicals in the samples studied here, a concentrated dispersion ($\text{OD} \sim 2\text{cm}^{-1}$ at the E_{11} transition) of (6,5) SWNTs with a high density of closed-shell ArBr defects was measured at 120 K, which was the lowest temperature accessible in the employed EPR spectrometer. As no EPR signal was observed even

under these conditions, it is likely that the sp^3 defects created by diazonium chemistry in organic media (Section 3.2.1) are formed in pairs and thus constitute a closed-shell structure on the nanotube as is generally assumed in models describing the defect binding configuration.¹²⁷

5.4 Impact of the radical on PL

Having confirmed the covalent attachment of PTM radicals to (6,5) SWNTs by sp^3 functionalization, PL spectroscopy was used to probe the interaction between the radical and the defect-localized exciton. As pointed out in Section 5.2, this approach relies on the comparison of the PL properties of sp^3 defects with radical (open-shell) and closed-shell substituents. Since the E_{11}^* PL characteristics depend sensitively on the optical trap depth, $\Delta E_{opt} = E_{11} - E_{11}^*$, a good closed-shell reference should have a similar ΔE_{opt} as the open-shell PTM defects to make sure that any observed differences arise from the presence of the unpaired spin and not from variations in the exciton trapping potential. As shown in Figure 5.3, the optical trap depths of the closed-shell ArBr and PTMH references are very close to that of PTM defects with deviations of merely 3 and 4 meV, respectively. Hence, both ArBr and PTMH defects are suitable closed-shell reference samples. Conversely, these results demonstrate that the presence of the radical does not change the energy of the trapped exciton to a significant degree.

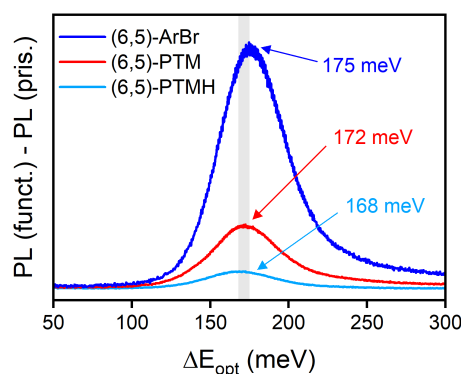


Figure 5.3: The intensity difference of the E_{11} -normalized PL spectra of sp^3 functionalized and pristine (6,5) SWNTs is plotted as a function of the optical trap depth $\Delta E_{opt} = E_{11} - E_{11}^*$. These data may be interpreted as the pure defect emission spectra without any contributions of E_{11} -associated PL sidebands and thus enable the precise determination of ΔE_{opt} even at low E_{11}^* PL intensities.

The next question that should be addressed is whether the radical affects the PL efficiency of the defect-localized exciton. The simplest way to check this is by comparing PL spectra of SWNTs with equal densities of sp^3 defects with and without radical substituents. Since the PTMH-Dz was not sufficiently reactive to produce a defect concentration comparable to that of the PTM-functionalized sample, the commercial Br-Dz was used to prepare a sample with a density of ArBr defects similar to that of PTM defects as evident from the E_{11}^*/E_{11} absorbance ratio (Figure 5.4a). Despite the matching defect densities, the PL spectra in Figure 5.4b display a markedly lower E_{11}^* PL intensity for PTM defects than for the closed-shell reference. This picture was further supported by PL lifetime measurements using time-correlated single-photon counting (TCSPC) which showed a bi-exponential decay for PTM defects, as commonly found for E_{11}^* PL at room temperature, albeit with substantially shorter lifetime components than for ArBr or PTMH defects (Figure 5.4c). Consequently, the data point toward a non-radiative decay pathway associated with the radical in close proximity to the defect-localized exciton.

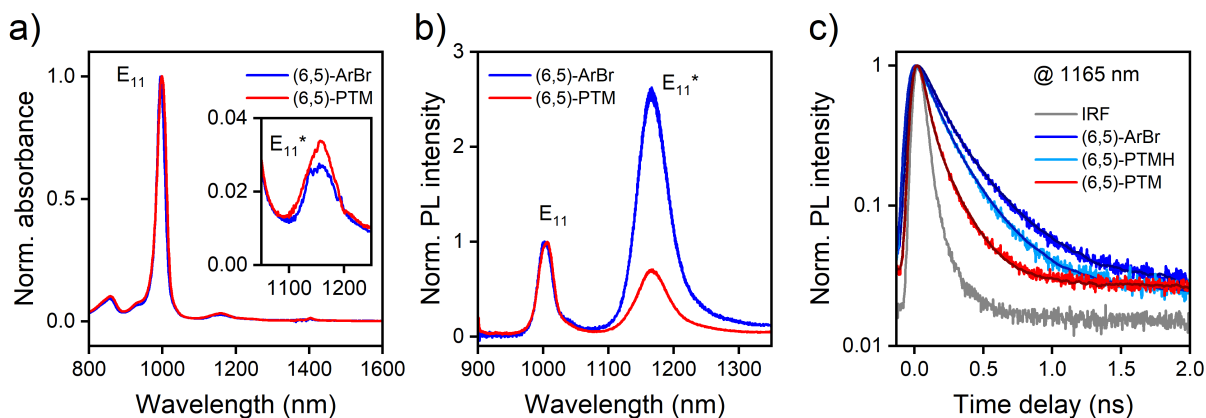


Figure 5.4: Normalized (a) absorption and (b) PL spectra of (6,5) SWNTs with similar densities of 4-bromophenyl (ArBr) and PTM defects. (c) PL decay traces recorded for E_{11}^* emission in a narrow wavelength band around 1165 nm. Dark lines represent bi-exponential fits to the decay curves accounting for the instrument response function (IRF). All data were collected for SWNT dispersions in toluene.

The most direct way to quantify this PL quenching effect and corroborate its connection to the radical character of the attached functional group is the *in situ* conversion of open-shell to closed-shell substituents on the aryl defects. For this purpose, the sensitivity of PTM radicals to UV and blue light (around their absorption maximum

at 385 nm) may be exploited. It is well-documented that irradiating PTM radicals in this spectral range triggers chlorine atom elimination followed by cyclization to the perchlorophenylfluorenyl (PPF) radical^{214,215} as illustrated in Figure 5.5a. Because of the planar fluorene structure, the radical center in the PPF is significantly more exposed to the solvent environment than that of the PTM. Therefore, fast decomposition of the PPF radical and formation of closed-shell products may be expected, for instance, by hydrogen abstraction from the solvent (toluene). Note that this photochemical conversion enables a comparison between the PL efficiencies of sp^3 defects with radical and closed-shell substituents, respectively, while keeping the defect density constant and avoiding the use of chemicals (*e.g.*, reducing agents) that might themselves affect the PL.

The procedure described above was implemented by irradiating a dispersion of PTM-functionalized (6,5) SWNTs with a UV light source (365 nm, 0.2 W cm^{-2} , Thorlabs SOLIS-365C) for 40 min and acquiring PL spectra and decay traces under the same conditions before and after irradiation. As shown in Figure 5.5b, the E_{11}^* PL intensity of PTM defects increased dramatically upon UV irradiation thus indicating the deactivation of the non-radiative decay pathway identified above. Since this transformation was accompanied by the disappearance of the EPR signal (Figure 5.5c), the E_{11}^* PL enhancement could be unambiguously attributed to the conversion of PTM radical substituents to closed-shell products. Moreover, as the E_{11} PL intensity remained unaffected, the formation of additional sp^3 defects as the origin of E_{11}^* brightening could be ruled out as it should have led to simultaneous quenching of E_{11} PL.

To also exclude any potential UV light-induced rearrangements of sp^3 defects on the SWNT surface, a dispersion of ArBr-functionalized (6,5) SWNTs was characterized in the same way. As shown in Figure 5.5d, no E_{11}^* brightening was observed. Instead, the overall PL intensity decreased slightly without any changes in spectral shape, presumably due to some SWNT aggregation. Furthermore, if the E_{11}^* PL enhancement in PTM defects results from the reduced quenching associated with radical decomposition, this should be evident in a longer E_{11}^* PL lifetime. Indeed, after irradiation, the PL lifetime of PTM defects increased to the level of the closed-shell reference defects as displayed in Figure 5.5e.

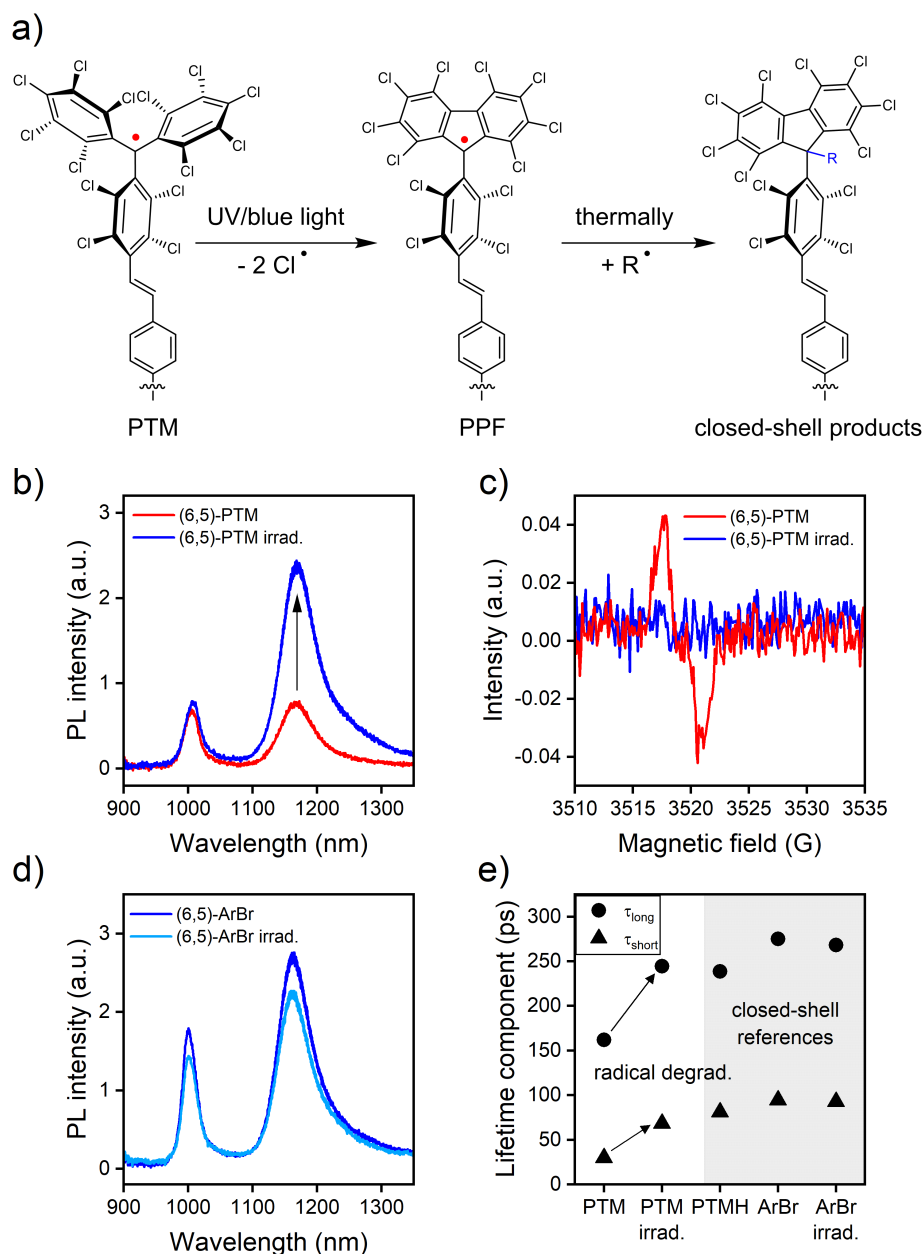


Figure 5.5: (a) Proposed reaction scheme for the *in situ* conversion of open-shell PTM defects to closed-shell species driven by irradiation at 365 nm. PL spectra of (b) PTM-functionalized and (d) ArBr-functionalized (6,5) SWNTs acquired before and after irradiation. (c) EPR spectra of the dispersion of PTM-functionalized (6,5) SWNTs used for PL characterization measured before and after irradiation. Since dilute dispersions were used for optical characterization, the initial signal level was relatively low. (e) E_{11}^* PL lifetime components extracted from bi-exponential fits to the decay traces of PTM defects and closed-shell references before and after irradiation.

Table 5.1: PL characterization for different types of sp^3 defects including the PL lifetime components (τ_l , τ_s) with the corresponding normalized amplitudes (A_l , A_s), the amplitude-averaged PL lifetime (τ_{amp-av}) and the spectrally-integrated E_{11}^*/E_{11} PL intensity ratio.

| defect | A_l (%) | τ_l (ps) | A_s (%) | τ_s (ps) | τ_{amp-av} (ps) | E_{11}^*/E_{11} PL |
|-------------|-----------|---------------|-----------|---------------|----------------------|----------------------|
| PTM | 16 | 162 | 84 | 30 | 51 | 2.6 |
| PTM irradi. | 30 | 245 | 70 | 68 | 121 | 6.5 |
| PTMH | 29 | 239 | 71 | 81 | 127 | 0.6 |
| ArBr | 31 | 275 | 69 | 95 | 150 | 3.7 |

The lifetime components extracted from bi-exponential fits to the decay traces are listed in Table 5.1 along with spectrally-integrated E_{11}^*/E_{11} PL intensity ratios for all investigated defect species. As the amplitude-averaged lifetime of PTM defects increased by a factor of 2.4 (from 51 ps to 121 ps) upon irradiation, thus matching the 2.5-fold enhancement of the E_{11}^*/E_{11} PL intensity ratio (from 2.6 to 6.5), the lower PL efficiency of radical-substituted defects can be fully accounted for by faster non-radiative relaxation and an unchanged radiative E_{11}^* lifetime in the presence of the PTM radical.

5.5 Mechanisms of interaction

The results discussed in the previous Section revealed important characteristics of the interaction between the PTM radical and the SWNT; for instance, that it is short-ranged and thus confined to defect-localized excitons. This picture was strongly supported by the data in Figure 5.5b, which showed that the E_{11}^* PL was boosted upon radical decomposition whereas the E_{11} intensity remained nearly constant in agreement with long average distances between the mobile E_{11} exciton and the defect site. Moreover, the degree of PL quenching matched the shortening of PL lifetime. Hence, the quenching process is of dynamic rather than static nature, *i.e.*, it is driven by enhanced non-radiative relaxation instead of the formation of non-luminescent complexes.²¹⁶ It is worth noting that this finding also excludes ground state charge transfer between the SWNT and the PTM with concomitant charge-induced PL quenching as the origin of reduced E_{11}^* intensity in PTM defects. In this Section, possible mechanisms underlying the PTM radical-induced PL quenching will be discussed in more detail. In most

cases, PL quenching in organic fluorophores may be attributed to one of three basic mechanisms:²¹⁶ Resonant excitation energy transfer, photoinduced electron transfer or enhanced intersystem crossing.

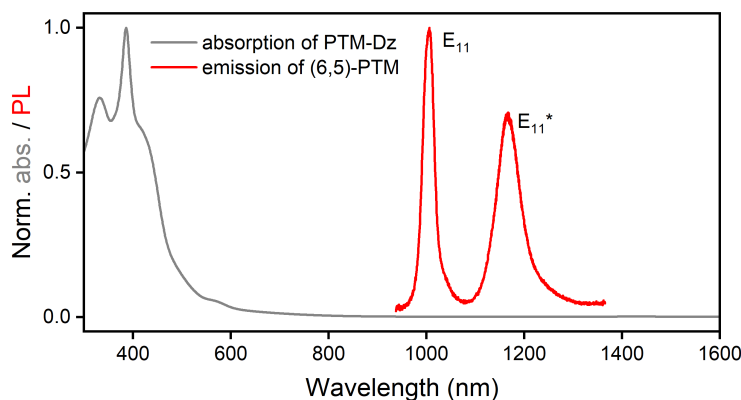


Figure 5.6: Absorption spectrum of PTM-Dz in THF and PL spectrum of PTM-functionalized (6,5) SWNTs in toluene.

First of all, it must be noted that the rate of Förster-²¹⁶ or Dexter-type²¹⁷ energy transfer depends on the overlap between the emission spectrum of the donor (here, the sp^3 defect) and the absorption spectrum of the acceptor (the PTM). While the emission spectrum of PTM-functionalized (6,5) SWNTs is easily accessible, the absorption of the attached PTM chromophores with a concentration on the order of nmol L^{-1} is below the detection limit of a standard absorption measurement. Note that the absorption of the attached PTM group itself and not the E_{11}^* transition would have to be probed in this case. For that reason, the absorption spectrum of the molecular PTM-Dz precursor was measured and used as an approximation to the absorption spectrum of the attached PTM radicals. As expected of PTM derivatives, the spectrum is dominated by a strong absorption band around 385 nm.²¹⁸ From the overlay in Figure 5.6 it is obvious that the spectral overlap between the two partners is negligible and thus, excitation energy transfer should be prohibitively slow and is therefore ruled out.

Although ground state charge transfer was excluded based on the detected changes in PL lifetime, excited state charge transfer in the form of photoinduced electron transfer (PET) is a dynamic quenching mechanism that could contribute to non-radiative decay. Figure 5.7 outlines the PET mechanism as it might proceed in PTM-functionalized sp^3 defects. After exciton trapping at the defect site, an electron is transferred to the PTM radical, thus reducing it to the PTM anion. Subsequently, the electron is

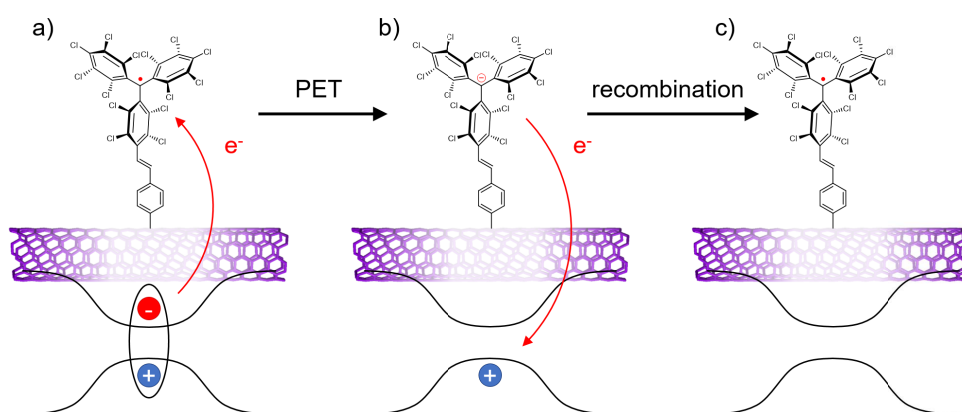


Figure 5.7: Schematic illustration of E_{11}^* PL quenching by photoinduced electron transfer (PET). (a) An electron is transferred from the defect-localized excited state to the PTM radical, thus reducing the latter to the PTM anion. (b) Subsequently, the electron is back-transferred to the valence band of the SWNT, where it recombines with a hole to non-radiatively return the sp^3 defect to its ground state (c).

back-transferred to the defect where charge recombination recovers the ground state of the sp^3 defect. In order to evaluate the driving force for the initial electron transfer from the SWNT/defect (donor D) to the PTM radical (acceptor A), as depicted in Figure 5.7a, the Gibbs free energy for PET may be computed according to²¹⁹

$$\Delta G_{PET} = eE_{red} (D^+ / D) - eE_{red} (A / A^-) - \Delta G_{00} - \frac{e^2}{4\pi\epsilon_r\epsilon_0 d} \quad (5.1)$$

where E_{red} is the reduction potential, ΔG_{00} the optical transition energy and the Coulomb attraction stabilizing the created ion pair is estimated to be about 0.5 eV for the relative permittivity of toluene ($\epsilon_r = 2.38$) and a distance $d \sim 1.2$ nm between the central carbon atom of PTM and the SWNT surface. Using the redox potentials reported by Shiraishi *et al.*²²⁰ and Souto *et al.*²²¹ as well as the PL transition energies determined in this work, PET from both pristine and sp^3 functionalized regions of a (6,5) SWNT to the PTM is found to be highly favorable²²² as indicated by a large negative ΔG_{PET} in Table 5.2. However, as the rate of electron transfer reactions drops exponentially on the length scale of 0.1 nm,²²³ only defect-localized excitons are sufficiently close to PTM radicals to be quenched by PET, which could explain why E_{11} emission is insensitive to the presence of the radical.

While PTM radicals could participate in a PET process because of their electron-poor character,¹⁷⁰ this pathway does not rely on the net spin of the functional group and

Table 5.2: Oxidation (E_{ox}) and reduction potentials (E_{red}) for pristine and sp^3 functionalized (6,5) SWNTs and PTM radicals. Electrochemical data for ArBr-functionalized (6,5) SWNTs was used as an approximation to that of PTM-functionalized (6,5) SWNTs, which is justified by their very similar optical trap depths. ΔG_{00} corresponds to the E_{11} and E_{11}^* PL transition energies, respectively. ΔG_{PET} refers to the oxidation of the SWNT/defect with simultaneous reduction of the PTM radical and includes a Coulomb term of -0.5 eV.

| species | E_{ox} (V) | E_{red} (V) | ΔG_{00} (eV) | ΔG_{PET} (eV) |
|---------------------|--------------|---------------|----------------------|-----------------------|
| (6,5) pristine | 0.615 | -0.420 | 1.24 | -2.17 |
| (6,5) sp^3 defect | 0.584 | -0.398 | 1.06 | -1.95 |
| PTM | 1.61 | -0.19 | - | - |

may be equally efficient with certain closed-shell substituents. In contrast to that, the radical could also interact with the exciton *via* spin exchange.

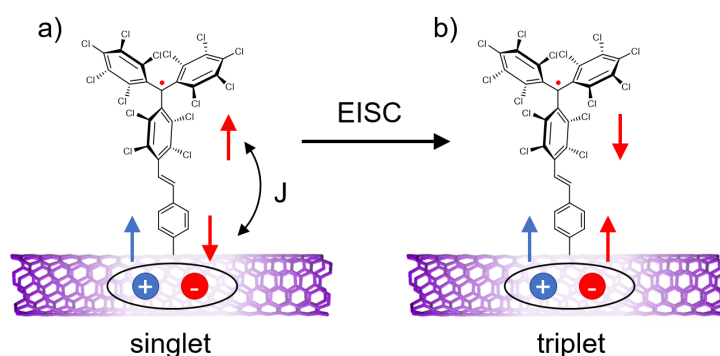


Figure 5.8: Schematic illustration of radical-enhanced intersystem crossing (EISC) in PTM-substituted sp^3 defects. (a) The electronic exchange interaction (J) between the radical spin and a trapped singlet exciton promotes a spin-flip that yields a triplet exciton (b).

Within this framework, the electronic exchange coupling (J) between the unpaired spin of the radical and the photoexcited electron-hole pair on the nanotube acts as a first-order perturbation that facilitates spin-flips of the involved charge carriers and thus speeds up intersystem crossing as sketched in Figure 5.8.²²⁴ Previously, such radical-enhanced intersystem crossing (EISC) was observed for a range of organic chromophores tethered to stable organic radicals.^{225–227} The strength of this interaction strongly increases with wavefunction overlap between the exciton and the singly-occupied molecular orbital (SOMO) on the radical.²²⁵ Furthermore, a higher EISC rate is expected for smaller singlet-triplet energy gaps.²²⁶ This may be understood from a simple perturbation theory treatment, which predicts the wavefunction mixing coefficient to be inversely proportional to the energy gap between the mixed states.

For radical-chromophore distances of around 1 nm and singlet-triplet splittings of a few 100 meV, EISC lifetimes of 1-100 ps were reported.^{225–228}

Given that the PTM-SWNT distance amounts to ~ 1.2 nm and the singlet-triplet splitting of E_{11} excitons in (6,5) SWNTs was predicted to be in the range of 50-100 meV,⁸⁹ fast EISC may be expected for excitons localized at PTM defects. As a result, excited state population could be transferred from the bright singlet to a dark triplet state, thus quenching E_{11}^* PL. Mobile E_{11} excitons, on the other hand, are on average too far away to couple to the radical spin.

In summary, both PET and EISC are plausible mechanisms for the quenching of defect-localized excitons. While both processes should reduce the E_{11}^* emission intensity, each pathway is expected to modify the decay dynamics of the trapped exciton in a distinct way. Therefore, a deeper analysis of the PTM radical-induced changes in E_{11}^* PL decay with respect to the established model for sp^3 defects with closed-shell substituents will be conducted in the next Section.

5.6 Model of exciton dynamics

The model of exciton dynamics at PTM defects presented in this Section is guided by three main assumptions: (i) The room-temperature exciton dynamics in sp^3 defects with closed-shell substituents follow the model by Hartmann *et al.*¹⁰⁴ and He *et al.*,¹⁰⁵ which was described in Section 2.2.3. It must be emphasized that any information regarding the role of the PTM radical that is derived in this Section only applies as long as this model is a valid description of the closed-shell case. (ii) Only PET and EISC are considered as potential quenching mechanisms. (iii) The exciton dynamics in PTM-substituted sp^3 defects are considered to be similar to those of the closed-shell reference system, but subject to either PET or EISC or a combination of both. This notion is corroborated by the relatively weak PL quenching (by a factor of ~ 2.5) and the observation of bi-exponential E_{11}^* PL decay with components of $\tau_l \sim 100$ ps and $\tau_s \sim 10$ ps for both open- and closed-shell aryl substituents.

Figure 5.9a depicts the model for exciton dynamics in common sp^3 defects with closed-shell substituents as studied in Chapter 4. The bright E_{11}^* (B) state is assumed to be the lowest energy singlet within the manifold of defect-localized excitons and

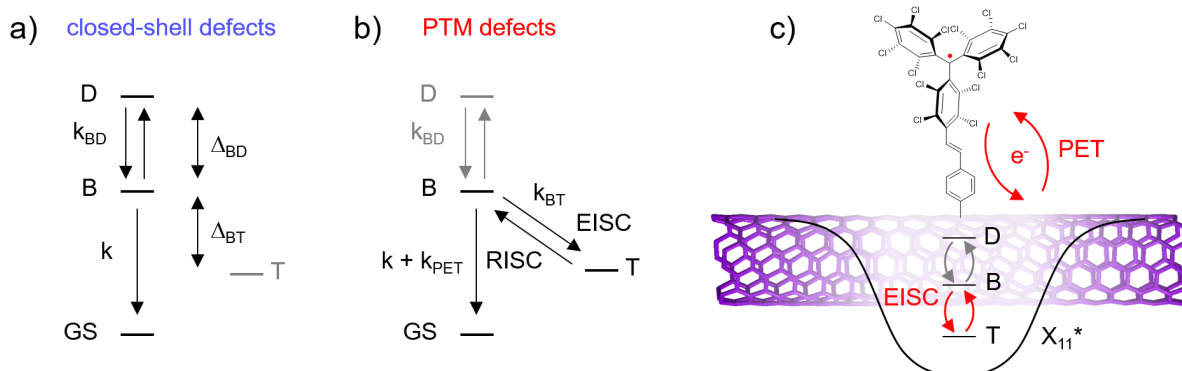


Figure 5.9: Model of exciton dynamics in sp^3 defects with (a) closed-shell and (b) PTM radical substituents. The energy level diagram includes the ground state (GS), the defect-localized bright (B) singlet exciton (giving rise to E_{11}^* emission), a localized dark (D) singlet exciton as well as a triplet (T) exciton, which could be either localized or mobile. The energy gaps between these states are defined by Δ_{BD} and Δ_{BT} . The indicated rate constants pertain to the following processes: k - exciton recombination through radiative and non-radiative channels; k_{PET} - non-radiative recombination due to photoinduced electron transfer; k_{EISC} - radical-enhanced intersystem crossing from the B to the T state; k_{RISC} - thermally activated reverse intersystem crossing from the T to the B state; k_{BD} - equilibration of B and D state populations; k_{BT} - equilibration of B and T state populations. (c) Graphical illustration of PET and EISC as the PL quenching mechanism in PTM-functionalized (6,5) SWNTs. States with low occupation probability and processes that are not competitive are indicated by gray color.

separated from a dark (D) singlet state by Δ_{BD} , which was estimated¹²⁴ to be a few meV. Coupling to the triplet manifold is considered inefficient because of weak spin-orbit interactions²²⁹ and low quantum yields of triplet formation reported for E_{11} excitons ($\sim 5\%$).²³⁰

After exciton trapping at the defect site, the excited state population undergoes a fast redistribution (with rate k_{BD}) among bright and dark states until an equilibrium defined by the Boltzmann occupation probability is reached. On a longer time scale, the trapped excitons recombine through radiative and non-radiative channels (with cumulative rate k) while the ratio of the B and D state populations remains constant. Within this framework, the experimentally measured long and short lifetime components are given by $\tau_l^{-1} = k$ and $\tau_s^{-1} = k_{BD} + k$, respectively.

To adapt this model to PTM radical-substituted defects, the effect of PET and EISC on the dynamics in Figure 5.9a must be evaluated. From the discussion in Section 5.5 it becomes clear that PET is a non-radiative recombination process that leads to irreversible loss of excited state population. The case of EISC is more complex as its

characteristics depend on the energy gap Δ_{BT} between the bright singlet and the triplet (T) state.

If $\Delta_{BT} \gg 25$ meV, EISC depletes the B state population irreversibly at room temperature since thermally activated reverse intersystem crossing (RISC) is ruled out. Otherwise, however, RISC enables reversible population exchange between the B and the T state. In this scenario, the triplet state drains population from the bright state, but does not speed up exciton recombination. On the basis of the low-temperature TCSPC results that will be presented in Section 5.7, it may be assumed that the T state is energetically below the B state. The magnitude of Δ_{BT} will be estimated later in this Section based on this condition.

Despite the complexity of the system, there are simple ways to separate and identify the contributions of enhanced non-radiative recombination, as expected in the case of PET or irreversible EISC, and reduced bright state population, as expected in the presence of reversible EISC. As recombination can occur at any time after exciton trapping, a radical-associated recombination channel with hypothetical rate k_Q should speed up τ_l^{-1} and τ_s^{-1} to an equal degree, *i.e.*,

$$\tau_l^{-1}(\text{PTM}) - \tau_l^{-1}(\text{closed-shell}) = \tau_s^{-1}(\text{PTM}) - \tau_s^{-1}(\text{closed-shell}) = k_Q \quad (5.2)$$

must be satisfied. However, upon evaluating these terms for the E_{11}^* lifetime data in Table 5.1, it turns out that $\tau_l^{-1}(\text{PTM}) - \tau_l^{-1}(\text{PTM irradi.}) = 2.1 \times 10^9 \text{s}^{-1}$, whereas $\tau_s^{-1}(\text{PTM}) - \tau_s^{-1}(\text{PTM irradi.}) = 1.9 \times 10^{10} \text{s}^{-1}$. Hence, the responses of τ_l^{-1} and τ_s^{-1} to the presence of the PTM radical differ by almost an order of magnitude. Enhanced non-radiative recombination alone, *i.e.*, pure PET or irreversible EISC, cannot account for the radical-induced changes in PL lifetime. In fact, the only way to rationalize the observed PL decay behavior with the assumptions stated above is through a combination of PET and reversible EISC, in which PET speeds up exciton recombination while reversible EISC leads to partial transfer of exciton population from the bright state to a triplet state. Within this kinetic model, which is illustrated in Figure 5.9b, the long and short decay components take on the forms $\tau_l^{-1} = k + k_{PET}$ and $\tau_s^{-1} = k_{BT} + k + k_{PET}$, respectively.

The model described in Figure 5.9b is further supported by a quantitative analysis of the PL lifetime data in Table 5.1, which affords reasonable values for all involved physical parameters. First of all, a PET rate of $(500 \text{ ps})^{-1}$ is computed, which could be explained by the trade-off between a highly favorable ΔG_{PET} and the relatively large distance of about 1.2 nm between the PTM radical and the nanotube. Since PET only changes the recombination rate but not the amplitudes of the bi-exponential decay, the Stern-Volmer equation²¹⁶ can be used to obtain the quenching factor purely due to PET,

$$QF_{PET} = 1 + \frac{k_{PET}}{\tau_{amp-av}^{-1}(\text{PTM irradi.})} = 1 + \frac{(500 \text{ ps})^{-1}}{(121 \text{ ps})^{-1}} = 1.24 \quad (5.3)$$

which represents the ratio of amplitude-averaged lifetimes τ (closed-shell)/ τ (PTM). Note that the same ratio applies to the PL intensities if the radiative lifetime is constant, as in this case.

Table 5.3: Physical parameters extracted for PTM radical-substituted aryl defects with respect to a closed-shell reference of UV-irradiated PTM defects as characterized in Table 5.1. $\Delta_{BD} = 9 \text{ meV}$ as reported by Kim *et al.*¹²⁴ for E_{11}^* defects (6,5) SWNTs was assumed in the calculations. $\Delta_{BT}^{(1T)}$ was computed under the assumption that the entire triplet exciton population resides in a single state.

| k_{PET} | k_{BT} | $\Delta_{BT}^{(1T)}$ | QF_{PET} | QF_{EISC} | QF_{tot} |
|-------------------------|------------------------|----------------------|------------|-------------|------------|
| $(500 \text{ ps})^{-1}$ | $(37 \text{ ps})^{-1}$ | 38 meV | 1.24 | 1.88 | 2.37 |

The time scale for population redistribution among the B and T state is found to be $k_{BT} = (37 \text{ ps})^{-1}$ in good agreement with EISC rates reported for organic radical-chromophore dyads separated by $\sim 1 \text{ nm}$.²²⁵⁻²²⁸ As k_{BT} exceeds $k_{BD} = (91 \text{ ps})^{-1}$ extracted for the closed-shell reference of UV-irradiated PTM defects and the T state is lower in energy than the D state, it may be concluded that the T state becomes the main reservoir that accepts population from the bright state.

As noted by He *et al.*,¹⁰⁵ the normalized amplitude of the slow decay component should be proportional to the equilibrium population of the bright state. Hence, the quenching due to EISC-mediated population transfer is simply given by

$$QF_{EISC} = \frac{A_l(\text{PTM irradi.})}{A_l(\text{PTM})} = \frac{30\%}{16\%} = 1.88 \quad (5.4)$$

and as the product $QF_{\text{PET}} \times QF_{\text{EISC}}$ matches the total quenching factor (QF_{tot}) determined from the measured E_{11}^* lifetimes, the assumption of combined PET and EISC results in a consistent model of PL quenching (Figure 5.9c).

Finally, since the equilibrium populations of the B, D and T states should be defined by the Boltzmann occupation probability and $\Delta_{BD} \sim 9$ meV was previously determined for E_{11}^* defects (6,5) SWNTs by Kim *et al.*,¹²⁴ the remaining parameter, Δ_{BT} , can be estimated. If it is assumed that the entire triplet population resides in a single state, $\Delta_{BT} = 38$ meV is obtained. However, quantum chemical calculations predict several triplet states within a few 10 meV of the bright E_{11}^* state.⁹¹ Therefore, $\Delta_{BT} = 38$ meV should be considered as an upper bound to the real singlet-triplet energy gap at E_{11}^* defects in (6,5) SWNTs.

To sum up, the PL quenching in PTM radical-tailored sp^3 defects can be adequately modeled by a combination of PET and EISC-driven exciton population transfer to dark triplet states. As $QF_{\text{EISC}} > QF_{\text{PET}}$, it may be concluded that quenching is dominated by the EISC process.

5.7 PL at low temperature and in high magnetic fields

As PL quenching in PTM-substituted sp^3 defects seems to be primarily caused by population transfer to dark triplet states, knowledge about their energy with respect to the bright E_{11}^* exciton would be highly desirable. Therefore, PL spectroscopy was performed on individual PTM-functionalized nanotubes at low temperature (4 K) and in high magnetic fields (up to 9 T). At cryogenic temperatures, population transfer to higher-energy states is ruled out due to insufficient thermal energy (~ 0.3 meV at 4 K). Hence, the observation of fast EISC at low temperatures would point toward the involved triplet state being energetically below the bright E_{11}^* exciton. Moreover, as lattice vibrations are strongly suppressed under these conditions, the PL linewidths are narrowed down to the level of around 1 meV. Thus, potential satellite peaks brightened under the influence of an applied magnetic field become resolvable.⁸⁵

As nanotubes carrying a single sp^3 defect were desired for these experiments, (6,5) SWNTs were reacted with a low concentration of PTM-Dz ($C_{Dz} = 7 \mu\text{mol L}^{-1}$, compare Section 3.2.2). Subsequently, these PTM-functionalized SWNTs were embedded in a

polystyrene matrix to reduce spectral diffusion and enhance the PL intensity.^{231,232} A confocal scanning PL map (Figure 5.10a) confirmed that the nanotubes were spatially separated and could be probed individually. In agreement with previous work,¹²⁸ the low-temperature PL spectra in Figure 5.10b show an inhomogeneous distribution of spectrally-narrow signals within the E_{11}^* band that are attributable to individual defects in distinct dielectric environments.^{14,127} As characteristic of the cryogenic PL spectra of polymer-wrapped SWNTs,²³³ each peak is accompanied by a weak phonon sideband red-shifted by 2-3 meV.

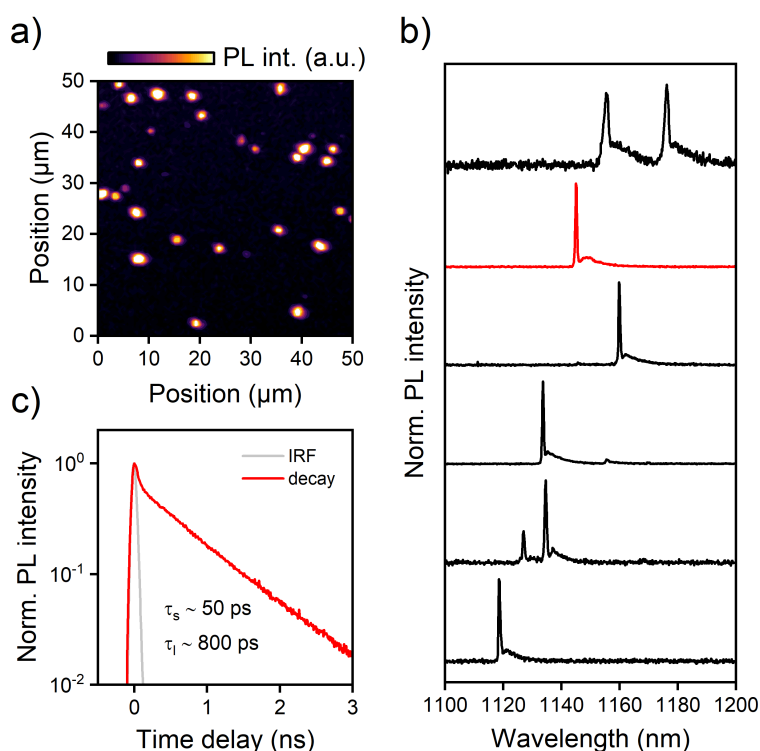


Figure 5.10: (a) Confocal raster-scanned PL map (acquired at room temperature) of individual PTM-functionalized (6,5) SWNTs in a polystyrene matrix. Excitation conditions: 785 nm, cw, 10 μ W, linearly polarized. (b) PL spectra of individual PTM-functionalized nanotubes measured at 4 K. Excitation conditions: 995 nm, cw, 6 μ W. The spectrum highlighted in red indicates the nanotube selected for the time-resolved measurement. (c) E_{11}^* PL decay of a single sp^3 defect recorded at 4 K. Excitation conditions: 995 nm, pulsed, 3 μ W.

Figure 5.10c shows the E_{11}^* PL decay of a single sp^3 defect corresponding to the PL spectrum highlighted in Figure 5.10b. The PL decay is bi-exponential with an unusually fast component with large amplitude ($\tau_s = 50$ ps, $A_s = 60\%$) and a slow component with $\tau_l = 800$ ps that falls in the range of decay times commonly observed for sp^3 defects with closed-shell functional groups.^{123,124} Such a fast decay component is un-

precedented for E_{11}^* emission at low temperature and since multi-exciton effects²³⁴ are ruled out based on the low excitation photon flux (2×10^{14} photons cm^{-2} pulse $^{-1}$),⁹⁶ its origin is likely related to the PTM radical. With a room-temperature rate of $(500 \text{ ps})^{-1}$, PET is clearly too slow to be responsible for this fast decay. On the other hand, the room-temperature time scale for population transfer due to EISC is in excellent agreement with τ_s . For that reason, the fast component is assigned to EISC and it may be concluded that the involved triplet state has a lower energy than the bright E_{11}^* state as was assumed in the model described in the previous Section.

However, as EISC should be irreversible at low temperature, the origin of the slow decay component is not obvious. A possible explanation might be temporary trapping of charge carriers on the PTM group (*e.g.*, following a PET event) aided by the cryogenic temperature and the insulating environment provided by the polystyrene matrix. As a result, the PTM radical would be reduced to its spin-paired anion state, in which EISC is switched-off, thus resulting in a slower decay time. In that case, the histogram in Figure 5.10c would represent a superposition of the histograms expected for the two individual species, *i.e.*, the PTM radical- (τ_s) and the PTM anion-substituted (τ_l) defects.

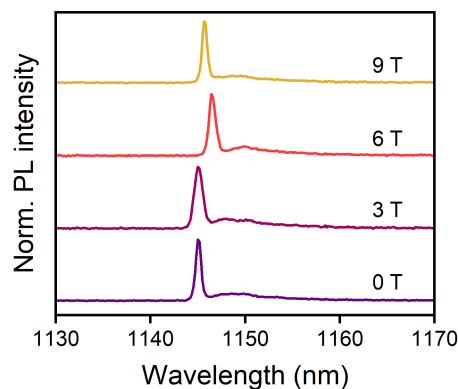


Figure 5.11: PL spectra of an individual PTM-functionalized (6,5) SWNTs for different applied magnetic fields at 4 K. The angle between the nanotube axis and the in-plane magnetic field was 60° . Excitation conditions: 995 nm, cw, 6 μW .

The same PTM-functionalized nanotube was also characterized by recording PL spectra as a function of an applied in-plane magnetic field (Voigt geometry). As evident from Figure 5.11, no field-induced fine structure was detectable within the limitations of spectrometer resolution ($\sim 0.3 \text{ meV}$) and characteristic spectral diffusion ($\sim 2 \text{ meV}$).

This result was corroborated by measurements on eight individual SWNTs with E_{11}^* emission signals in the wavelength range of 1120-1180 nm and different nanotube orientations, some of which were nearly parallel to the applied field.

Recently, Kim *et al.*⁹¹ observed a magnetic field-induced peak splitting in a minority of sp^3 functionalized SWNTs, which the authors explained by the brightening of delocalized E_{11} -associated triplet states through their mixing with the bright E_{11}^* exciton. As this mechanism requires a nearly perfect energy level alignment (\pm a few meV) between the involved singlet and triplet states, the absence of fine structure in the magneto-PL spectra shown in Figure 5.11 is in accordance with the estimate of $\Delta_{BT} = 38$ meV derived in Section 5.6, which should prevent significant field-induced coupling of the B and the T state.

Overall, the low-temperature and magnetic field-dependent PL experiments are in good agreement with the kinetic model developed in the previous Section, albeit further studies are needed to fully understand the E_{11}^* PL decay of PTM defects at low temperature.

5.8 Probing triplet states by EISC

As the interaction between nanotube excitons and radical spins appears to be dominated by radical-enhanced intersystem crossing (EISC), it is worth discussing how this mechanism could be harnessed to gain insights into the elusive triplet exciton manifold of pristine or sp^3 functionalized SWNTs (Figure 5.12).

First of all, it should be noted that EISC is also likely to occur in pristine SWNTs given the small singlet-triplet splitting of 50-100 meV predicted for E_{11} excitons in (6,5) SWNTs.⁸⁹ Since these splittings are still larger than Δ_{BT} estimated in Section 5.6, RISC should be slower than in the case studied here. Hence, EISC might give access to a large population of long-lived triplet states in pristine nanotubes, which could be probed by transient absorption,^{90,94} optically-detected magnetic resonance^{93,230} or PL spectroscopy as demonstrated in this work. In fact, quantifying the RISC rate, *e.g.*, through detection of delayed fluorescence,^{92,230} would be an even more powerful approach as the forward EISC process does not need to directly involve the lowest

energy triplet exciton²²⁶ (T_1) as illustrated in Figure 5.12 using the example of E_{11} excitons.

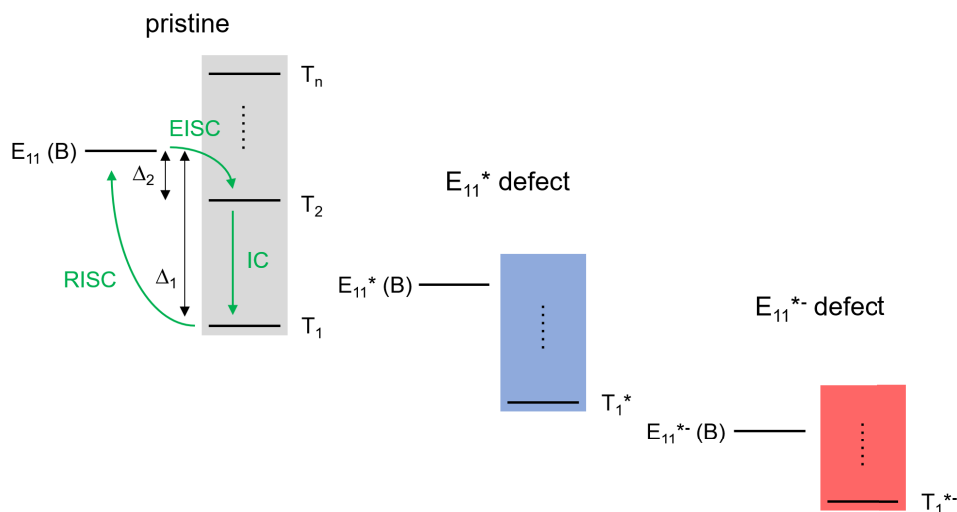


Figure 5.12: Schematic illustration of triplet (T) energy levels with respect to bright (B) excitons of the E_{11} , E_{11}^* and E_{11}^{*-} manifold. Note that the energy level diagram is intended to be purely illustrative and does not represent any experimental or theoretical data. Population transfer mediated by radical-enhanced intersystem crossing (EISC) and its reverse process (RISC) are indicated together with ultrafast internal conversion (IC). As the EISC rate scales with the inverse of the singlet-triplet energy gap (Δ_1 , Δ_2), transfer to higher-lying triplets (*e.g.*, T_2) could be preferred over direct transfer to T_1 in some cases.

In the case of pristine SWNTs, the simplest way to realize EISC would be the addition of stable organic radicals (*e.g.*, the free PTM radical) to a nanotube dispersion. However, in the absence of a covalent linkage, EISC relies on bi-molecular collisions between radicals and mobile excitons on the SWNTs. Hence, to achieve competitive EISC rates of $> (100 \text{ ps})^{-1}$, extremely high radical concentrations of several mol L^{-1} would be required.²¹⁶ An alternative approach could be the covalent attachment of radicals to SWNTs through functionalization chemistry that leaves the sp^2 carbon lattice intact. As shown by Setaro *et al.*,¹⁴² high levels of functionalization are achievable without E_{11} emission quenching or the creation of localized exciton states. Thus, combining this approach with the concept of EISC holds promise for efficient triplet sensitization²³⁵ in quasi-intrinsic carbon nanotubes.

The introduction of radical-substituted sp^3 defects, on the other hand, not only enables the efficient interaction between T excitons and spins but also allows lower-energy (and potentially localized) triplet states to be probed. Comparing the EISC response of such defects to the pristine case might also answer the question whether the

triplet involved in the exciton dynamics of PTM defects belongs to the E_{11} or E_{11}^* manifold. Furthermore, varying the energy of the defect-localized exciton *via* the binding configuration or the aryl substituent could enhance or suppress the coupling of the bright exciton to the various triplet states and thus provide further information about their character.

Overall, the interaction with radical spins is a promising approach to access triplet states in carbon nanotubes and extract information regarding their energies and degree of exciton localization.

5.9 Summary and conclusion

This Chapter described the decoration of purified semiconducting (6,5) SWNTs with stable organic perchlorotriphenylmethyl (PTM) radicals using simple diazonium chemistry. Due to the good solubility of the PTM-tailored diazonium salt in organic solvents, this approach is perfectly suited for the functionalization of polymer-wrapped SWNTs. Upon covalent attachment to the (6,5) SWNT, the unpaired spin remains localized on the PTM moiety and interacts with the nanotube through space. PL spectroscopy shows a quenching of E_{11}^* emission (by a factor of ~ 2.5) while E_{11} PL is not affected, thus demonstrating that the interaction with the radical is short-ranged and therefore limited to defect-localized excitons. The observed radical-induced changes in E_{11}^* decay dynamics can be adequately explained by assuming a partial population transfer from the bright E_{11}^* exciton to a dark triplet state mediated by radical-enhanced intersystem crossing (EISC) and a smaller contribution from a photoinduced electron transfer (PET) process. These findings may provide the starting point for more extensive studies of triplet excitons in carbon nanotubes exploiting the concept of EISC. By choosing a different radical species from the large library of stable organic radicals known today, including, *e.g.*, nitroxides, phenoxyl and verdazyl radicals,^{236,237} it might be possible to suppress photoinduced electron transfer in future studies and thus to achieve purely spin-based interaction with the nanotube exciton.

Chapter 6

Luminescent Defects in SWNT Thin Films

This Chapter discusses the photoluminescence and electroluminescence properties of aryl defects in thin films and devices.

The results presented in Section 6.2 were published* in part in Berger *et al.*, *ACS Nano* **2019**, *13*, 9259-9269.¹⁶⁹ Modified reprints of previously published Figures are presented with permission of the American Chemical Society. The waveguides discussed in Sections 6.3 and 6.4 were fabricated and characterized in collaboration with Jan M. Lüttgens (Heidelberg University). Simon Settele (Heidelberg University) provided a sample of SWNTs that were selectively functionalized with E_{11}^{*-} defects according to a recently developed method.²³⁸ The light-emitting field-effect transistors described in Section 6.5 were fabricated and characterized in collaboration with Nicolas F. Zorn (Heidelberg University).

6.1 Introduction

As emphasized in Chapter 4, polymer-wrapped SWNTs in organic solvents exhibit superior solution-processability and film formation properties compared to surfactant-encapsulated SWNTs in water. Therefore, the protocols for sp^3 functionalization of polymer-wrapped SWNTs developed in this work strongly facilitate the integration of carbon nanotubes with luminescent defects into light-emitting devices and photonic structures. This Chapter demonstrates that deposition methods like aerosol-jet printing or spin-coating, which are well-established for polymer-sorted SWNTs,^{64,171,179} are easily transferable to defect-tailored, polymer-wrapped SWNTs and yield homogeneous and luminescent thin films suitable for device applications.

Nevertheless, it is important to keep in mind that the PL characteristics of carbon nanotubes in thin films can be markedly different from those observed in liquid dispersions, which were covered extensively in Chapters 4 and 5. The properties of nanotubes deposited on substrates are influenced by many factors including the chiral purity of the sample,^{33,93,239} the level of tube bundling,²⁴⁰⁻²⁴³ the dielectric environment^{105,244-247} as well as interactions with the substrate,²⁴⁸ metal electrodes²⁴⁹ or other layers in a device stack. In many cases, the PL properties of nanotubes in thin films are inferior to those in liquid dispersions and show undesired line broadening,^{88,186,232} spectral diffusion^{250,251} and blinking^{123,231} as well as a reduced PLQY.²⁴⁰ These adverse effects

*URL: <https://pubs.acs.org/doi/10.1021/acsnano.9b03792>. Requests related to the reuse of this material should be directed to the American Chemical Society.

can sometimes be alleviated by providing a low-permittivity environment, *e.g.*, by embedding the SWNTs in a polymer matrix^{117,231,232,250,252} or depositing them on top of an atomically-flat insulator.^{251,253} However, in device structures, this approach is often not feasible. For that reason, a detailed understanding of the emission properties of sp^3 functionalized SWNTs in thin films is of high practical importance.

One of the key questions in this respect is whether the PLQY of the defect state decreases to the same degree as that of the intrinsic E_{11} exciton upon depositing the SWNTs as a thin film. Given the stark contrast in non-radiative decay pathways and PL lifetimes of mobile (E_{11}) and trapped (E_{11}^*) excitons,¹⁰⁵ each state might respond differently to the perturbation caused by substrate or intertube interactions. This question is addressed in Section 6.2 for the example of aerosol-jet printed and spin-coated films of pristine and sp^3 functionalized (6,5) SWNTs.

Since the emission generated in bare films of randomly oriented SWNTs is not directional, it is hardly useful for applications. Thus, Section 6.3 deals with sp^3 functionalized (6,5) SWNTs that were doped into a smooth polymer layer waveguiding the emitted PL to the edge of a solid substrate, from which it is out-coupled in a controlled fashion as is required for instance in luminescent solar concentrators.^{149–151}

Furthermore, the employed waveguide architecture is a commonly used layout for the measurement of the optical gain or loss coefficient of a material.¹⁵⁷ Although there is a report of optical gain at the E_{11} transition of pristine SWNTs,¹⁵² the absence of such a signature in other studies of the high excitation density regime calls these results into question.^{254,255} The main obstacle to achieving optical gain in pristine SWNTs is considered to be exciton-exciton annihilation (EEA), *i.e.*, the fast Auger quenching of E_{11} excitons upon diffusive encounter, which prevents sufficiently high exciton densities from being reached.^{256–259} In addition, low PLQYs²⁶⁰ (on the order of 0.1 % in films) and strong self-absorption owing to the small E_{11} Stokes shift⁹⁷ (a few meV) limit the light output of pristine SWNTs in thin films.

For luminescent sp^3 defects some of these issues are substantially improved and hence, optical gain appears more likely to be realized at the defect-associated E_{11}^* transition than at the intrinsic E_{11} transition. In particular, the self-absorption of E_{11}^* emission is negligible,¹⁷⁵ the PLQYs in μm -long (6,5) SWNTs are enhanced by a factor of 2 and significant state-filling is observed at moderately low pump powers.¹²⁶ On the other

hand, there are indications that mobile excitons can also quench localized excitons in an EEA process upon diffusive collision with the defect site.²³⁴ To search for optical gain with sp^3 defects, the emission from waveguide-incorporated functionalized SWNTs was studied in the high exciton density regime, as discussed in Section 6.4.

Finally, the recent demonstration of electroluminescence (EL) from sp^3 defects under impact excitation in a two-terminal device²⁶¹ raises the questions whether EL can also be generated through carrier recombination under ambipolar conditions and how the presence of sp^3 defects affects charge transport in the operating device. To address these points, random networks of sp^3 functionalized SWNTs were integrated into light-emitting field-effect transistors and their charge transport and electroluminescence characteristics studied, as described in Section 6.5.

6.2 Emission efficiency in thin films

One of the simplest ways to compare the emission efficiencies of pristine and sp^3 functionalized SWNTs in thin films is to measure the PL intensity emitted from equally thick films of the two materials. Here, an aerosol-jet printer¹⁷¹ (see Section 3.3.2) was used to deposit pristine and 4-bromophenyl-functionalized (6,5) SWNTs from concentrated inks onto glass substrates. Functionalization was carried out at a Br-Dz concentration of 0.37 mmol L^{-1} so as to maximize the E_{11}^* and total PLQY as described in Section 4.4. At this degree of functionalization, each nanotube is expected to bear only about 7 – 9 defects per micrometer tube length and thus, the colloidal stability and viscosity of the dispersion should be very similar to that of pristine (6,5) SWNTs. Indeed, both nanotube inks could be printed under the same conditions and the film thickness was tuned *via* the number of printing cycles.

Figure 6.1a shows a brightfield (BF) optical micrograph of printed films that are visible with the bare eye. Scanning the films with a 532 nm laser and recording the G^+ mode Raman intensity (Figure 6.1b) confirmed that the two films indeed contained very similar amounts of nanotubes.¹⁸⁷ Turning to PL characterization, the films were homogeneously illuminated with the expanded beam of a 640 nm cw laser and the PL within the InGaAs detection window (900-1600 nm) was imaged by a 2D array detector (Figure 6.1c). Clearly, the film of sp^3 functionalized SWNTs is significantly brighter

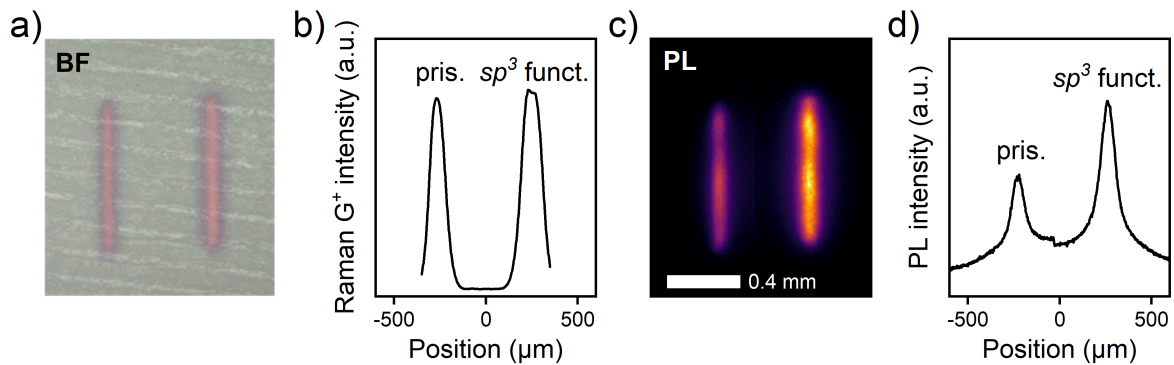


Figure 6.1: (a) Brightfield optical micrograph of printed films (left: pristine, right: sp^3 functionalized SWNTs). (b) Raman G^+ mode intensity profile across the printed films and averaged along each stripe. (c) PL micrographs recorded under cw excitation at 640 nm. Note that the raw PL intensity at each pixel was corrected for the wavelength-dependent sensitivity of the InGaAs detector taking into account the emission spectra of the respective nanotube samples. (d) Spectrally-integrated PL intensity profile across the printed films and averaged along each stripe.

than that of pristine SWNTs, thus reflecting the higher PLQY of luminescent defects. Averaging the PL intensity along each stripe (Figure 6.1d) reveals that the total PL intensity of the film of functionalized SWNTs is about 1.7-fold higher than that of the reference and hence the brightening in the film state closely matches that observed in dispersion (Section 4.4).

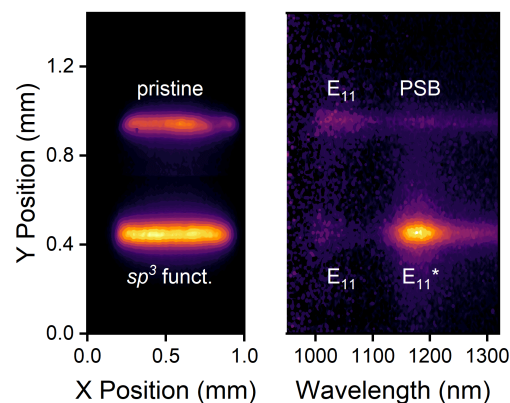


Figure 6.2: Real-space and hyperspectral image of printed films of pristine and sp^3 functionalized (6,5) SWNTs under cw excitation at 640 nm.

In addition, hyperspectral imaging of the stripes (see Figure 6.2) confirmed that the bright PL of the defect-tailored film arises from intense E_{11}^* emission. The spectra show a weak and asymmetric E_{11} feature that suffers from strong self-absorption in the

optically-dense films. In contrast to that, the E_{11}^* emission is nearly free of reabsorption since the E_{11}^* absorbance amounts to only a few percent of that of the E_{11} transition. A more direct way to evaluate the defect-induced brightening in the film state is by measurement of the absolute PLQY using an integrating sphere as outlined in Section 3.4.4.^{20,172} However, this approach requires homogeneous, large-area films and is further complicated by the weak PL signal of deposited nanotubes. To enable a reproducible measurement, pristine and functionalized (6,5) SWNTs were spin-coated from toluene dispersions onto glass substrates with dimensions of 1 cm². Care was taken to keep the optical density of the layers low and thus avoid reabsorption.^{173,262}

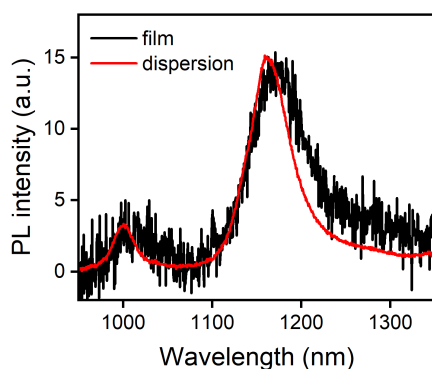


Figure 6.3: PL spectra of 4-bromophenyl-functionalized (6,5) SWNTs measured on a toluene dispersion and a film on glass inside an integrating sphere under excitation at 575 nm.

Table 6.1: E_{11} (900-1080 nm), E_{11}^* (1080-1365 nm, including a small contribution from the E_{11}^{*-} band) and total PLQY of 4-bromophenyl-functionalized (6,5) SWNTs when dispersed in toluene or deposited as a thin film on glass.

| Sample | E_{11} PLQY (%) | E_{11}^* PLQY (%) | total PLQY (%) |
|------------|-------------------|---------------------|----------------|
| dispersion | 0.25 | 2.90 | 3.15 |
| film | 0.03 | 0.28 | 0.31 |

Figure 6.3 compares the PL spectra of 4-bromophenyl-functionalized (6,5) SWNTs in dispersion and in the film as measured inside an integrating sphere. Strikingly, the E_{11}^*/E_{11} PL intensity ratio in dispersion and in the film are essentially identical within the precision of the signal-to-noise ratio. Hence, the E_{11} and E_{11}^* PLQYs are reduced by the same factor upon deposition on glass. Table 6.1 lists the extracted spectrally-resolved and total PLQYs under both conditions. The respective PLQYs are about a factor of 10 lower in the film than in dispersion.

A complementary way to study the PL quenching in nanotube films is by measuring the PL lifetime. Since the E_{11} PL decay is too fast to be resolved using the TCSPC setup used in this work, only the E_{11}^* PL lifetime can be evaluated here. Figure 6.4 shows the E_{11}^* PL decay of the functionalized SWNTs for a dispersion and a drop-cast film on glass. Evidently, the PL lifetime is dramatically reduced upon nanotube deposition, which indicates enhanced non-radiative decay.

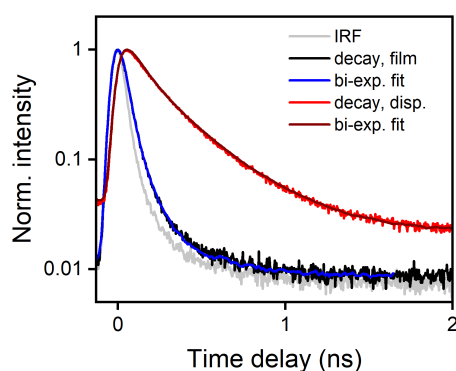


Figure 6.4: E_{11}^* PL decay of 4-bromophenyl-functionalized (6,5) SWNTs measured at an emission wavelength of 1165 nm for a toluene dispersion (red) and a drop-cast film on glass (black). Decay traces are shown together with bi-exponential fits to the data accounting for the instrument response function (IRF).

Although the corresponding data for the E_{11} decay is not available, the fact that the E_{11} and E_{11}^* PLQYs are reduced by the same factor hints toward this non-radiative relaxation being equally efficient for mobile and localized excitons. Since this condition rules out any diffusion-based mechanisms²⁴⁰ and bundling with metallic or large-diameter semiconducting SWNTs is unlikely given the high purity of the samples, the origin of PL quenching in monochiral nanotube films might be increased dielectric screening.^{244,245} This effect should be particularly strong for those nanotubes that are in direct contact with the polar glass substrate.^{118,248} Previously, the PLQY of pristine SWNTs was found to be substantially lower in solvents with high dielectric permittivity, in particular water.²⁴⁴ Additionally, the ratio of E_{11} to E_{11}^* PL intensity was reported to be nearly independent of solvent permittivity¹⁰⁵ thus demonstrating that mobile and localized excitons respond similarly to dielectric screening. As proposed by Larsen *et al.*, increased screening of the electron-hole Coulomb interaction might suppress the radiative recombination of excitons in favor of non-radiative recombination of

free charge carriers.²⁴⁴ Beyond that, the exposure of nanotube surface to water and oxygen in films under ambient conditions could p-dope the nanotubes, thus leading to Auger quenching of excitons.^{118,263} Only very low charge carrier concentrations are required for efficient PL quenching and therefore, such doping levels may not result in significant trion emission.^{163,264}

Table 6.2: Long and short lifetime components (τ_l , τ_s) with corresponding amplitudes (A_l , A_s) and amplitude-averaged lifetimes (τ_{amp-av}) of the E_{11}^* PL decay in 4-bromophenyl-functionalized (6,5) SWNTs when dispersed in toluene or deposited as a thin film on glass.

| Sample | τ_l (ps) | A_l (%) | τ_s (ps) | A_s (%) | τ_{amp-av} (ps) |
|------------|---------------|-----------|---------------|-----------|----------------------|
| dispersion | 262 | 21 | 78 | 79 | 117 |
| film | 66 | 5 | 17 | 95 | 20 |

Bi-exponential fits to the decay traces reveal that the amplitude-averaged E_{11}^* lifetime (see Table 6.2) drops by a factor of 6. Hence, the dynamic quenching cannot fully account for the 10-fold reduction of PLQY. Of course, film morphology and thus, the dielectric environment, may differ between the spin-coated and drop-cast films that were used for the PLQY and TCSPC experiments, respectively. Nevertheless, the mismatch of PL quenching and lifetime shortening may point toward inhomogeneous contributions to the quenching. For instance, if the PLQY of nanotubes directly interacting with the substrate was vanishingly small, they would not contribute to the time-resolved PL experiment at all, whereas nanotubes within the bulk of the film could be quenched to a lesser extent in agreement with the 6-fold shortening of PL lifetime.

In summary, the PLQYs of the E_{11} and the E_{11}^* state drop by roughly the same factor upon depositing the functionalized nanotubes onto glass substrates. Thus, the defect-induced PL enhancement is retained in thin films, but it is not larger than in dispersion. Therefore, future studies should address the role of the dielectric environment on the defect state PLQY and search for suitable protective layers with low dielectric permittivity.

6.3 Waveguide design and characterization

This Section describes the integration of sp^3 functionalized (6,5) SWNTs into polymer waveguides, which not only results in confined propagation of the emitted PL, but also provides the basis for the investigation of potential optical gain and loss processes in luminescent sp^3 defects in Section 6.4.

Figure 6.5a illustrates the structure of the fabricated samples (compare Section 3.3.3), in which defect-tailored SWNTs are embedded in a layer of polystyrene that serves as the core of a planar dielectric waveguide. While the polystyrene/air interface already provides a high refractive index contrast, magnesium fluoride substrates ($n = 1.37$ at $\lambda = 1200$ nm) were chosen instead of glass substrates ($n = 1.50$) to enhance the refractive index contrast at the bottom interface. This approach strongly reduces the minimum thickness of the nanotube/polymer layer required for waveguiding (cut-off thickness); from 485 nm for glass to 224 nm for magnesium fluoride substrates at $\lambda = 1200$ nm. As the nanotube/polymer blend was deposited by spin-coating to produce a smooth layer with low scattering losses, a lower cut-off thickness enabled higher spin speeds and thus improved film homogeneity and waveguide quality.

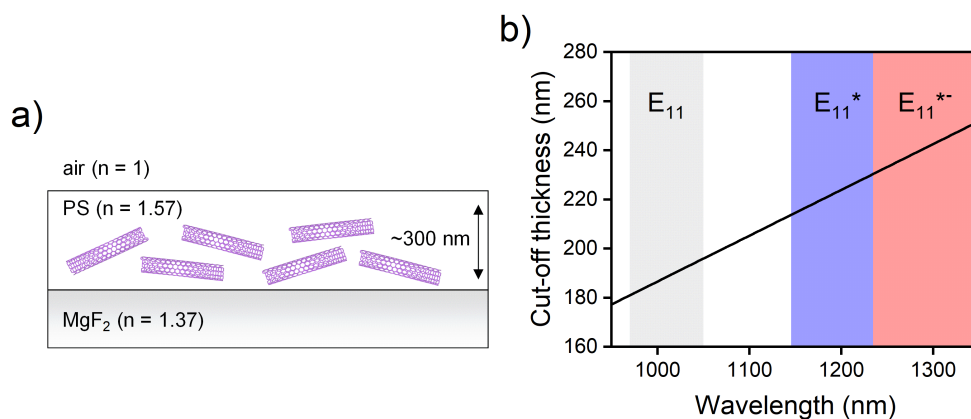


Figure 6.5: (a) Schematic structure of the fabricated planar dielectric waveguides. (b) Cut-off thickness of the polymer/SWNT layer for waveguiding in the fundamental TE mode at a given wavelength. Shading indicates the spectral bands of E_{11} (gray), E_{11}^* (blue) and E_{11}^{*-} emission (red).

Figure 6.5b shows the calculated cut-off thickness (given by Equation 2.10) for waveguiding in the fundamental TE mode of the waveguide structure shown in Figure 6.5a. Since the waveguides studied in this work have a typical core thickness of 300 nm,

they support light propagation across the full spectral range of emission from functionalized (6,5) SWNTs including the defect-associated E_{11}^* and E_{11}^{*-} bands. It should be mentioned that tuning the film thickness below cut-off serves the purpose of a spectral short-pass filter. In this way, the E_{11}^{*-} contribution could be rejected in some applications to narrow down the emission spectrum while transmitting E_{11}^* PL.

The waveguides were characterized in a setup (see Section 3.4.5) that enabled excitation with a line laser from the front, while the waveguided emission was detected from the edge of the substrate, *i.e.*, orthogonal to the excitation beam path. To this end, the nanotube/polymer-coated substrate was cleaved to afford a clean edge for characterization.

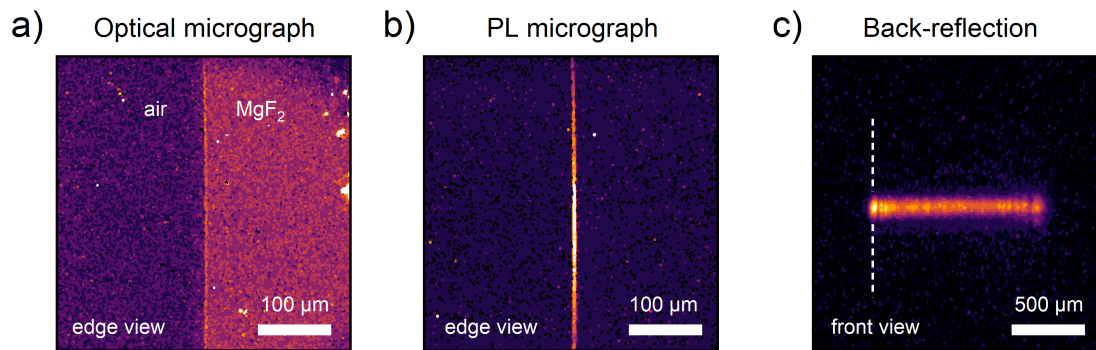


Figure 6.6: (a) Optical micrograph of the substrate edge acquired through the collection objective under lamp illumination. (b) PL micrograph of the same spot recorded under laser excitation. (c) Back-reflection of the laser line imaged *via* a beamsplitter. The white dashed line indicates the location of the substrate edge. Note that laser scattering on the edge gives rise to brighter back-reflection.

Figure 6.6a shows an optical micrograph of the substrate edge viewed through the collection objective under lamp illumination. Imaging confirmed the high quality of the exposed edge of the waveguide and ensured that the objective was precisely focused. When the lamp was switched off and the SWNTs were instead excited with a line laser from the front, their PL was waveguided to the substrate edge, from where it was collected as shown in Figure 6.6b. The observed bright emission zone had a FWHM of $3\ \mu\text{m}$ and gave a nearly diffraction-limited PL image of the $300\ \text{nm}$ -thick waveguide core. In the dimension parallel to the substrate surface, the width of the emission zone was approximately equal to the width of the exciting laser line ($200\text{--}250\ \mu\text{m}$). In order

to determine the size of the laser line directly on the sample surface, a beamsplitter was inserted to image the laser back-reflection onto the detector (Figure 6.6c). Note that to be able to vary the laser stripe length, the sample edge was positioned directly on the optical axis and therefore only half of the generated laser line was projected onto the sample. The excited area on the sample was typically 1.3-1.4 mm long and 200-250 μm wide and featured a homogeneous excitation density profile as confirmed by Figure 6.6c.

As a measure of waveguide quality, the optical losses were quantified in a shifting excitation spot (SES) experiment.^{152,157,174} Within this framework, the PL intensity I_{es} generated at a small excitation spot is attenuated as the light travels the distance z toward the substrate edge and the PL intensity I_{oc} that is out-coupled from the edge varies according to¹⁵²

$$I_{oc} \propto I_{es} \exp(-\gamma z) \quad (6.1)$$

where γ denotes the loss coefficient. To realize this experiment in the setup described above, the laser line was constrained to a total length of about 1.1 mm with an adjustable mechanical slit. Subsequently, the substrate and the objective were shifted in small steps orthogonal to the excitation beam such that the laser line moved deeper into the sample while the collection objective remained focused onto the edge. Figure 6.7a illustrates the procedure with intensity profiles extracted from images corresponding to the starting and the end point of the experiment, respectively. While lamp illumination revealed the position of the sample edge, the laser back-reflection indicated the stripe length projected onto the sample. At the beginning, roughly half of the laser line struck the sample. Upon moving the sample, the stripe length, *i.e.*, the excited area, increased up to its maximum value of about 1.1 mm as plotted in Figure 6.7b. For $z > 0$ the laser line was no longer in contact with the edge and therefore the out-coupled PL was expected to decrease according to Equation 6.1. Indeed, Figure 6.7c shows that the PL intensity collected from the edge drops exponentially with increasing z and a loss coefficient of $\gamma = 7 \text{ cm}^{-1}$ is extracted. This loss coefficient is a factor of 5-7 lower than those found for similar nanotube/polymer waveguides¹⁵² and reflects the

high waveguide quality obtained from spin-coating the nanotube/polymer blend onto low-index MgF_2 substrates.

In summary, the fabricated waveguides show efficient light propagation on the length scale of $\gamma^{-1} = 1.4$ mm. Given that the core thickness in the employed waveguides was still close to the cut-off condition for NIR waveguiding, increasing the nanotube/polymer film thickness appears to be the most promising approach to improve the waveguiding efficiency.

Since the nanotubes strongly absorb NIR light and sp^3 defects give rise to nearly reabsorption-free luminescence, sp^3 functionalized SWNTs may be an interesting material for luminescent solar concentrators (LSCs).¹⁴⁹⁻¹⁵¹ For this application, the thickness of the waveguiding layer is typically in the range of 2-2000 μm resulting in strong light trapping.¹⁵¹ Beside the waveguiding efficiency, the PLQY must be enhanced to compete with state of the art LSCs.¹⁵¹ If these issues could be resolved, the spectral characteristics of defect-tailored SWNTs may provide a strong incentive to explore their use in LSCs to boost the power conversion efficiency of solar cells.¹⁴⁹

Nevertheless, light waves traveling along a path of about 1 mm length in the present waveguides already encounter a large number of luminescent defects. Therefore, such a layout holds promise for sizable optical gain if population inversion could be achieved in the material. For that reason, the next Section discusses the power-dependence of defect emission and the PL output of the fabricated waveguides at high excitation densities.

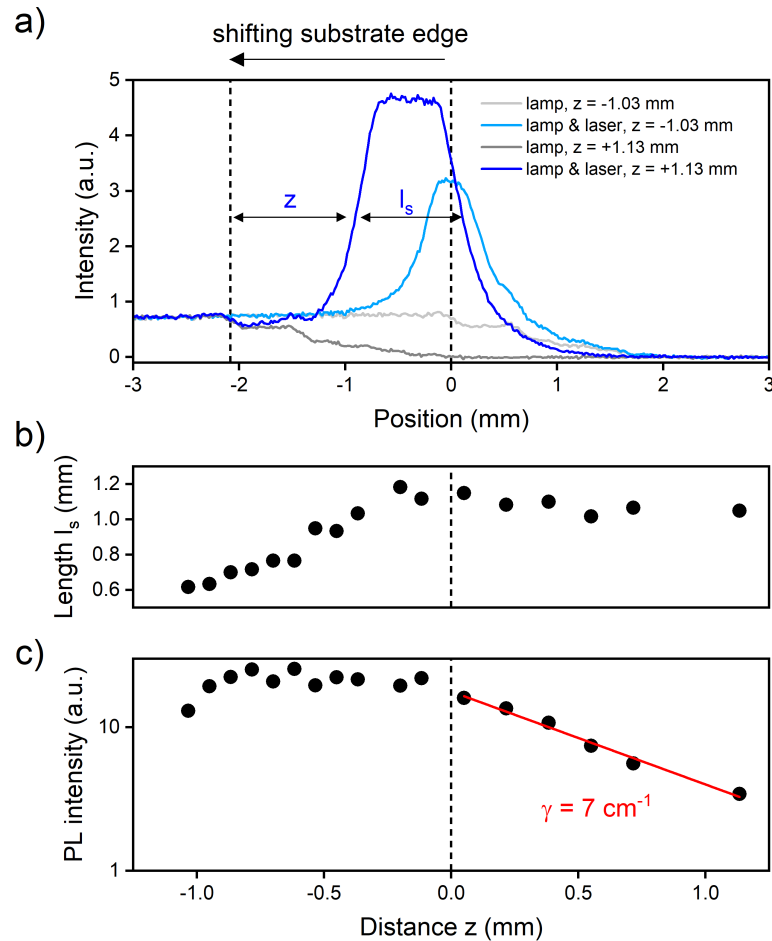


Figure 6.7: Determination of waveguide losses in a shifting excitation spot experiment. (a) Intensity profiles extracted from images corresponding to the start and end point of the experiment. Under lamp illumination, the position of the substrate edge is obtained from transmission images (gray and light gray). Upon unblocking the excitation laser, its back-reflection (blue and light blue) indicates the stripe position and length on the substrate surface. The definition of the stripe length l_s and distance z are exemplified for the end point of the scan. (b) Stripe length l_s on the substrate as a function of sample position represented by the distance z . Initially, the stripe length increases as the substrate is moved toward the stripe. The projected length then saturates at the full stripe length of around 1.1 mm. (c) PL intensity collected from the edge as a function of sample position represented by the distance z . Note that for $z > 0$, the variable z is equal to the distance between the excited region and the substrate edge. The red line is a linear fit to the log-linear plot used to obtain the loss coefficient γ . The intensity plateau for $z < 0$ is due to the relatively long laser line with a full length comparable to γ^{-1} .

6.4 Emission at high excitation densities

Before considering the case of waveguide integration, the pump power-dependence of the PL from sp^3 functionalized SWNTs should be discussed in general. Figure 6.8a displays PL spectra measured on a film of (6,5) SWNTs with a high density of 4-bromophenyl defects under different power densities of cw excitation. The E_{11} -normalized spectra show a strong decrease of the E_{11}^*/E_{11} and E_{11}^{*-}/E_{11} PL intensity ratios with increasing pump power. In addition, Figure 6.8b indicates that the onset of PL saturation occurs at much smaller pump powers for the E_{11}^* and E_{11}^{*-} than for the E_{11} signal. This trend is consistent with previous reports¹²⁶ and may be ascribed to differences in the mechanisms responsible for saturation of the intrinsic E_{11} and defect-associated E_{11}^* and E_{11}^{*-} PL signals.

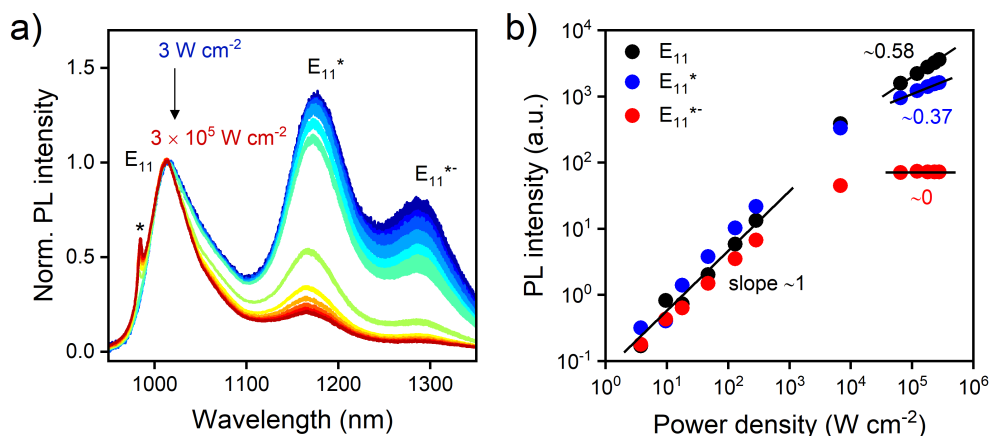


Figure 6.8: (a) E_{11} -normalized, pump power-dependent PL spectra of a spin-coated film of 4-bromophenyl-functionalized (6,5) SWNTs on glass acquired under cw excitation at 785 nm. The asterisk marks a Raman signal corresponding to the 2D mode. (b) Integrated PL intensities of E_{11} , E_{11}^* and E_{11}^{*-} emission as a function of pump power density.

It is well-established that E_{11} emission saturates due to Auger-type exciton-exciton annihilation upon collision of two mobile E_{11} excitons.^{256–259} Since their lifetime is short (~ 10 ps),¹⁰¹ high exciton densities and thus, pump powers, are required for significant interaction and Auger quenching of E_{11} emission. Defect-localized excitons, on the other hand, have substantially longer lifetimes¹⁰⁴ (> 100 ps) and hence even at low exciton densities there is a considerable probability that a mobile exciton encounters a trapped exciton. This scenario should lead to emission saturation due to state-filling, *i.e.*, the mobile exciton cannot be trapped in an occupied defect state.¹²⁶ However,

it is unclear whether pure state-filling is the only mechanism that contributes to PL saturation or Auger quenching involving a mobile and a localized exciton participates as well. As pointed out by Ma *et al.*,²³⁴ the latter process should be evident in the E_{11}^* or E_{11}^{*-} PL lifetime as a fast decay component that emerges at high excitation densities. Unfortunately, such experiments tend to be compromised by photo-induced degradation.²³⁴ Although a comprehensive model of exciton-exciton interactions at sp^3 defects is not available yet, the low-threshold PL saturation of luminescent defects is clearly attributable to the prolonged lifetime of localized excitons. This notion is further corroborated by the observation that the E_{11}^{*-} emission saturates at even lower pump power than the E_{11}^* emission (see Figure 6.8b) in accordance with the longer E_{11}^{*-} exciton lifetime.

It should be noted that even though high cw excitation densities appear to fully saturate the E_{11}^{*-} transition (Figure 6.8b), which corresponds to high exciton densities in the E_{11}^{*-} state, amplified spontaneous emission is highly unlikely to be observed in the given measurement configuration (excitation and detection through the same objective) owing to the short path length of PL within the material.¹⁵⁷ For this reason, the characterization of waveguide-integrated sp^3 functionalized SWNTs is crucial.

As discussed above, fast exciton diffusion and long lifetimes of trapped excitons lead to efficient filling of defect states which is a prerequisite for population inversion and potential optical gain.¹²⁶ In order to achieve the highest excitation densities and approach population inversion while minimizing undesired sample heating, the PL excitation wavelength should be optimized. For this purpose, a photoluminescence excitation-emission (PLE) map of 4-bromophenyl-functionalized (6,5) SWNTs was recorded (Figure 6.9a) and the excitation spectrum extracted at the peak wavelength of E_{11}^* emission (Figure 6.9b).

The excitation spectrum reveals that pumping at the E_{11} transition generates E_{11}^* PL about 4 times more efficiently than pumping at the higher-energy E_{22} transition or the K -momentum phonon sideband (PSB). Since defect states are populated *via* trapping of E_{11} excitons,¹⁰³ the lower E_{11}^* PL efficiency upon higher-energy excitation may be attributed to loss channels, such as exciton dissociation, that compete with intersubband relaxation of higher resonances to the E_{11} band-edge exciton.^{265,266}

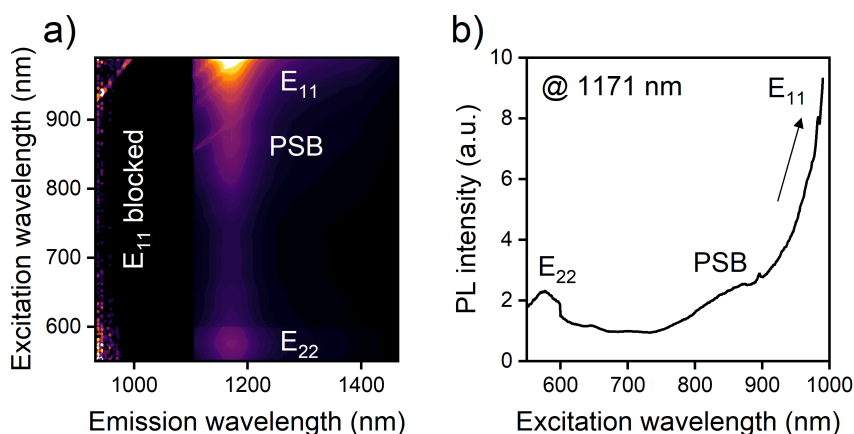


Figure 6.9: (a) PLE map measured on an aerosol-jet printed film of 4-bromophenyl-functionalized (6,5) SWNTs on glass. Note that the spectral range below 1100 nm was blocked by a long-pass filter to enable a wide excitation wavelength scan up to the E_{11} transition. (b) PL intensity at the E_{11}^* peak wavelength (1171 nm) as a function of excitation wavelength.

Returning to the characterization of waveguide-integrated sp^3 functionalized SWNTs in the right-angle configuration described in Section 3.4.5 and Section 6.3, the following conditions were chosen to increase the prospects of observing optical gain: (i) The length of the excited region on the film was adjusted to $1.4 \text{ mm} = \gamma^{-1}$ such that the full propagation length was harnessed; (ii) the pump wavelength was tuned to 985 nm to be nearly resonant with the E_{11} transition while staying below the filter cut-off at 1000 nm that blocked unwanted NIR laser wavelengths; (iii) ultrashort laser pulses (78 fs pulse duration) were employed to produce high instantaneous exciton densities and avoid continuous sample heating. Moreover, the PL response of both E_{11}^* - and E_{11}^{*-} -emitting sp^3 defects was studied to account for their distinct spectral overlap with excited state absorption features of the pristine (6,5) SWNT.²⁶⁷ To this end, (6,5) SWNTs were functionalized using either diazonium chemistry (Br-Dz, $C_{Dz} = 1.85 \text{ mmol L}^{-1}$, Route II, see Section 3.2.1) to create predominantly E_{11}^* -emitting defects or a base-mediated reaction with 2-iodoaniline to selectively introduce E_{11}^{*-} -emitting defects (refer to Settele *et al.*²³⁸). Subsequently, both types of functionalized SWNTs were embedded in waveguide structures as depicted in Figure 6.5a.

The pump power-dependent spectra of the PL collected from the waveguide edge under line excitation are shown in Figure 6.10a,b for the two types of waveguide-integrated sp^3 functionalized (6,5) SWNTs. Note that the spectral range below 1100 nm was blocked by a long-pass filter to suppress scattered laser light. Since a high concentration of

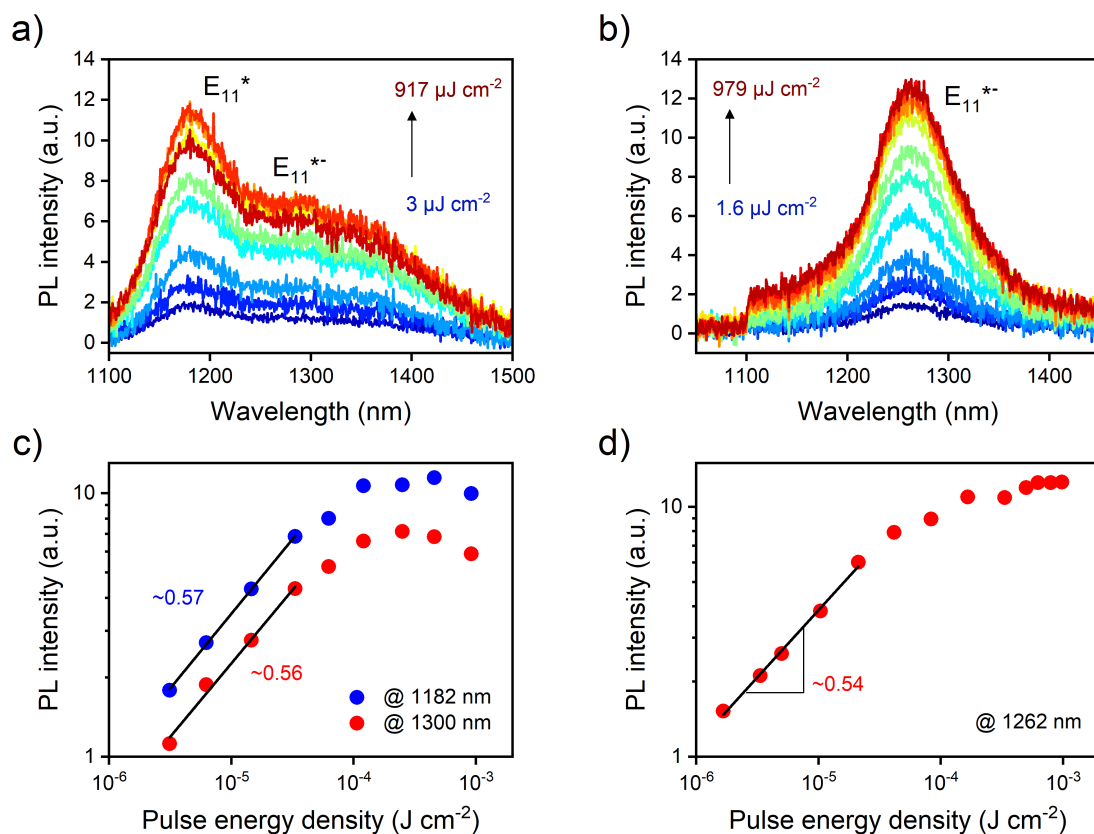


Figure 6.10: Pump power-dependent spectra of the PL out-coupled from the edge of a waveguide based on (6,5) SWNTs with predominantly (a) E_{11}^* -emitting or (b) E_{11}^{*-} -emitting sp^3 defects. The emission intensities at characteristic wavelengths are plotted as a function of pulse energy density in (c) and (d) for the waveguides in (a) and (b), respectively. The excitation wavelength was 985 nm. As pulsed excitation was employed, the pump power is represented by the pulse energy density (in units of J cm^{-2}) and not by the average power density (in units of W cm^{-2}) as in the cw case.

diazonium salt was used to produce the sample characterized in Figure 6.10a, not only the E_{11}^* but also the E_{11}^{*-} PL signal was observed. The aniline/base-functionalized (6,5) SWNTs, on the other hand, showed nearly pure E_{11}^{*-} emission (Figure 6.10b). In all cases, the defect PL signals saturate or even quench at high pump powers. In addition, the background level of the spectra increases with excitation power, in particular toward the short-wavelength filter cut-off. This background signal might originate from residual scattered laser light or E_{11} -associated PL sidebands that become more prominent at higher excitation densities owing to the higher saturation-threshold of E_{11} excitons compared to defect-localized excitons (compare Figure 6.8).

Figure 6.10c,d reveal that even the lowest excitation densities used in this experiment do not give rise to linear PL response as evident from a slope < 1 in the log-log

plot of PL intensity *vs.* power. Hence, an even more sensitive PL detection would be required to probe the linear regime in this measurement configuration. Upon raising the pulse energy density to a few $100 \mu\text{J cm}^{-2}$, the E_{11}^* and E_{11}^{*-} PL intensities become essentially constant as is commonly observed for E_{11} PL under intense pulsed excitation as well.^{257,258} At the highest pump powers (about 1 mJ cm^{-2}), the emission intensity of both defect types even decreases (Figure 6.10c) in agreement with previous studies on the single-tube level.¹²⁸ Such a drop of absolute PL intensity at high pump power might be related to photo-degradation²⁶⁸ or the emergence of additional loss channels, for instance, biexciton formation.²⁶⁹

Since the E_{11}^* and E_{11}^{*-} PL intensities saturate and remain nearly constant across an order of magnitude in pump power, it can be concluded that sp^3 defects do not show optical gain under the given conditions. Otherwise, a doubling of slope in the log-log plot of PL intensity *vs.* power, indicative of amplified spontaneous emission, would have been expected at a certain threshold pump power.¹⁵⁷

In general, light amplification occurs when the gain due to stimulated emission (which scales with the density of excitations) exceeds the losses associated with non-radiative recombination and stray light escaping from the amplifier.¹⁵⁷ Consequently, several effects may be responsible for the absence of optical gain in sp^3 defects. First of all, waveguiding losses exist and could mask an optical gain that is smaller than the loss coefficient $\gamma = 7 \text{ cm}^{-1}$. Improving the film smoothness and homogeneity could help to reduce light propagation losses and thus, the threshold for optical gain. Other processes could lead to a drop of E_{11}^* and E_{11}^{*-} PLQY at high excitation densities. Most notably, Auger quenching of mobile and trapped excitons leads to non-radiative losses.²³⁴ Furthermore, laser-induced heating can not only cause sample degradation, but also promote thermal detrapping of defect-localized excitons.¹¹³ Finally, Sykes *et al.* recently suggested that the absence of any detectable stimulated emission from sp^3 defects in (6,5) SWNTs might be due to spectral overlap of E_{11}^* emission with the excited state absorption of optically generated trions.²⁶⁷ This explanation, however, is unlikely given that E_{11}^{*-} defects did not exhibit optical gain either, despite negligible overlap with the trion feature of (6,5) SWNTs.

In summary, a more detailed knowledge of exciton-exciton annihilation and thermal detrapping processes in functionalized SWNTs are required to evaluate whether optical

gain could possibly be realized in this material. Beyond that, the fabrication of higher-quality waveguides hosting functionalized SWNTs with enhanced PLQYs may help to achieve this goal.

6.5 Electroluminescence from sp^3 defects

As pointed out in the introductory Section 6.1, the key benefit of an sp^3 functionalization method for polymer-wrapped SWNTs is the ease with which the resulting defect-tailored SWNTs can be integrated into optoelectronic devices. Here, PFO-BPy-wrapped sp^3 functionalized (6,5) SWNTs were integrated in light-emitting field-effect transistors (LEFETs) following a standard procedure developed for pristine SWNTs (Section 3.3.4).²⁷⁰

For this purpose, aryl defects were introduced to (6,5) SWNTs using diazonium chemistry (Br-Dz, $C_{Dz} = 1.85 \text{ mmol L}^{-1}$, Route II, see Section 3.2.1). The chosen reaction conditions led to relatively high defect densities as confirmed by the large E_{11}^*/E_{11} PL intensity ratio and the elevated D/ G^+ mode intensity ratio in the Raman spectrum (listed in Table 6.3). By using the correlations established in Section 4.6 between these relative metrics and the defect density calculated within the DLCQ model, the density of luminescent defects in this particular sample may be estimated to be around 10 – 15 defects per μm tube length.

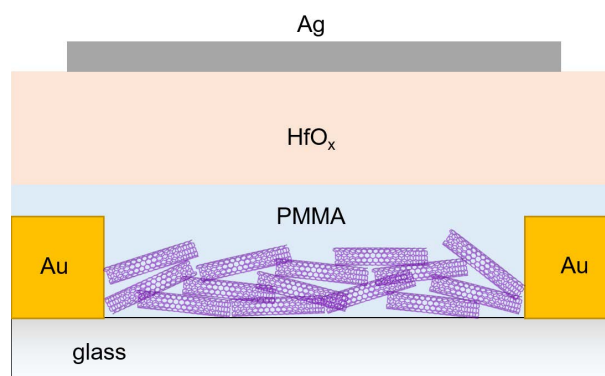


Figure 6.11: Schematic of the employed bottom-contact/top-gate field-effect transistor structure.

After the usual purification and re-dispersion steps, the functionalized SWNTs were spin-coated onto pre-patterned gold contacts on glass to form a dense network of randomly oriented nanotubes (linear density of ~ 20 tubes per micrometer). The

networks were annealed at a moderately high temperature of 150 °C to drive water out of the network while avoiding the cleavage of covalently attached aryl groups.²⁷¹ Subsequent deposition of a PMMA/hafnium oxide hybrid dielectric and a silver top-gate completed the transistor structure, which is schematically shown in Figure 6.11. As a reference sample, a device based on pristine (6,5) SWNTs was fabricated under the same conditions.

Table 6.3: Summary of material and device characterization for samples of pristine and 4-bromophenyl-functionalized (6,5) SWNTs. The E_{11}^*/E_{11} PL signal ratio refers to spectrally-integrated intensities. The corresponding PL spectra were measured for SWNTs in toluene dispersion under pulsed excitation with 0.5 mJ cm^{-2} at 575 nm. Raman spectra were recorded with a 532 nm excitation laser. Linear charge carrier mobilities are reported for devices with a channel length $L = 20 \text{ }\mu\text{m}$. The data represent average values over 8 devices per type.

| Sample | PL E_{11}^*/E_{11} | Raman D/G ⁺ | μ_{lin}^h ($\text{cm}^2 \text{V}^{-1} \text{s}^{-1}$) | μ_{lin}^e ($\text{cm}^2 \text{V}^{-1} \text{s}^{-1}$) |
|---------------|----------------------|------------------------|---|---|
| pristine | - | 0.04 | 5.00 ± 0.21 | 1.19 ± 0.15 |
| sp^3 funct. | 14 | 0.12 | 2.54 ± 0.13 | 0.57 ± 0.07 |

While sp^3 defects may enhance the luminescence quantum yield of SWNTs (see Section 4.4 and 6.2), they simultaneously degrade the electrical conductivity of carbon nanotubes.^{16,272,273} The increase in resistance associated with creation of a single sp^3 defect on an individual nanotube was estimated to be in the range of $6 \text{ }\Omega$ ²⁷² to a few $100 \text{ }\Omega$ ¹⁶ and may thus be comparable to that of an intertube junction.^{274,275} Hence, devices based on sp^3 functionalized SWNTs are expected to exhibit a lower charge carrier mobility than the pristine reference. Interestingly, the electrical transfer characteristics shown in Figure 6.12a,d indicate only a moderate degradation of charge transport properties for the given level of functionalization. As presented in Table 6.3, the linear mobilities for electrons and holes are both reduced by a factor of 2. It is worth noting that the drop of mobility is almost identical for negatively and positively charged carriers and thus pointing toward similar interactions of sp^3 defects with electrons and holes, respectively. Despite the comparatively high defect density which is already above the level leading to the maximum PLQY (see Section 4.4), charge transport through a network of functionalized SWNTs is still relatively efficient, presumably aided by the large number of percolation paths in the dense nanotube network.²⁷⁶ Upon operating the LEFETs in the ambipolar regime and at sufficiently high drain currents ($> 1 \text{ }\mu\text{A}$), EL was generated in the center of the channel as described in

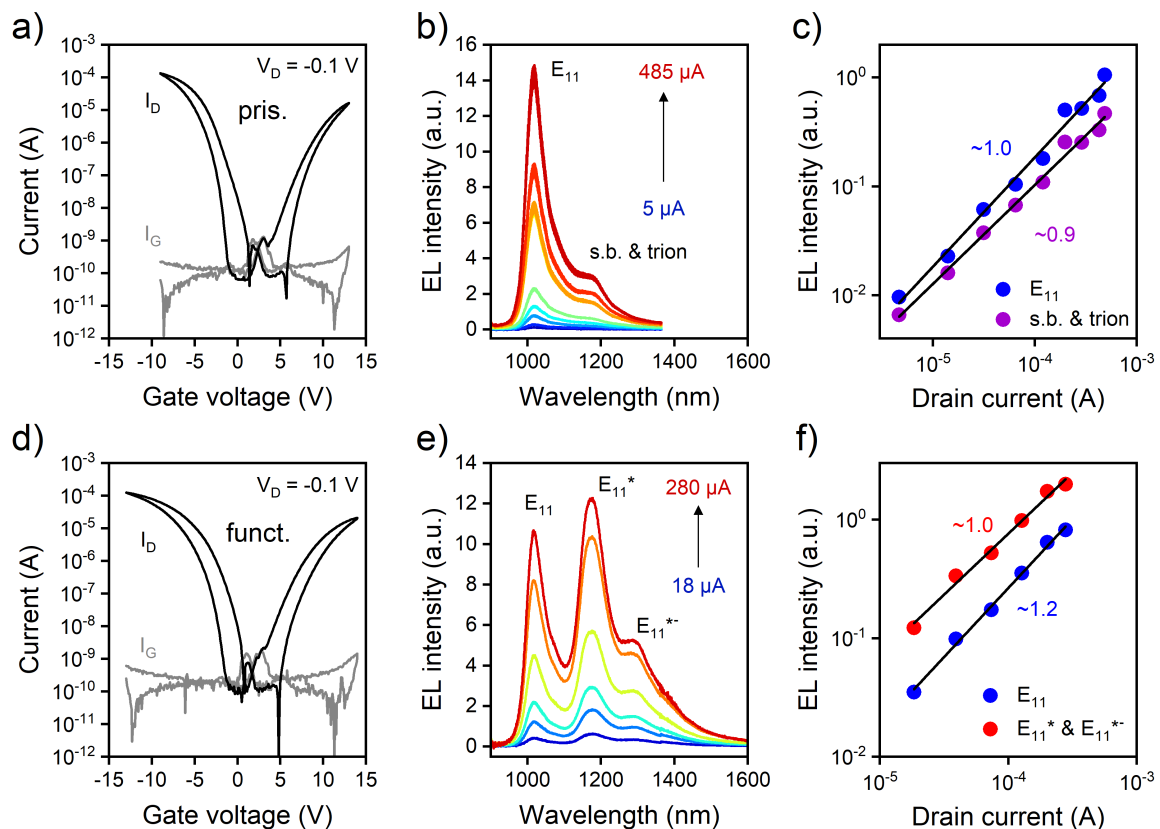


Figure 6.12: Current-voltage and electroluminescence (EL) characterization at room temperature for devices based on (a-c) pristine and (d-f) sp^3 functionalized (6,5) SWNTs: (a,d) Current-voltage transfer curves; (b,e) EL spectra measured under device operation in the ambipolar regime; (c,f) spectrally-integrated EL intensity plotted *versus* the drain current. The E_{11} band was defined as the wavelengths < 1100 nm, whereas the defect, trion and E_{11} -related sidebands (s.b.) were assigned to the wavelengths > 1100 nm.

Section 2.4. The emitted light was collected with an objective and the corresponding spectra are shown in Figure 6.12b,e. The sp^3 functionalized SWNTs exhibit EL from the intrinsic E_{11} and the defect-associated E_{11}^* and E_{11}^{*-} transitions, whereas the pristine reference displays only E_{11} emission accompanied by a weak sideband and a trion signal. Surprisingly, the E_{11}^*/E_{11} EL signal ratio (~ 2) is much smaller than the corresponding PL intensity ratio measured in dispersion (~ 14 , see Table 6.3). To check whether this mismatch might be the result of state-filling and concomitant non-linear EL response, the EL intensity of each emission feature was plotted as a function of drain current (see Figure 6.12c,f), which is assumed to be proportional to the exciton generation rate. As indicated by the slope of ~ 1 in the log-log plot of EL intensity *vs.* drain current, both E_{11} and E_{11}^* emission are in the linear regime and there are no signs

of significant state-filling or exciton-exciton annihilation. This picture is also consistent with instantaneous exciton densities of around 0.1 per μm tube length estimated for electrical excitation with $100\ \mu\text{A}$.

Other possible explanations for this observation include quenching of defect-localized excitons by free charge carriers²⁶³ or the preferential passage of current through less defective tube segments with lower resistance. To corroborate or exclude these hypotheses, additional experiments such as charge-modulation PL spectroscopy²⁷⁰ and temperature-dependent charge transport measurements^{52,64} are required. Nevertheless, the demonstration of EL from sp^3 defects in a simple LEFET structure opens up new avenues for electrically-driven single-photon emission and nanotube-based NIR light-emitting devices with enhanced quantum efficiency.

6.6 Summary and conclusion

This Chapter demonstrated the excellent solution-processability of polymer-wrapped sp^3 functionalized SWNTs, which were made accessible through the synthetic protocol developed in Chapter 4. Deposition techniques such as spin-coating and aerosol-jet printing were employed to produce homogeneous thin films of functionalized SWNTs and ultimately enable their integration into photonic structures including waveguides and light-emitting field-effect transistors.

Similar to the behavior of pristine SWNTs, the PLQY of sp^3 functionalized SWNTs deposited on glass substrates was found to be an order of magnitude lower than in toluene dispersion. Since the PLQYs of the mobile (E_{11}) and the defect-localized excitons (E_{11}^*) were reduced by the same factor, the defect-induced PL brightening observed in dispersion was retained in thin films. Furthermore, PL lifetime measurements revealed that the E_{11}^* PL quenching in nanotube films is primarily due to enhanced non-radiative recombination, which might originate from increased dielectric screening by the polar glass substrate. Therefore, applying suitable passivation layers to the substrate surface or embedding the sp^3 functionalized nanotubes in matrices with low dielectric permittivity may boost the E_{11} and E_{11}^* emission efficiency.

Thin films of sp^3 functionalized SWNTs in polystyrene on magnesium fluoride substrates with low refractive index yielded a planar dielectric waveguide structure that

efficiently channeled E_{11}^* and E_{11}^{*-} PL over distances of around 1.4 mm. In the future, careful tuning of the waveguide core thickness might enable the precise cut-off of longer wavelength E_{11}^{*-} emission and thus provide a way to generate pure E_{11}^* emission. Upon further improvement of PLQY and waveguiding efficiency, defect-tailored SWNTs could be an attractive material for near-infrared luminescent solar concentrators.

These waveguides also served as a platform to evaluate the potential for optical gain in functionalized SWNTs. The PL output of sp^3 defects was found to saturate at substantially lower excitation densities than the E_{11} emission of the pristine lattice, which is a direct consequence of the longer lifetime of defect-localized excitons. Under intense pulsed excitation (1 mJ cm^{-2} near-resonant with the E_{11} transition), the emission from the E_{11}^* and E_{11}^{*-} defect states remained completely saturated or even quenched slightly. Hence, there are no indications of optical gain in sp^3 defects under the investigated conditions. In order to assess whether optical gain could be realized in functionalized SWNTs at all, a better understanding of exciton-exciton annihilation and thermal detrapping processes at luminescent defects are required.

Finally, the integration of defect-tailored SWNTs into a light-emitting field-effect transistor structure enabled the generation of electroluminescence from sp^3 defects. Even at defect densities above those leading to the highest E_{11}^* PLQY, networks of functionalized SWNTs supported efficient charge transport as indicated by the moderate mobility reduction (by a factor of 2) with respect to the pristine reference. In the ambipolar regime, light emission from the intrinsic E_{11} and the defect-associated E_{11}^* and E_{11}^{*-} states was observed, thus confirming the population of emissive defect states, which is a prerequisite for the realization of electrically-pumped quantum light sources based on sp^3 functionalized SWNTs.

Chapter 7

Conclusion and Outlook

At the start of this thesis, the introduction of luminescent sp^3 defects had already proved to be a powerful approach to enhance the photoluminescence (PL) quantum yields of carbon nanotubes¹⁰² and to accomplish room-temperature single-photon emission in the near-infrared.¹⁴ However, the employed synthetic methods were limited to aqueous dispersions of SWNTs with often short tube lengths, residual metallic nanotubes and poor solution-processability, which hampered the integration of sp^3 defects into optoelectronic devices and prevented many aspects of their photophysics from being explored.

This thesis overcame these issues through the development of a functionalization method for polymer-wrapped SWNTs in organic solvents yielding luminescent aryl defects. Thanks to this advance, electronically-pure (6,5) SWNTs with long average tube lengths ($> 1 \mu\text{m}$) obtained from polymer-sorting under shear force mixing²⁰ became amenable to sp^3 functionalization. This model system allowed for the investigation of defect-localized excitons in high-quality SWNTs (Chapter 4), the modification of exciton dynamics through the influence of attached functional groups (Chapter 5) and the integration of sp^3 functionalized SWNTs into photonic structures and light-emitting devices (Chapter 6).

Chapter 4 described a simple sp^3 functionalization method for polymer-wrapped SWNTs that relies on the solubilization of aryldiazonium salts by an ether crown in a toluene/acetonitrile mixture. Since all reagents are commercially available and the reaction proceeds under ambient conditions, this method is perfectly suited for the scalable production of sp^3 functionalized SWNTs for device applications, as was demonstrated in Chapter 6. The large tube lengths and the low-permittivity environment provided by the wrapping polymer and the organic solvent (toluene) led to a comparatively high PL quantum yield (PLQY) of around 4% in (6,5) SWNTs decorated with electron-poor aryl defects, which corresponds to a 1.7-fold enhancement with respect to the pristine reference. This relatively small defect-induced brightening, compared to factors of 5-10 for short (6,5) SWNTs in water,¹⁰² may be attributed to the high quality of shear-mixed (6,5) SWNTs. While the PLQY of E_{11} excitons is defined by diffusive quenching at tube ends and other lattice defects,¹⁰¹ whose density depend on nanotube growth and processing conditions, the PLQY of defect-localized E_{11}^* excitons is limited by intrinsic loss channels, such as multi-phonon decay and thermal detrapping.^{104,105}

Hence, with increasing quality of the nanotube starting material, the absolute PLQYs before and after functionalization are expected to grow, whereas the defect-induced relative brightening should follow an inverse trend. Consequently, the introduction of sp^3 defects may even reduce the overall PLQY for SWNTs of sufficiently high quality, as might be observable, for example, in CVD-grown air-suspended SWNTs.^{186,250}

Furthermore, the polymer-wrapped SWNTs showed well-resolved absorption spectra, in which the E_{11}^* absorption arising from sp^3 defects could be unambiguously identified. Upon estimating the defect density within a diffusion-limited contact quenching model and accounting for the exciton size, the oscillator strength of the defect-localized E_{11}^* exciton was found to be similar to that of the intrinsic E_{11} exciton. This result greatly simplifies the characterization of sp^3 functionalized SWNTs as the average density of exciton trapping sites can be deduced from a simple absorption measurement. In addition, the correspondence in oscillator strengths of the E_{11} and E_{11}^* transitions indicates similar radiative relaxation rates for mobile and trapped excitons, respectively, and thus corroborates the notion that the commonly observed defect-induced PLQY enhancement is primarily due to the deactivation of diffusive quenching upon exciton localization.

Chapter 5 demonstrated that the localization of excitons around sp^3 defects also enables their efficient interaction with covalently attached stable organic radicals and thus provides a way to control exciton photophysics in carbon nanotubes. More specifically, diazonium chemistry was used to link perchlorotriphenylmethyl (PTM) radicals to polymer-wrapped (6,5) SWNTs *via* luminescent aryl defects. By virtue of the non-polar PTM group, the tailored aryldiazonium salt was ideally suited for the reaction with polymer-wrapped SWNTs in organic solvents. The presence of the PTM radical substituent on the sp^3 defect caused a 2.5-fold quenching of E_{11}^* PL, which can be explained by the transfer of exciton population from the bright E_{11}^* singlet to a dark triplet state mediated by radical-enhanced intersystem crossing and a smaller contribution due to photoinduced electron transfer. In contrast to that, the E_{11} emission remained unaffected, in agreement with long average distances between mobile excitons and the point of sp^3 functionalization.

Based on these results, the interaction of excitons with nearby spins holds promise for enhancing the triplet population and might even serve as a general concept for probing

the elusive triplet manifold in pristine and sp^3 functionalized SWNTs in future studies. Understanding triplet states is of high importance for the development of more efficient electroluminescent and photovoltaic devices based on carbon nanotubes. In addition, the observation of stronger spin-orbit interactions at sp^3 defects in graphene²⁷⁷ raises the question whether similar effects could be realized in suitably designed nanotube defects.^{91,229} In such a scenario, triplet excitons might satisfy the requirements for optically-addressable spin states in quantum information technology.^{278,279}

Beside the tuning of exciton properties, spin-labeled defects could be useful for many other purposes. For instance, as pulsed EPR methods can measure the distance between spins on a nanometer scale,²⁸⁰ such defects could serve as a model system to investigate clustering and thus contribute to understanding luminescent defects on a molecular scale.^{176,185} Moreover, upon transferring²⁸¹ radical-tailored SWNTs into biocompatible surfactants,²⁸² such nanotubes might be usable as metal-free contrast agents for *in vivo* magnetic resonance imaging^{200,205} complementary to near-infrared bioimaging.^{11,12,17} Lastly, as diazonium chemistry is even more efficient for metallic SWNTs,²⁸³ the presented synthetic route could enable the fabrication of spin valves^{202,206} based on all-organic, radical-decorated SWNTs.

In Chapter 6, luminescent aryl defects were introduced according to the method presented in Chapter 4 and subsequently characterized in thin films and optoelectronic devices. The sp^3 functionalized and polymer-wrapped (6,5) SWNTs showed excellent solution-processability and standard deposition techniques such as spin-coating and aerosol-jet printing yielded homogeneous and large-area thin films. Upon depositing the sp^3 functionalized SWNTs as a neat film on glass, both the E_{11} and E_{11}^* PLQY decreased by a factor of about 10 with respect to the PLQYs in toluene dispersion. This PLQY reduction likely originates from increased dielectric screening by the polar glass substrate and highlights the role of the dielectric environment of the emitter for the electroluminescence efficiency in devices. Consequently, the light emission might be enhanced by embedding the nanotubes in a non-polar polymer matrix or by passivating the substrate surface.

Furthermore, thin films of sp^3 functionalized (6,5) SWNTs in polystyrene on low-index magnesium fluoride substrates served as planar dielectric waveguides for E_{11}^* and E_{11}^- emission and showed efficient light propagation on the length scale of

1.4 mm. As the emitted PL travels a long distance through the nanotube/polymer layer, these waveguide structures were used to search for optical gain in sp^3 defects. However, the E_{11}^* and E_{11}^{*-} emission saturated or even quenched under intense pulsed excitation. Thus, there are no indications of optical gain, which might be due to exciton-exciton annihilation involving mobile and trapped excitons, thermal detrapping at high excitation densities or photo-degradation. In future studies, these hypotheses should be tested by pump power-dependent PL lifetime measurements.²³⁴ Based on the available data, it appears unlikely that sp^3 defects will enable lasing with carbon nanotubes.

Finally, dense networks of sp^3 functionalized (6,5) SWNTs were integrated into a light-emitting field-effect transistor (LEFET) structure. Operating the transistor in the ambipolar regime generated electroluminescence (EL) from sp^3 defects in the center of the channel and thus confirmed the population of emissive defect states under electrical excitation. Hence, sp^3 functionalization is a promising route to tune the emission spectrum and potentially enhance the EL intensity of nanotube-based LEFETs and light-emitting diodes.²⁶⁰ Moreover, the realization of electrically-driven single-photon sources will facilitate the integration of quantum emitters into more complex architectures and allow their full potential to be harnessed.

In the future, one of the main objectives should be the transfer of concepts and applications demonstrated for the example of (6,5) and other small-diameter SWNTs to larger-diameter SWNTs with smaller optical band gaps. This will shift the E_{11}^* and E_{11}^{*-} emission bands closer to the desirable telecommunication C band and boost their application potential. As previous reports pointed toward a drop of defect state PLQY for chiralities with larger diameter,^{14,102} it might be necessary to combine this approach with the targeting of defect binding configurations with larger optical red-shifts (E_{11}^{*-}).²³⁸ In addition, many potential applications, especially those utilizing individual nanotubes, cannot tolerate the spectral diversity found in today's samples of sp^3 functionalized SWNTs. The distribution of emission signals may be narrowed down through the selective creation of specific binding configurations^{127,238} and smoothing out the dielectric environment. Furthermore, as the study of sp^3 defects in high-quality nanotube hosts revealed the limitations of defect-induced PL brightening, it appears reasonable to focus less on the optimization of PLQYs and more on new

functionalities in imaging, sensing and quantum light emission that arise from exciton localization. In particular, given the high levels of indistinguishability displayed by single photons emitted from cavity-integrated sp^3 defects,¹⁵ the implementation of quantum cryptography based on luminescent defects seems to be within reach.

Bibliography

1. Sillard, P. & Molin, D. in *Fibre Optic Communication* (eds Venghaus, H. & Grote, N.) 49–102 (Springer, Cham, 2017).
2. Grote, N., Möhrle, M. & Ortsiefer, M. in *Fibre Optic Communication* (eds Venghaus, H. & Grote, N.) 103–149 (Springer, Cham, 2017).
3. Nathan, A. *et al.* Flexible Electronics: The Next Ubiquitous Platform. *Proc. IEEE* **100**, 1486–1517 (2012).
4. Schubert, M. *et al.* Monitoring contractility in cardiac tissue with cellular resolution using biointegrated microlasers. *Nat. Photonics* **14**, 452–458 (2020).
5. Zaumseil, J. Single-walled carbon nanotube networks for flexible and printed electronics. *Semicond. Sci. Technol.* **30**, 074001 (2015).
6. Zaumseil, J. Semiconducting Single-Walled Carbon Nanotubes or Very Rigid Conjugated Polymers: A Comparison. *Adv. Electron. Mater.* **5**, 1800514 (2019).
7. Brozena, A. H., Kim, M., Powell, L. R. & Wang, Y. Controlling the optical properties of carbon nanotubes with organic colour-centre quantum defects. *Nat. Rev. Chem.* **3**, 375–392 (2019).
8. Gifford, B. J., Kilina, S., Htoon, H., Doorn, S. K. & Tretiak, S. Controlling Defect-State Photophysics in Covalently Functionalized Single-Walled Carbon Nanotubes. *Acc. Chem. Res.* **53**, 1791–1801 (2020).
9. Shiraki, T., Miyauchi, Y., Matsuda, K. & Nakashima, N. Carbon Nanotube Photoluminescence Modulation by Local Chemical and Supramolecular Chemical Functionalization. *Acc. Chem. Res.* **53**, 1846–1859 (2020).

10. Ghosh, S., Bachilo, S. M., Simonette, R. A., Beckingham, K. M. & Weisman, R. B. Oxygen Doping Modifies Near-Infrared Band Gaps in Fluorescent Single-Walled Carbon Nanotubes. *Science* **330**, 1656–1659 (2010).
11. Mann, F. A., Herrmann, N., Opazo, F. & Kruss, S. Quantum Defects as a Toolbox for the Covalent Functionalization of Carbon Nanotubes with Peptides and Proteins. *Angew. Chem. Int. Ed.* **59**, 17732–17738 (2020).
12. Mandal, A. K. *et al.* Fluorescent sp^3 Defect-Tailored Carbon Nanotubes Enable NIR-II Single Particle Imaging in Live Brain Slices at Ultra-Low Excitation Doses. *Sci. Rep.* **10**, 5286 (2020).
13. Lounis, B. & Orrit, M. Single-photon sources. *Rep. Prog. Phys.* **68**, 1129–1179 (2005).
14. He, X. *et al.* Tunable room-temperature single-photon emission at telecom wavelengths from sp^3 defects in carbon nanotubes. *Nat. Photonics* **11**, 577–582 (2017).
15. Luo, Y. *et al.* Carbon Nanotube Color Centers in Plasmonic Nanocavities: A Path to Photon Indistinguishability at Telecom Bands. *Nano Lett.* **19**, 9037–9044 (2019).
16. Lee, Y. *et al.* Electrically Controllable Single-Point Covalent Functionalization of Spin-Cast Carbon-Nanotube Field-Effect Transistor Arrays. *ACS Nano* **12**, 9922–9930 (2018).
17. Mann, F. A., Lv, Z., Grosshans, J., Opazo, F. & Kruss, S. Nanobody-Conjugated Nanotubes for Targeted Near-Infrared In Vivo Imaging and Sensing. *Angew. Chem. Int. Ed.* **58**, 11469–11473 (2019).
18. Nißler, R. *et al.* Remote near infrared identification of pathogens with multiplexed nanosensors. *Nat. Commun.* **11**, 5995 (2020).
19. Kim, M. *et al.* Mapping Structure-Property Relationships of Organic Color Centers. *Chem* **4**, 2180–2191 (2018).
20. Graf, A. *et al.* Large scale, selective dispersion of long single-walled carbon nanotubes with high photoluminescence quantum yield by shear force mixing. *Carbon* **105**, 593–599 (2016).

21. Kataura, H. *et al.* Diameter control of single-walled carbon nanotubes. *Carbon* **38**, 1691–1697 (2000).
22. Sanchez-Valencia, J. R. *et al.* Controlled synthesis of single-chirality carbon nanotubes. *Nature* **512**, 61–64 (2014).
23. Prasek, J. *et al.* Methods for carbon nanotubes synthesis—review. *J. Mater. Chem.* **21**, 15872–15884 (2011).
24. Jiang, Y., Wang, H., Shang, X. F., Li, Z. H. & Wang, M. Influence of NH₃ atmosphere on the growth and structures of carbon nanotubes synthesized by the arc-discharge method. *Inorg. Mater.* **45**, 1237–1239 (2009).
25. Kusaba, M. & Tsunawaki, Y. Production of single-wall carbon nanotubes by a XeCl excimer laser ablation. *Thin Solid Films* **506-507**, 255–258 (2006).
26. Kim, K. S. *et al.* Large-scale production of single-walled carbon nanotubes by induction thermal plasma. *J. Phys. D: Appl. Phys.* **40**, 2375–2387 (2007).
27. Bachilo, S. M. *et al.* Narrow (n,m)-Distribution of Single-Walled Carbon Nanotubes Grown Using a Solid Supported Catalyst. *J. Am. Chem. Soc.* **125**, 11186–11187 (2003).
28. Kitiyanan, B., Alvarez, W. E., Harwell, J. H. & Resasco, D. E. Controlled production of single-wall carbon nanotubes by catalytic decomposition of CO on bimetallic Co–Mo catalysts. *Chem. Phys. Lett.* **317**, 497–503 (2000).
29. Resasco, D. E. *et al.* A scalable process for production of single-walled carbon nanotubes (SWNTs) by catalytic disproportionation of CO on a solid catalyst. *J. Nanoparticle Res.* **4**, 131–136 (2002).
30. Lolli, G. *et al.* Tailoring (n,m) Structure of Single-Walled Carbon Nanotubes by Modifying Reaction Conditions and the Nature of the Support of CoMo Catalysts. *J. Phys. Chem. B* **110**, 2108–2115 (2006).
31. Liu, B., Wu, F., Gui, H., Zheng, M. & Zhou, C. Chirality-Controlled Synthesis and Applications of Single-Wall Carbon Nanotubes. *ACS Nano* **11**, 31–53 (2017).
32. Coleman, J. N. Liquid-phase exfoliation of nanotubes and graphene. *Adv. Funct. Mater.* **19**, 3680–3695 (2009).

33. O'Connell, M. J. *et al.* Band Gap Fluorescence from Individual Single-Walled Carbon Nanotubes. *Science* **297**, 593–596 (2002).
34. Naumov, A. V., Tsyboulski, D. A., Bachilo, S. M. & Weisman, R. B. Length-dependent optical properties of single-walled carbon nanotube samples. *Chem. Phys.* **422**, 255–263 (2013).
35. Cambré, S. *et al.* Luminescence Properties of Individual Empty and Water-Filled Single-Walled Carbon Nanotubes. *ACS Nano* **6**, 2649–2655 (2012).
36. Arnold, M. S., Green, A. A., Hulvat, J. F., Stupp, S. I. & Hersam, M. C. Sorting carbon nanotubes by electronic structure using density differentiation. *Nat. Nanotechnol.* **1**, 60–65 (2006).
37. Liu, H., Nishide, D., Tanaka, T. & Kataura, H. Large-scale single-chirality separation of single-wall carbon nanotubes by simple gel chromatography. *Nat. Commun.* **2**, 309 (2011).
38. Krupke, R., Hennrich, F., v. Löhneysen, H. & Kappes, M. M. Separation of Metallic from Semiconducting Single-Walled Carbon Nanotubes. *Science* **301**, 344–347 (2003).
39. Fagan, J. A. Aqueous two-polymer phase extraction of single-wall carbon nanotubes using surfactants. *Nanoscale Adv.* **1**, 3307–3324 (2019).
40. Khripin, C. Y., Fagan, J. A. & Zheng, M. Spontaneous partition of carbon nanotubes in polymer-modified aqueous phases. *J. Am. Chem. Soc.* **135**, 6822–6825 (2013).
41. Fagan, J. A. *et al.* Isolation of specific small-diameter single-wall carbon nanotube species via aqueous two-phase extraction. *Adv. Mater.* **26**, 2800–2804 (2014).
42. Subbaiyan, N. K. *et al.* Role of Surfactants and Salt in Aqueous Two-Phase Separation of Carbon Nanotubes toward Simple Chirality Isolation. *ACS Nano* **8**, 1619–1628 (2014).
43. Li, H., Gordeev, G., Garrity, O., Reich, S. & Flavel, B. S. Separation of Small-Diameter Single-Walled Carbon Nanotubes in One to Three Steps with Aqueous Two-Phase Extraction. *ACS Nano* **13**, 2567–2578 (2019).

44. Li, H. *et al.* Separation of Specific Single-Enantiomer Single-Wall Carbon Nanotubes in the Large-Diameter Regime. *ACS Nano* **14**, 948–963 (2020).
45. Wei, L., Flavel, B. S., Li, W., Krupke, R. & Chen, Y. Exploring the upper limit of single-walled carbon nanotube purity by multiple-cycle aqueous two-phase separation. *Nanoscale* **9**, 11640–11646 (2017).
46. Samanta, S. K. *et al.* Conjugated polymer-Assisted dispersion of single-wall carbon nanotubes: The power of polymer wrapping. *Acc. Chem. Res.* **47**, 2446–2456 (2014).
47. Nish, A., Hwang, J. Y., Doig, J. & Nicholas, R. J. Highly selective dispersion of single-walled carbon nanotubes using aromatic polymers. *Nat. Nanotechnol.* **2**, 640–646 (2007).
48. Hwang, J.-Y. *et al.* Polymer Structure and Solvent Effects on the Selective Dispersion of Single-Walled Carbon Nanotubes. *J. Am. Chem. Soc.* **130**, 3543–3553 (2008).
49. Gomulya, W. *et al.* Semiconducting single-walled carbon nanotubes on demand by polymer wrapping. *Adv. Mater.* **25**, 2948–2956 (2013).
50. Hennrich, F. *et al.* Length-Sorted, Large-Diameter, Polyfluorene-Wrapped Semiconducting Single-Walled Carbon Nanotubes for High-Density, Short-Channel Transistors. *ACS Nano* **10**, 1888–1895 (2016).
51. Derenskyi, V. *et al.* Semiconducting SWNTs sorted by polymer wrapping: How pure are they? *Appl. Phys. Lett.* **112** (2018).
52. Brohmann, M. *et al.* Temperature-Dependent Charge Transport in Polymer-Sorted Semiconducting Carbon Nanotube Networks with Different Diameter Distributions. *J. Phys. Chem. C* **122**, 19886–19896 (2018).
53. Lemasson, F. *et al.* Polymer Library Comprising Fluorene and Carbazole Homo- and Copolymers for Selective Single-Walled Carbon Nanotubes Extraction. *Macromolecules* **45**, 713–722 (2011).
54. Jiang, H., Taranekar, P., Reynolds, J. R. & Schanze, K. S. Conjugated polyelectrolytes: Synthesis, photophysics, and applications. *Angew. Chem. Int. Ed.* **48**, 4300–4316 (2009).

55. Kang, Y. K. *et al.* Helical wrapping of single-walled carbon nanotubes by water soluble poly(*p*-phenyleneethynylene). *Nano Lett.* **9**, 1414–1418 (2009).
56. Deria, P. *et al.* Single-handed helical wrapping of single-walled carbon nanotubes by chiral, ionic, semiconducting polymers. *J. Am. Chem. Soc.* **135**, 16220–16234 (2013).
57. Balcı Leinen, M. *et al.* Doping-Dependent Energy Transfer from Conjugated Polyelectrolytes to (6,5) Single-Walled Carbon Nanotubes. *J. Phys. Chem. C* **123**, 22680–22689 (2019).
58. Gao, J., Loi, M. A., Carvalho, E. J. F. & Dos Santos, M. C. Selective Wrapping and Supramolecular Structures of Polyfluorene-Carbon Nanotube Hybrids. *ACS Nano* **5**, 3993–3999 (2011).
59. Von Bargen, C. D. *et al.* Origins of the helical wrapping of phenyleneethynylene polymers about single-walled carbon nanotubes. *J. Phys. Chem. B* **117**, 12953–12965 (2013).
60. Jakubka, F. *et al.* Effect of polymer molecular weight and solution parameters on selective dispersion of single-walled carbon nanotubes. *ACS Macro Lett.* **1**, 815–819 (2012).
61. Ding, J., Li, Z., Lefebvre, J., Du, X. & Malenfant, P. R. L. Mechanistic Consideration of pH Effect on the Enrichment of Semiconducting SWCNTs by Conjugated Polymer Extraction. *J. Phys. Chem. C* **120**, 21946–21954 (2016).
62. Li, Z., Ding, J., Lefebvre, J. & Malenfant, P. R. L. Dopant-Modulated Conjugated Polymer Enrichment of Semiconducting SWCNTs. *ACS Omega* **3**, 3413–3419 (2018).
63. Ozawa, H., Ide, N., Fujigaya, T., Niidome, Y. & Nakashima, N. One-pot separation of highly enriched (6,5) SWNT using a fluorene-based copolymer. *Chem. Lett.* **40**, 239–241 (2011).
64. Brohmann, M. *et al.* Charge Transport in Mixed Semiconducting Carbon Nanotube Networks with Tailored Mixing Ratios. *ACS Nano* **13**, 7323–7332 (2019).
65. Philip Wong, H. S. & Akinwande, D. *Carbon Nanotube and Graphene Device Physics* (Cambridge University Press, New York, 2010).

66. Byrne, M. T. & Gun'ko, Y. Recent Advances in Research on Carbon Nanotube-Polymer Composites. *Adv. Mater.* **22**, 1672–1688 (2010).
67. Yu, L., Shearer, C. & Shapter, J. Recent Development of Carbon Nanotube Transparent Conductive Films. *Chem. Rev.* **116**, 13413–13453 (2016).
68. Srivastava, N., Hong, L., Kreupl, F. & Banerjee, K. On the Applicability of Single-Walled Carbon Nanotubes as VLSI Interconnects. *IEEE Trans. Nanotechnol.* **8**, 542–559 (2009).
69. Krainov, I. V. *et al.* Giant Magnetoresistance in Carbon Nanotubes with Single-Molecule Magnets TbPc₂. *ACS Nano* **11**, 6868–6880 (2017).
70. Schießl, S. P. *et al.* Modeling carrier density dependent charge transport in semiconducting carbon nanotube networks. *Phys. Rev. Mater.* **1**, 046003 (2017).
71. Statz, M. *et al.* Charge and Thermoelectric Transport in Polymer-Sorted Semiconducting Single-Walled Carbon Nanotube Networks. *ACS Nano* **14**, 15552–15565 (2020).
72. Yu, P. Y. & Cardona, M. *Fundamentals of Semiconductors* (Springer, Berlin, 2005).
73. Reich, S., Thomsen, C. & Maultzsch, J. *Carbon Nanotubes* (Wiley VCH, Weinheim, 2004).
74. Blancon, J. C. *et al.* Direct measurement of the absolute absorption spectrum of individual semiconducting single-wall carbon nanotubes. *Nat. Commun.* **4**, 2542 (2013).
75. Dresselhaus, M. S., Dresselhaus, G., Saito, R. & Jorio, A. Exciton photophysics of carbon nanotubes. *Annu. Rev. Phys. Chem.* **58**, 719–747 (2007).
76. Spataru, C. D., Ismail-Beigi, S., Benedict, L. X. & Louie, S. G. Excitonic effects and optical spectra of single-walled carbon nanotubes. *Phys. Rev. Lett.* **92**, 077402 (2004).
77. Weisman, R. B. & Bachilo, S. M. Dependence of optical transition energies on structure for single-walled carbon nanotubes in aqueous suspension: An empirical Kataura plot. *Nano Lett.* **3**, 1235–1238 (2003).

78. Chernikov, A. *et al.* Exciton binding energy and nonhydrogenic Rydberg series in monolayer WS₂. *Phys. Rev. Lett.* **113**, 076802 (2014).
79. Raja, A. *et al.* Coulomb engineering of the bandgap and excitons in two-dimensional materials. *Nat. Commun.* **8**, 15251 (2017).
80. Lefebvre, J. & Finnie, P. Excited Excitonic States in Single-Walled Carbon Nanotubes. *Nano Lett.* **8**, 1890–1895 (2008).
81. Wang, F., Dukovic, G., Brus, L. E. & Heinz, T. F. The Optical Resonances in Carbon Nanotubes Arise from Excitons. *Science* **308**, 838–841 (2005).
82. Maultzsch, J. *et al.* Exciton binding energies in carbon nanotubes from two-photon photoluminescence. *Phys. Rev. B* **72**, 241402 (2005).
83. Zhao, H. & Mazumdar, S. Electron-electron interaction effects on the optical excitations of semiconducting single-walled carbon nanotubes. *Phys. Rev. Lett.* **93**, 157402 (2004).
84. Mortimer, I. B. & Nicholas, R. J. Role of bright and dark excitons in the temperature-dependent photoluminescence of carbon nanotubes. *Phys. Rev. Lett.* **98**, 027404 (2007).
85. Matsunaga, R., Matsuda, K. & Kanemitsu, Y. Evidence for dark excitons in a single carbon nanotube due to the Aharonov-Bohm effect. *Phys. Rev. Lett.* **101**, 147404 (2008).
86. Spataru, C. D., Ismail-Beigi, S., Capaz, R. B. & Louie, S. G. Theory and ab initio calculation of radiative lifetime of excitons in semiconducting carbon nanotubes. *Phys. Rev. Lett.* **95**, 247402 (2005).
87. Blackburn, J. L., Holt, J. M., Irurzun, V. M., Resasco, D. E. & Rumbles, G. Confirmation of K-momentum dark exciton vibronic sidebands using ¹³C-labeled, highly enriched (6,5) single-walled carbon nanotubes. *Nano Lett.* **12**, 1398–1403 (2012).
88. Kadria-Vili, Y., Bachilo, S. M., Blackburn, J. L. & Weisman, R. B. Photoluminescence Side Band Spectroscopy of Individual Single-Walled Carbon Nanotubes. *J. Phys. Chem. C* **120**, 23898–23904 (2016).

89. Capaz, R. B., Spataru, C. D., Ismail-Beigi, S. & Louie, S. G. Excitons in carbon nanotubes: Diameter and chirality trends. *Phys. Status Solidi B* **244**, 4016–4020 (2007).
90. Tretiak, S. Triplet State Absorption in Carbon Nanotubes: A TD-DFT Study. *Nano Lett.* **7**, 2201–2206 (2007).
91. Kim, Y. *et al.* Hidden Fine Structure of Quantum Defects Revealed by Single Carbon Nanotube Magneto-Photoluminescence. *ACS Nano* **14**, 3451–3460 (2020).
92. Lin, C. W., Bachilo, S. M. & Weisman, R. B. Delayed Fluorescence from Carbon Nanotubes through Singlet Oxygen-Sensitized Triplet Excitons. *J. Am. Chem. Soc.* **142**, 21189–21196 (2020).
93. Palotás, J. *et al.* Incidence of Quantum Confinement on Dark Triplet Excitons in Carbon Nanotubes. *ACS Nano* **14**, 11254–11261 (2020).
94. Park, J., Deria, P. & Therien, M. J. Dynamics and transient absorption spectral signatures of the single-wall carbon nanotube electronically excited triplet state. *J. Am. Chem. Soc.* **133**, 17156–17159 (2011).
95. Mohite, A. D., Santos, T. S., Moodera, J. S. & Alphenaar, B. W. Observation of the triplet exciton in EuS-coated single-walled nanotubes. *Nat. Nanotechnol.* **4**, 425–429 (2009).
96. Harrah, D. M. *et al.* Intensity-Dependent Exciton Dynamics of (6,5) Single-Walled Carbon Nanotubes: Momentum Selection Rules, Diffusion, and Nonlinear Interactions. *ACS Nano* **5**, 9898–9906 (2011).
97. Jones, M. *et al.* Analysis of photoluminescence from solubilized single-walled carbon nanotubes. *Phys. Rev. B* **71**, 115426 (2005).
98. Charlier, J.-C. Defects in Carbon Nanotubes. *Acc. Chem. Res.* **35**, 1063–1069 (2002).
99. Cagnet, L. *et al.* Stepwise Quenching of Exciton Fluorescence in Carbon Nanotubes by Single-Molecule Reactions. *Science* **316**, 1465–1468 (2007).
100. Doyle, C. D., Rocha, J.-D. R., Weisman, R. B. & Tour, J. M. Structure-Dependent Reactivity of Semiconducting Single-Walled Carbon Nanotubes with Benzene-diazonium Salts. *J. Am. Chem. Soc.* **130**, 6795–6800 (2008).

101. Hertel, T., Himmelein, S., Ackermann, T., Stich, D. & Crochet, J. Diffusion limited photoluminescence quantum yields in 1-D semiconductors: Single-wall carbon nanotubes. *ACS Nano* **4**, 7161–7168 (2010).
102. Piao, Y. *et al.* Brightening of carbon nanotube photoluminescence through the incorporation of sp^3 defects. *Nat. Chem.* **5**, 840–845 (2013).
103. Hartmann, N. F. *et al.* Photoluminescence imaging of solitary dopant sites in covalently doped single-wall carbon nanotubes. *Nanoscale* **7**, 20521–20530 (2015).
104. Hartmann, N. F. *et al.* Photoluminescence Dynamics of Aryl sp^3 Defect States in Single-Walled Carbon Nanotubes. *ACS Nano* **10**, 8355–8365 (2016).
105. He, X. *et al.* Solvent- and Wavelength-Dependent Photoluminescence Relaxation Dynamics of Carbon Nanotube sp^3 Defect States. *ACS Nano* **12**, 8060–8070 (2018).
106. Kilina, S., Ramirez, J. & Tretiak, S. Brightening of the lowest exciton in carbon nanotubes via chemical functionalization. *Nano Lett.* **12**, 2306–2312 (2012).
107. Gifford, B. J., Kilina, S., Htoon, H., Doorn, S. K. & Tretiak, S. Exciton Localization and Optical Emission in Aryl-Functionalized Carbon Nanotubes. *J. Phys. Chem. C* **122**, 1828–1838 (2018).
108. Gifford, B. J. *et al.* Optical Effects of Divalent Functionalization of Carbon Nanotubes. *Chem. Mater.* **31**, 6950–6961 (2019).
109. Ishii, A., Machiya, H. & Kato, Y. High Efficiency Dark-to-Bright Exciton Conversion in Carbon Nanotubes. *Phys. Rev. X* **9**, 041048 (2019).
110. Crochet, J. J. *et al.* Disorder limited exciton transport in colloidal single-wall carbon nanotubes. *Nano Lett.* **12**, 5091–5096 (2012).
111. Srivastava, A. & Kono, J. Diffusion-limited exciton-exciton annihilation in single-walled carbon nanotubes: A time-dependent analysis. *Phys. Rev. B* **79**, 205407 (2009).
112. Harrah, D. M. & Swan, A. K. The Role of Length and Defects on Optical Quantum Efficiency and Exciton Decay Dynamics in Single-Walled Carbon Nanotubes. *ACS Nano* **5**, 647–655 (2011).

113. Kim, M. *et al.* Fluorescent Carbon Nanotube Defects Manifest Substantial Vibrational Reorganization. *J. Phys. Chem. C* **120**, 11268–11276 (2016).
114. Streit, J. K., Bachilo, S. M., Ghosh, S., Lin, C. W. & Weisman, R. B. Directly measured optical absorption cross sections for structure-selected single-walled carbon nanotubes. *Nano Lett.* **14**, 1530–1536 (2014).
115. Miyauchi, Y. *et al.* Brightening of excitons in carbon nanotubes on dimensionality modification. *Nat. Photonics* **7**, 715–719 (2013).
116. Perebeinos, V., Tersoff, J. & Avouris, P. Radiative Lifetime of Excitons in Carbon Nanotubes. *Nano Lett.* **5**, 2495–2499 (2005).
117. He, X. *et al.* Intrinsic Limits of Defect-State Photoluminescence Dynamics in Functionalized Carbon Nanotubes. *Nanoscale* **11**, 9125–9132 (2019).
118. Perebeinos, V. & Avouris, P. Phonon and electronic nonradiative decay mechanisms of excitons in carbon nanotubes. *Phys. Rev. Lett.* **101**, 057401 (2008).
119. Aharoni, A., Oron, D., Banin, U., Rabani, E. & Jortner, J. Long-range electronic-to-vibrational energy transfer from nanocrystals to their surrounding matrix environment. *Phys. Rev. Lett.* **100**, 057404 (2008).
120. Wen, Q. *et al.* Impact of D₂O/H₂O Solvent Exchange on the Emission of HgTe and CdTe Quantum Dots: Polaron and Energy Transfer Effects. *ACS Nano* **10**, 4301–4311 (2016).
121. Ma, X. *et al.* Electronic structure and chemical nature of oxygen dopant states in carbon nanotubes. *ACS Nano* **8**, 10782–10789 (2014).
122. Kwon, H. *et al.* Probing Trions at Chemically Tailored Trapping Defects. *ACS Cent. Sci.* **5**, 1786–1794 (2019).
123. Nutz, M. *et al.* Photon Correlation Spectroscopy of Luminescent Quantum Defects in Carbon Nanotubes. *Nano Lett.* **19**, 7078–7084 (2019).
124. Kim, Y. *et al.* Photoluminescence Intensity Fluctuations and Temperature-Dependent Decay Dynamics of Individual Carbon Nanotube sp³ Defects. *J. Phys. Chem. Lett.* **10**, 1423–1430 (2019).

125. Ma, X., Hartmann, N. F., Baldwin, J. K., Doorn, S. K. & Htoon, H. Room-temperature single-photon generation from solitary dopants of carbon nanotubes. *Nat. Nanotechnol.* **10**, 671–675 (2015).
126. Iwamura, M. *et al.* Nonlinear Photoluminescence Spectroscopy of Carbon Nanotubes with Localized Exciton States. *ACS Nano* **8**, 11254–11260 (2014).
127. Saha, A. *et al.* Narrow-band single-photon emission through selective aryl functionalization of zigzag carbon nanotubes. *Nat. Chem.* **10**, 1089–1095 (2018).
128. He, X. *et al.* Low-Temperature Single Carbon Nanotube Spectroscopy of sp^3 Quantum Defects. *ACS Nano* **11**, 10785–10796 (2017).
129. Kwon, H. *et al.* Molecularly Tunable Fluorescent Quantum Defects. *J. Am. Chem. Soc.* **138**, 6878–6885 (2016).
130. Przypis, L. *et al.* Enhancing near-infrared photoluminescence from single-walled carbon nanotubes by defect-engineering using benzoyl peroxide. *Sci. Rep.* **10**, 19877 (2020).
131. He, X., Kevlishvili, I., Murcek, K., Liu, P. & Star, A. $[2\pi + 2\pi]$ Photocycloaddition of Enones to Single-Walled Carbon Nanotubes Creates Fluorescent Quantum Defects. *ACS Nano* **15**, 4833–4844 (2021).
132. Wu, X., Kim, M., Kwon, H. & Wang, Y. Photochemical Creation of Fluorescent Quantum Defects in Semiconducting Carbon Nanotube Hosts. *Angew. Chem. Int. Ed.* **57**, 648–653 (2018).
133. Zheng, Y., Bachilo, S. M. & Weisman, R. B. Photoexcited Aromatic Reactants Give Multicolor Carbon Nanotube Fluorescence from Quantum Defects. *ACS Nano* **14**, 715–723 (2020).
134. Lin, C. W. *et al.* Creating fluorescent quantum defects in carbon nanotubes using hypochlorite and light. *Nat. Commun.* **10**, 2874 (2019).
135. Janas, D. Perfectly imperfect: a review of chemical tools for exciton engineering in single-walled carbon nanotubes. *Mater. Horiz.* **7**, 2860–2881 (2020).
136. Usrey, M. L., Lippmann, E. S. & Strano, M. S. Evidence for a Two-Step Mechanism in Electronically Selective Single-Walled Carbon Nanotube Reactions. *J. Am. Chem. Soc.* **127**, 16129–16135 (2005).

137. Schmidt, G., Gallon, S., Esnouf, S., Bourgoïn, J. P. & Chenevier, P. Mechanism of the coupling of diazonium to single-walled carbon nanotubes and its consequences. *Chem. Eur. J.* **15**, 2101–2110 (2009).
138. Gomberg, M. & Bachmann, W. E. The Synthesis Of Biaryl Compounds By Means Of The Diazo Reaction. *J. Am. Chem. Soc.* **46**, 2339–2343 (1924).
139. Powell, L. R., Piao, Y. & Wang, Y. Optical Excitation of Carbon Nanotubes Drives Localized Diazonium Reactions. *J. Phys. Chem. Lett.* **7**, 3690–3694 (2016).
140. Powell, L. R., Kim, M. & Wang, Y. Chirality-Selective Functionalization of Semiconducting Carbon Nanotubes with a Reactivity-Switchable Molecule. *J. Am. Chem. Soc.* **139**, 12533–12540 (2017).
141. Luo, H. B. *et al.* One-Pot, Large-Scale Synthesis of Organic Color Center-Tailored Semiconducting Carbon Nanotubes. *ACS Nano* **13**, 8417–8424 (2019).
142. Setaro, A. *et al.* Preserving π -conjugation in covalently functionalized carbon nanotubes for optoelectronic applications. *Nat. Commun.* **8**, 14281 (2017).
143. Godin, A. G. *et al.* Photoswitchable single-walled carbon nanotubes for super-resolution microscopy in the near-infrared. *Sci. Rep.* **5**, eaax1166 (2019).
144. Liu, J.-M. *Photonic Devices* (Cambridge University Press, New York, 2005).
145. Kogelnik, H. in *Guided Wave Optoelectronics* (ed Tamir, T.) 7–88 (Springer, Berlin, 1988).
146. Calzado, E. M., Villalvilla, J. M., Boj, P. G., Quintana, J. A. & Diaz-Garcia, M. A. Tuneability of amplified spontaneous emission through control of the thickness in organic-based waveguides. *J. Appl. Phys.* **97**, 093103 (2005).
147. Degnan, J. J. The Waveguide Laser: A Review. *Appl. Phys.* **11**, 1–33 (1976).
148. Khasminskaya, S. *et al.* Fully integrated quantum photonic circuit with an electrically driven light source. *Nat. Photonics* **10**, 727–732 (2016).
149. Yang, C. & Lunt, R. R. Limits of Visibly Transparent Luminescent Solar Concentrators. *Adv. Optical Mater.* **5**, 1600851 (2017).

150. Mateen, F., Lee, S. Y. & Hong, S.-K. Luminescent solar concentrators based on thermally activated delayed fluorescence dyes. *J. Mater. Chem. A* **8**, 3708–3716 (2020).
151. Roncali, J. Luminescent Solar Collectors: Quo Vadis? *Adv. Energy Mater.* **10**, 2001907 (2020).
152. Gauffrès, E. *et al.* Optical gain in carbon nanotubes. *Appl. Phys. Lett.* **96**, 231105 (2010).
153. Gauffrès, E. *et al.* Light Emission in Silicon from Carbon Nanotubes. *ACS Nano* **6**, 3813–3819 (2012).
154. Imamura, S., Watahiki, R., Miura, R., Shimada, T. & Kato, Y. K. Optical control of individual carbon nanotube light emitters by spectral double resonance in silicon microdisk resonators. *Appl. Phys. Lett.* **102**, 161102 (2013).
155. Khasminskaya, S., Pyatkov, F., Flavel, B. S., Pernice, W. H. & Krupke, R. Waveguide-integrated light-emitting carbon nanotubes. *Adv. Mater.* **26**, 3465–3472 (2014).
156. He, X. *et al.* Carbon nanotubes as emerging quantum-light sources. *Nat. Mater.* **17**, 663–670 (2018).
157. Shaklee, K. L., Nahory, R. E. & Leheny, R. F. Optical Gain in Semiconductors. *J. Lumin.* **7**, 284–309 (1973).
158. Zaumseil, J. & Sirringhaus, H. Electron and Ambipolar Transport in Organic Field-Effect Transistors. *Chem. Rev.* **107**, 1296–1323 (2007).
159. Zaumseil, J. Recent Developments and Novel Applications of Thin Film, Light-Emitting Transistors. *Adv. Funct. Mater.* **30**, 1905269 (2019).
160. Choi, H. H., Cho, K., Frisbie, C. D., Sirringhaus, H. & Podzorov, V. Critical assessment of charge mobility extraction in FETs. *Nat. Mater.* **17**, 2–7 (2017).
161. Kang, M. S. & Frisbie, C. D. A pedagogical perspective on ambipolar FETs. *ChemPhysChem* **14**, 1547–1552 (2013).
162. Schmechel, R., Ahles, M. & von Seggern, H. A pentacene ambipolar transistor: Experiment and theory. *J. Appl. Phys.* **98**, 084511 (2005).

163. Jakubka, F., Grimm, S. B., Zakharko, Y., Gannott, F. & Zaumseil, J. Trion Electroluminescence from Semiconducting Carbon Nanotubes. *ACS Nano* **8**, 8477–8486 (2014).
164. Held, M. *et al.* Ultrastrong Coupling of Electrically Pumped Near-Infrared Exciton-Polaritons in High Mobility Polymers. *Adv. Optical Mater.* **6**, 1700962 (2018).
165. Zhang, Y. J., Oka, T., Suzuki, R., Ye, J. T. & Iwasa, Y. Electrically Switchable Chiral Light-Emitting Transistor. *Science* **344**, 725–728 (2014).
166. Schornbaum, J. *et al.* Light-Emitting Quantum Dot Transistors: Emission at High Charge Carrier Densities. *Nano Lett.* **15**, 1822–1828 (2015).
167. Rother, M., Schießl, S. P., Zakharko, Y., Gannott, F. & Zaumseil, J. Understanding Charge Transport in Mixed Networks of Semiconducting Carbon Nanotubes. *ACS Appl. Mater. Interfaces* **8**, 5571–5579 (2016).
168. Zakharko, Y. *et al.* On-Demand Coupling of Electrically Generated Excitons with Surface Plasmons via Voltage-Controlled Emission Zone Position. *ACS Photonics* **3**, 1–7 (2016).
169. Berger, F. J. *et al.* Brightening of Long, Polymer-Wrapped Carbon Nanotubes by sp^3 Functionalization in Organic Solvents. *ACS Nano* **13**, 9259–9269 (2019).
170. Seber, G. *et al.* Covalent Modification of Highly Ordered Pyrolytic Graphite with a Stable Organic Free Radical by Using Diazonium Chemistry. *Chem. Eur. J.* **23**, 1415–1421 (2017).
171. Rother, M. *et al.* Aerosol-Jet Printing of Polymer-Sorted (6,5) Carbon Nanotubes for Field-Effect Transistors with High Reproducibility. *Adv. Electron. Mater.*, 1700080 (2017).
172. De Mello, J. C., Wittman, H. F. & Friend, R. H. An Improved Experimental Determination of External Photoluminescence Quantum Efficiency. *Adv. Mater.* **9**, 230–232 (1997).
173. Ahn, T. S., Al-Kaysi, R. O., Muller, A. M., Wentz, K. M. & Bardeen, C. J. Self-absorption correction for solid-state photoluminescence quantum yields obtained from integrating sphere measurements. *Rev. Sci. Instrum.* **78**, 086105 (2007).

174. Dal Negro, L., Bettotti, P., Cazzanelli, M., Pacifici, D. & Pavesi, L. Applicability conditions and experimental analysis of the variable stripe length method for gain measurements. *Opt. Commun.* **229**, 337–348 (2004).
175. Powell, L. R., Piao, Y., Ng, A. L. & Wang, Y. Channeling Excitons to Emissive Defect Sites in Carbon Nanotube Semiconductors beyond the Dilute Regime. *J. Phys. Chem. Lett.* **9**, 2803–2807 (2018).
176. Zhang, Y. *et al.* Propagative Sidewall Alkylcarboxylation that Induces Red-Shifted Near-IR Photoluminescence in Single-Walled Carbon Nanotubes. *J. Phys. Chem. Lett.* **4**, 826–830 (2013).
177. Brozena, A. H., Leeds, J. D., Zhang, Y., Fourkas, J. T. & Wang, Y. Controlled Defects in Semiconducting Carbon Nanotubes Promote Efficient Generation and Luminescence of Trions. *ACS Nano* **8**, 4239–4247 (2014).
178. Yomogida, Y. *et al.* Industrial-scale separation of high-purity single-chirality single-wall carbon nanotubes for biological imaging. *Nat. Commun.* **7**, 12056 (2016).
179. Graf, A., Tropf, L., Zakharko, Y., Zaumseil, J. & Gather, M. C. Near-infrared exciton-polaritons in strongly coupled single-walled carbon nanotube microcavities. *Nat. Commun.* **7**, 13078 (2016).
180. Wang, J. *et al.* Role of Defects as Exciton Quenching Sites in Carbon Nanotube Photovoltaics. *J. Phys. Chem. C* **121**, 8310–8318 (2017).
181. Beadle, J. R., Korzeniowski, S. H., Rosenberg, D. E., Garcia-Slanga, B. J. & Gokel, G. W. Phase-Transfer-Catalyzed Gomberg-Bachmann Synthesis of Unsymmetrical Biarenes: A Survey of Catalysts and Substrates. *J. Org. Chem.* **49**, 1594–1603 (1984).
182. Dyke, C. A., Stewart, M. P., Maya, F. & Tour, J. M. Diazonium-Based Functionalization of Carbon Nanotubes: XPS and GC-MS Analysis and Mechanistic Implications. *Synlett*, 155–160 (2004).
183. Gifford, B. J. *et al.* Mod(n-m,3) Dependence of Defect-State Emission Bands in Aryl-Functionalized Carbon Nanotubes. *Nano Lett.* **19**, 8503–8509 (2019).

184. Danné, N. *et al.* Ultrashort Carbon Nanotubes That Fluoresce Brightly in the Near-Infrared. *ACS Nano* **12**, 6059–6065 (2018).
185. Wu, X., Kim, M., Qu, H. & Wang, Y. Single-defect spectroscopy in the shortwave infrared. *Nat. Commun.* **10**, 2672 (2019).
186. Hofmann, M. S. *et al.* Bright, long-lived and coherent excitons in carbon nanotube quantum dots. *Nat. Nanotechnol.* **8**, 502–505 (2013).
187. Dresselhaus, M. S., Dresselhaus, G., Saito, R. & Jorio, A. Raman spectroscopy of carbon nanotubes. *Phys. Rep.* **409**, 47–99 (2005).
188. Dresselhaus, M. S., Jorio, A., Souza Filho, A. G. & Saito, R. Defect characterization in graphene and carbon nanotubes using Raman spectroscopy. *Phil. Trans. R. Soc. A* **368**, 5355–5377 (2010).
189. Piscanec, S., Lazzeri, M., Robertson, J., Ferrari, A. C. & Mauri, F. Optical phonons in carbon nanotubes: Kohn anomalies, Peierls distortions, and dynamic effects. *Phys. Rev. B* **75**, 035427 (2007).
190. Knight, D. S. & White, W. B. Characterization of diamond films by Raman spectroscopy. *J. Mater. Res.* **4**, 385–393 (1989).
191. Cançado, L. G. *et al.* General equation for the determination of the crystallite size L_a of nanographite by Raman spectroscopy. *Appl. Phys. Lett.* **88**, 163106 (2006).
192. Kalbacova, J. *et al.* Defect Evolution of Ion-Exposed Single-Wall Carbon Nanotubes. *J. Phys. Chem. C* **123**, 2496–2505 (2019).
193. Crochet, J., Clemens, M. & Hertel, T. Quantum Yield Heterogeneities of Aqueous Single-Wall Carbon Nanotube Suspensions. *J. Am. Chem. Soc.* **129**, 8058–8059 (2007).
194. Schöppler, F. *et al.* Molar Extinction Coefficient of Single-Wall Carbon Nanotubes. *J. Phys. Chem. C* **115**, 14682–14686 (2011).
195. Berger, F. J. *et al.* Interaction of Luminescent Defects in Carbon Nanotubes with Covalently Attached Stable Organic Radicals. *ACS Nano* **15**, 5147–5157 (2021).

196. Kwon, H. *et al.* Optical Probing of Local pH and Temperature in Complex Fluids with Covalently Functionalized, Semiconducting Carbon Nanotubes. *J. Phys. Chem. C* **119**, 3733–3739 (2015).
197. Shiraki, T., Onitsuka, H., Shiraishi, T. & Nakashima, N. Near infrared photoluminescence modulation of single-walled carbon nanotubes based on a molecular recognition approach. *Chem. Commun.* **52**, 12972–12975 (2016).
198. Onitsuka, H., Fujigaya, T., Nakashima, N. & Shiraki, T. Control of the Near Infrared Photoluminescence of Locally Functionalized Single-Walled Carbon Nanotubes via Doping by Azacrown-Ether Modification. *Chem. Eur. J.* **24**, 9393–9398 (2018).
199. Schnee, M. *et al.* Quantum transport in carbon nanotubes covalently functionalized with magnetic molecules. *Phys. Status Solidi B* **253**, 2424–2427 (2016).
200. Marangon, I. *et al.* Covalent Functionalization of Multi-walled Carbon Nanotubes with a Gadolinium Chelate for Efficient T_1 -Weighted Magnetic Resonance Imaging. *Adv. Funct. Mater.* **24**, 7173–7186 (2014).
201. Ncube, S. *et al.* Kondo effect and enhanced magnetic properties in gadolinium functionalized carbon nanotube supramolecular complex. *Sci. Rep.* **8**, 8057 (2018).
202. Bader, S. D. & Parkin, S. S. P. Spintronics. *Annu. Rev. Condens. Matter Phys.* **1**, 71–88 (2010).
203. Urdampilleta, M., Klyatskaya, S., Cleuziou, J. P., Ruben, M. & Wernsdorfer, W. Supramolecular spin valves. *Nat. Mater.* **10**, 502–506 (2011).
204. Ballester, M. Inert Free Radicals (IFR): A Unique Trivalent Carbon Species. *Acc. Chem. Res.* **18**, 380–387 (1985).
205. Rajca, A. *et al.* Organic radical contrast agents for magnetic resonance imaging. *J. Am. Chem. Soc.* **134**, 15724–15727 (2012).
206. Kuemmeth, F., Churchill, H. O. H., Herring, P. K. & Marcus, C. M. Carbon nanotubes for coherent spintronics. *Mater. Today* **13**, 18–26 (2010).
207. Seber, G. *et al.* Synergistic Exploitation of the Superoxide Scavenger Properties of Reduced Graphene Oxide and a Trityl Organic Radical for the Impedimetric Sensing of Xanthine. *Adv. Mater. Interfaces* **5**, 1701072 (2018).

208. Zaka, M. *et al.* Electron Paramagnetic Resonance Investigation of Purified Catalyst-free Single-Walled Carbon Nanotubes. *ACS Nano* **4**, 7708–7716 (2010).
209. Armet, O. *et al.* Inert Carbon Free Radicals. 8. Polychlorotriphenylmethyl Radicals. Synthesis, Structure, and Spin-Density Distribution. *J. Phys. Chem.* **91**, 5608–5616 (1987).
210. Weil, J. A. & Bolton, J. R. *Electron Paramagnetic Resonance* (John Wiley & Sons, Hoboken, 2007).
211. Reuel, N. F., Dupont, A., Thouvenin, O., Lamb, D. C. & Strano, M. S. Three-Dimensional Tracking of Carbon Nanotubes within Living Cells. *ACS Nano* **6**, 5420–5428 (2012).
212. Lohmann, S. H. *et al.* sp^3 -Functionalization of Single-Walled Carbon Nanotubes Creates Localized Spins. *ACS Nano* **14**, 17675–17682 (2020).
213. Tsoufis, T. *et al.* Direct observation of spin-injection in tyrosinate-functionalized single-wall carbon nanotubes. *Carbon* **67**, 424–433 (2014).
214. Ballester, M. *et al.* Inert Carbon Free Radicals. 5. Perchloro-9-phenylfluorenyl Radical Series. *J. Org. Chem.* **49**, 770–778 (1984).
215. Fox, M. A., Gaillard, E. & Chen, C.-C. Photochemistry of Stable Free Radicals: The Photolysis of Perchlorotriphenylmethyl Radicals. *J. Am. Chem. Soc.* **109**, 7088–7094 (1987).
216. Lakowicz, J. R. *Principles of Fluorescence Spectroscopy* (Springer, New York, 2006).
217. Dexter, D. L. A Theory of Sensitized Luminescence in Solids. *J. Chem. Phys.* **21**, 836–850 (1953).
218. Simão, C. *et al.* A robust molecular platform for non-volatile memory devices with optical and magnetic responses. *Nat. Chem.* **3**, 359–364 (2011).
219. Weller, A. Photoinduced Electron Transfer in Solution: Exciplex and Radical Ion Pair Formation Free Enthalpies and their Solvent Dependence. *Z. Phys. Chem.* **133**, 93–98 (1982).

220. Shiraishi, T., Shiraki, T. & Nakashima, N. Substituent effects on the redox states of locally functionalized single-walled carbon nanotubes revealed by in situ photoluminescence spectroelectrochemistry. *Nanoscale* **9**, 16900–16907 (2017).
221. Souto, M. *et al.* Pressure-Induced Conductivity in a Neutral Nonplanar Spin-Localized Radical. *J. Am. Chem. Soc.* **138**, 11517–11525 (2016).
222. Miller, J. R., Calcaterra, L. T. & Closs, G. L. Intramolecular Long-Distance Electron Transfer in Radical Anions. The Effects of Free Energy and Solvent on the Reaction Rates. *J. Am. Chem. Soc.* **106**, 3047–3049 (1984).
223. Lewis, F. D. *et al.* Distance-Dependent Electron Transfer in DNA Hairpins. *Science* **277**, 673–676 (1997).
224. Yeganeh, S., Wasielewski, M. R. & Ratner, M. A. Enhanced Intersystem Crossing in Three-Spin Systems: A Perturbation Theory Treatment. *J. Am. Chem. Soc.* **131**, 2268–2273 (2009).
225. Giacobbe, E. M. *et al.* Ultrafast Intersystem Crossing and Spin Dynamics of Photoexcited Perylene-3,4:9,10-Bis(dicarboximide) Covalently Linked to a Nitroxide Radical at Fixed Distances. *J. Am. Chem. Soc.* **131**, 3700–3712 (2009).
226. Colvin, M. T. *et al.* Competitive Electron Transfer and Enhanced Intersystem Crossing in Photoexcited Covalent TEMPO-Perylene-3,4:9,10-Bis(dicarboximide) Dyads: Unusual Spin Polarization Resulting from the Radical-Triplet Interaction. *J. Phys. Chem. A* **114**, 1741–1748 (2010).
227. Wang, Z. *et al.* Radical-Enhanced Intersystem Crossing in New Bodipy Derivatives and Application for Efficient Triplet-Triplet Annihilation Upconversion. *J. Am. Chem. Soc.* **139**, 7831–7842 (2017).
228. Dyar, S. M. *et al.* Photogenerated Quartet State Formation in a Compact Ring-Fused Perylene-Nitroxide. *J. Phys. Chem. B* **119**, 13560–13569 (2015).
229. Trerayapiwat, K. J., Lohmann, S. H., Ma, X. & Sharifzadeh, S. Tuning spin-orbit coupling in (6,5) single-walled carbon nanotube doped with sp^3 defects. *J. Appl. Phys.* **129**, 014309 (2021).
230. Stich, D. *et al.* Triplet-triplet exciton dynamics in single-walled carbon nanotubes. *Nat. Photonics* **8**, 139–144 (2013).

231. Ai, N., Walden-Newman, W., Song, Q., Kalliakos, S. & Strauf, S. Suppression of Blinking and Enhanced Exciton Emission from Individual Carbon Nanotubes. *ACS Nano* **5**, 2664–2670 (2011).
232. Orcin-Chaix, L. *et al.* Photostability of Single-Walled Carbon Nanotubes/Polymer Core–Shell Hybrids as Telecom Wavelength Emitters. *ACS Appl. Nano Mater.* **3**, 7291–7296 (2020).
233. Sarpkaya, I. *et al.* Strong Acoustic Phonon Localization in Copolymer-Wrapped Carbon Nanotubes. *ACS Nano* **9**, 6383–6393 (2015).
234. Ma, X. *et al.* Multi-exciton emission from solitary dopant states of carbon nanotubes. *Nanoscale* **9**, 16143–16148 (2017).
235. Arellano, L. M. *et al.* Triplet photosensitizer-nanotube conjugates: synthesis, characterization and photochemistry of charge stabilizing, palladium porphyrin/carbon nanotube conjugates. *Nanoscale* **12**, 9890–9898 (2020).
236. Ratera, I. & Veciana, J. Playing with organic radicals as building blocks for functional molecular materials. *Chem. Soc. Rev.* **41**, 303–349 (2012).
237. Ji, L., Shi, J., Wei, J., Yu, T. & Huang, W. Air-Stable Organic Radicals: New-Generation Materials for Flexible Electronics? *Adv. Mater.* **32**, 1908015 (2020).
238. Settele, S. *et al.* Synthetic control over the binding configuration of luminescent sp^3 -defects in single-walled carbon nanotubes. *Nat. Commun.*, in press (2021).
239. Tan, P. H. *et al.* Photoluminescence spectroscopy of carbon nanotube bundles: Evidence for exciton energy transfer. *Phys. Rev. Lett.* **99**, 137402 (2007).
240. Crochet, J. J., Sau, J. D., Duque, J. G., Doorn, S. K. & Cohen, M. L. Electrodynamic and Excitonic Intertube Interactions in Semiconducting Carbon Nanotube Aggregates. *ACS Nano* **5**, 2611–2618 (2011).
241. Crochet, J. J. *et al.* Free-carrier generation in aggregates of single-wall carbon nanotubes by photoexcitation in the ultraviolet regime. *Phys. Rev. Lett.* **107**, 257402 (2011).
242. Streit, J. K., Bachilo, S. M., Sanchez, S. R., Lin, C. W. & Weisman, R. B. Variance Spectroscopy. *J. Phys. Chem. Lett.* **6**, 3976–3981 (2015).

243. Arias, D. H. *et al.* Effect of nanotube coupling on exciton transport in polymer-free monochiral semiconducting carbon nanotube networks. *Nanoscale* **11**, 21196–21206 (2019).
244. Larsen, B. A. *et al.* Effect of solvent polarity and electrophilicity on quantum yields and solvatochromic shifts of single-walled carbon nanotube photoluminescence. *J. Am. Chem. Soc.* **134**, 12485–12491 (2012).
245. Miyauchi, Y. Photoluminescence studies on exciton photophysics in carbon nanotubes. *J. Mater. Chem. C* **1**, 6499–6521 (2013).
246. Shiraki, T. *et al.* Solvatochromism of near infrared photoluminescence from doped sites of locally functionalized single-walled carbon nanotubes. *Chem. Commun.* **55**, 3662–3665 (2019).
247. Campo, J. *et al.* Optical Property Tuning of Single-Wall Carbon Nanotubes by Endohedral Encapsulation of a Wide Variety of Dielectric Molecules. *ACS Nano* **15**, 2301–2317 (2021).
248. Schweiger, M., Zakharko, Y., Gannott, F., Grimm, S. B. & Zaumseil, J. Photoluminescence enhancement of aligned arrays of single-walled carbon nanotubes by polymer transfer. *Nanoscale* **7**, 16715–16720 (2015).
249. Gaulke, M. *et al.* Low-Temperature Electroluminescence Excitation Mapping of Excitons and Trions in Short-Channel Monochiral Carbon Nanotube Devices. *ACS Nano* **14**, 2709–2717 (2020).
250. Sarpkaya, I. *et al.* Prolonged spontaneous emission and dephasing of localized excitons in air-bridged carbon nanotubes. *Nat. Commun.* **4**, 2152 (2013).
251. Noe, J. C. *et al.* Environmental Electrometry with Luminescent Carbon Nanotubes. *Nano Lett.* **18**, 4136–4140 (2018).
252. Shayan, K. *et al.* Suppression of exciton dephasing in sidewall-functionalized carbon nanotubes embedded into metallo-dielectric antennas. *Nanoscale* **10**, 12631–12638 (2018).
253. Fang, N. *et al.* Hexagonal Boron Nitride As an Ideal Substrate for Carbon Nanotube Photonics. *ACS Photonics* **7**, 1773–1779 (2020).

254. Lüer, L. *et al.* Size and mobility of excitons in (6,5) carbon nanotubes. *Nat. Phys.* **5**, 54–58 (2008).
255. Mann, C. & Hertel, T. 13 nm Exciton Size in (6,5) Single-Wall Carbon Nanotubes. *J. Phys. Chem. Lett.* **7**, 2276–2280 (2016).
256. Wang, F., Dukovic, G., Knoesel, E., Brus, L. E. & Heinz, T. F. Observation of rapid Auger recombination in optically excited semiconducting carbon nanotubes. *Phys. Rev. B* **70**, 241403 (2004).
257. Xiao, Y. F., Nhan, T. Q., Wilson, M. W. & Fraser, J. M. Saturation of the photoluminescence at few-exciton levels in a single-walled carbon nanotube under ultrafast excitation. *Phys. Rev. Lett.* **104**, 017401 (2010).
258. Murakami, Y. & Kono, J. Nonlinear photoluminescence excitation spectroscopy of carbon nanotubes: exploring the upper density limit of one-dimensional excitons. *Phys. Rev. Lett.* **102**, 037401 (2009).
259. Ishii, A., Yoshida, M. & Kato, Y. K. Exciton diffusion, end quenching, and exciton-exciton annihilation in individual air-suspended carbon nanotubes. *Phys. Rev. B* **91**, 125427 (2015).
260. Graf, A., Murawski, C., Zakharko, Y., Zaumseil, J. & Gather, M. C. Infrared Organic Light-Emitting Diodes with Carbon Nanotube Emitters. *Adv. Mater.* **30**, 1706711 (2018).
261. Xu, B., Wu, X., Kim, M., Wang, P. & Wang, Y. Electroluminescence from 4-nitroaryl organic color centers in semiconducting single-wall carbon nanotubes. *J. Appl. Phys.* **129**, 044305 (2021).
262. Wei, X. *et al.* Photoluminescence Quantum Yield of Single-Wall Carbon Nanotubes Corrected for the Photon Reabsorption Effect. *Nano Lett.* **20**, 410–417 (2019).
263. Steiner, M. *et al.* Gate-variable light absorption and emission in a semiconducting carbon nanotube. *Nano Lett.* **9**, 3477–3481 (2009).
264. Eckstein, K. H., Oberndorfer, F., Achsnich, M. M., Schöppler, F. & Hertel, T. Quantifying Doping Levels in Carbon Nanotubes by Optical Spectroscopy. *J. Phys. Chem. C* **123**, 30001–30006 (2019).

265. Hertel, T. *et al.* Intersubband Decay of 1-D Exciton Resonances in Carbon Nanotubes. *Nano Lett.* **8**, 87–91 (2008).
266. Kumamoto, Y. *et al.* Spontaneous exciton dissociation in carbon nanotubes. *Phys. Rev. Lett.* **112**, 117401 (2014).
267. Sykes, M. E. *et al.* Ultrafast Exciton Trapping at sp^3 Quantum Defects in Carbon Nanotubes. *ACS Nano* **13**, 13264–13270 (2019).
268. Georgi, C. *et al.* Photoinduced luminescence blinking and bleaching in individual single-walled carbon nanotubes. *ChemPhysChem* **9**, 1460–1464 (2008).
269. Gerardot, B. D. *et al.* Photon statistics from coupled quantum dots. *Phys. Rev. Lett.* **95**, 137403 (2005).
270. Zorn, N. F. *et al.* Probing Mobile Charge Carriers in Semiconducting Carbon Nanotube Networks by Charge Modulation Spectroscopy. *ACS Nano* **14**, 2412–2423 (2020).
271. Schirowski, M., Hauke, F. & Hirsch, A. Controlling the Degree of Functionalization: In-Depth Quantification and Side-Product Analysis of Diazonium Chemistry on SWCNTs. *Chem. Eur. J.* **25**, 12761–12768 (2019).
272. Wilson, H. *et al.* Electrical Monitoring of sp^3 Defect Formation in Individual Carbon Nanotubes. *J. Phys. Chem. C* **120**, 1971–1976 (2016).
273. Wang, B. *et al.* Defect-Induced Photoluminescence Enhancement and Corresponding Transport Degradation in Individual Suspended Carbon Nanotubes. *Phys. Rev. Applied* **9**, 05402 (2018).
274. Nirmalraj, P. N., Lyons, P. E., De, S., Coleman, J. N. & Boland, J. J. Electrical Connectivity in Single-Walled Carbon Nanotube Networks. *Nano Lett.* **9**, 3890–3895 (2009).
275. Znidarsic, A. *et al.* Spatially Resolved Transport Properties of Pristine and Doped Single-Walled Carbon Nanotube Networks. *J. Phys. Chem. C* **117**, 13324–13330 (2013).
276. Malhofer, A. *et al.* Direct visualization of percolation paths in carbon nanotube/polymer composites. *Org. Electron.* **45**, 151–158 (2017).

277. Balakrishnan, J., Kok Wai Koon, G., Jaiswal, M., Castro Neto, A. H. & Özyilmaz, B. Colossal enhancement of spin–orbit coupling in weakly hydrogenated graphene. *Nat. Phys.* **9**, 284–287 (2013).
278. DiVincenzo, D. P. The Physical Implementation of Quantum Computation. *Fortschr. Phys.* **48**, 771–783 (2000).
279. Awschalom, D. D., Hanson, R., Wrachtrup, J. & Zhou, B. B. Quantum technologies with optically interfaced solid-state spins. *Nat. Photonics* **12**, 516–527 (2018).
280. Schiemann, O., Cekan, P., Margraf, D., Prisner, T. F. & Sigurdsson, S. T. Relative orientation of rigid nitroxides by PELDOR: beyond distance measurements in nucleic acids. *Angew. Chem. Int. Ed.* **48**, 3292–3295 (2009).
281. Nißler, R. *et al.* Chirality enriched carbon nanotubes with tunable wrapping via corona phase exchange purification (CPEP). *Nanoscale* **11**, 11159–11166 (2019).
282. Gao, Z., Varela, J. A., Groc, L., Lounis, B. & Cognet, L. Toward the suppression of cellular toxicity from single-walled carbon nanotubes. *Biomater. Sci.* **4**, 230–244 (2016).
283. Strano, M. S. *et al.* Electronic Structure Control of Single-Walled Carbon Nanotube Functionalization. *Science* **301**, 1519–1522 (2003).

Eidesstattliche Versicherung gemäß §8 der Promotionsordnung der Naturwissenschaftlich-Mathematischen Gesamtfakultät der Universität Heidelberg.

Bei der eingereichten Dissertation zu dem Thema *Luminescent Defects in Polymer-Wrapped Carbon Nanotubes: Synthesis, Properties and Applications* handelt es sich um meine eigenständig erbrachte Leistung.

Ich habe nur die angegebenen Quellen und Hilfsmittel benutzt und mich keiner unzulässigen Hilfe Dritter bedient. Insbesondere habe ich wörtlich oder sinngemäß aus anderen Werken übernommene Inhalte als solche kenntlich gemacht.

Die Arbeit oder Teile davon habe ich bislang nicht an einer Hochschule des In- oder Auslands als Bestandteil einer Prüfungs- oder Qualifikationsleistung vorgelegt.

Die Richtigkeit der vorstehenden Erklärungen bestätige ich.

Die Bedeutung der eidesstattlichen Versicherung und der strafrechtlichen Folgen einer unrichtigen oder unvollständigen eidesstattlichen Versicherung sind mir bekannt.

Ich versichere an Eides statt, dass ich nach bestem Wissen die reine Wahrheit erkläre und nichts verschwiegen habe.

Heidelberg, 29. März 2021

Felix Julian Berger